NACA TN 3227

NATIONAL ADVISORY COMMITTEE FOR AERONAUTICS

TECHNICAL NOTE 3227

APPLICATION OF TWO-DIMENSIONAL VORTEX THEORY TO THE PREDICTION OF FLOW FIELDS BEHIND WINGS OF WING-BODY COMBINATIONS AT SUBSONIC AND SUPERSONIC SPEEDS

By Arthur Wm. Rogers

Ames Aeronautical Laboratory
Moffett Field, Calif.

NACA

Washington
September 1954

TABLE OF CONTENTS

TABLE OF CONTENTS - Concluded

NATIONAL ADVISORY COMMITTEE FOR AERONAUTICS

TECHNICAL NOTE 3227

APPLICATION OF TWO-DIMENSIONAL VORTEX THEORY TO THE PREDICTION OF FLOW FIELDS BEHIND WINGS OF WING-BODY COMBINATIONS AT SUBSONIC AND SUPERSONIC SPEEDS

By Arthur Wm. Rogers

SUMMARY

A theoretical investigation has been made of a general method for predicting the flow field behind the wings of plane and cruciform wing and body combinations at transonic or supersonic speeds and slender configurations at subsonic speeds. The wing trailing-vortex wake is represented initially by line vortices distributed to approximate the spanwise distribution of circulation along the trailing edge of the exposed wing panels. The afterbody is represented by corresponding image vortices within the body. Two-dimensional line-vortex theory is then used to compute the induced velocities at each vortex and the resulting displacement of each vortex is determined by means of a numerical stepwise integration procedure. The method was applied to the calculation of the position of the vortex wake and the estimation of downwash at chosen tail locations behind triangular-wing and cylindrical-body combinations at supersonic speeds. The effects of such geometric parameters as aspect ratio, angle of attack and incidence, ratio of body radius to wing semispan, and angle of bank on the vortex wake behind wings of wing-body combinations were studied. The relative importance of wing vortices, the corresponding image vortices within the body, and body crossflow in determining the total downwash was assessed at a possible tail location.

It was found that the line-vortex method of this report permitted the calculation of vortex paths behind wings of wing-body combinations with reasonable facility and accuracy. A calculated sample wake shape agreed qualitatively with one observed experimentally, and sample results of the line-vortex method compared well with an available exact crossflow-plane solution. An empirical formula was derived to estimate the number of vortices required per wing panel for a satisfactory computation of downwash at tail locations. It was found that the shape of the vortex wake and the ultimate number of rolled-up vortices behind a wing depend on the circulation distribution along the wing trailing edge. For the low-aspect-ratio plane wing and body combinations considered, it appeared that downwash at horizontal tail locations is largely determined except near the tail-body juncture by the wing vortices alone for small ratios of body radius to wing semispan, and by the body upwash alone for large values of that ratio.

INTRODUCTION

Satisfactory aerodynamic design of high-speed aircraft requires knowledge of the interference flow field resulting from wing-body-tail interaction. The behavior of the wing vortex wake in the presence of the body directly affects the air stream flowing past the tail surfaces. In particular, for certain relative sizes and positions of wing, body, and tail, the wing-body vortex wake produces large stream angles at the tail surfaces and nonlinear variation with angle of attack of the pitching moment contributed by the tail. Therefore, it is desirable to be able to predict flow fields at the tail location for a given configuration in order to evaluate stability and control requirements.

Furthermore, vapor-screen studies in supersonic wind tunnels have shown that the configuration of the vortex wake from the wings of some wing-body combinations differs markedly from the usual conception of a sheet whose side edges curl over to form a single pair of vortices. For example, figure 1(a) shows the S-shaped cross section of a vortex sheet from each panel of a high-aspect-ratio supersonic wing and body combination at angle of attack.[1] Here the ultimate vortex pattern far downstream of the wing consists of two vortices from each wing panel, both rotating in the same direction. Such a vortex wake results in a flow field different from the more well-known pattern, and the load on a tail situated in that flow field differs from the tail load associated with a single-vortex wake. It is important, therefore, to determine the conditions under which this unusual wake pattern occurs.

Considerable investigation (refs. 2-12) has been devoted to the prediction of flow fields behind wings, both plane and cruciform. Reference 2 uses linearized conical-flow theory to calculate sidewash and downwash for a flat vortex sheet at the wing trailing edge and in the Trefftz plane, references 3 and 4 use supersonic potential doublet distributions to determine downwash in the plane of a flat wake and in the vertical plane of symmetry for any distance downstream of a wing. Reference 5 employs pressure doublets to obtain general expressions for the induced velocities in space behind a wing, and references 6 through 8 utilize line-vortex theory to predict sidewash and downwash in the flat-vortex wake and in space. The flow in the Trefftz plane behind supersonic wings is treated in reference 9 by means of linearized conical-flow theory. The downwash based on a flat deflected vortex sheet and the downwash based on two deflected vortex lines are calculated in reference 10. The rolling up of the trailing-vortex sheet behind wings is analyzed in reference 11, and reference 12 considers the motion of single vortices from each panel of a cruciform wing. The literature on the vortex wake behind wings of wing-body combinations, however, is still relatively meager (refs. 13 and 14). For wing-body combinations, reference 13 accounts for the effect of the fuselage on the flow field by

---

[1] A description of the vapor-screen technique is given in reference 1.

considering the motion of two fully rolled-up vortices in the presence of a circular cylinder. Reference 14 treats a specific configuration by slender-body theory with the two assumptions of either a flat vortex sheet or two fully rolled-up vortices.

The general problem to be considered here is the determination of the interference flow field behind wings of wing-body combinations (e.g., fig. 2) at subsonic or supersonic speeds. The dual purposes of this report are to present in detail and evaluate the method outlined in reference 13, and to apply it to the calculation of vortex paths and to the effects of wing aspect ratio, span loading, angle of attack, ratio of body diameter to wing span, angle of bank, and wing incidence on vortex paths and downwash at a possible tail location.

Part I of this report presents the results of the application of the method. All calculations of span loading were made for triangular-wing and cylindrical-body combinations at a Mach number of 2.0. Wing aspect ratios of 2/3, 2, and 4 are considered, combined with bodies whose radii are 0.2, 0.4, 0.6, and 0.72 times the wing semispan. The tail location selected for downwash computations in this part represents a missile-type configuration, for which the horizontal tail is assumed to be located in the body diametral plane 10 body radii downstream of the wing trailing edge.

Part II of this report contains a detailed description of the line-vortex method. An examination is made of the effect on downwash at chosen tail locations of the number of vortices used to represent the trailing vorticity. The nature of the stepwise integration method used is discussed, and solutions obtained by the stepwise integration method are compared with known exact solutions. Downwash is also computed at the tail of a high-tail airplane-type configuration, characterized by a horizontal tail 3 body radii downstream of the wing trailing edge and 2 body radii above the body axis.

SYMBOLS

A	aspect ratio
c	local wing chord
c_r	wing root chord in plane of symmetry
$\overline{ds}$	directed line segment of a contour
E	elliptic integral of second kind
$\overline{i},\overline{j},\overline{k}$	unit vectors in x,y,z directions

k	aspect-ratio correction factor defined in Appendix B
L	lift
M	Mach number
n	number of vortices in summation
p	static pressure
Δp	pressure differential across wing surface, $p_l - p_u$
q	free-stream dynamic pressure, $\frac{\rho V_o^2}{2}$
$\overline{q}$	velocity vector, $u\overline{i} + v\overline{j} + w\overline{k}$
r	body radius
s	local horizontal-wing semispan
s_m	maximum horizontal-wing semispan
s'	spanwise position of wing vortex
t	local vertical-wing semispan
t_m	maximum vertical-wing semispan
u,v,w	velocities in x,y,z directions (See fig. 2.)
V_o	free-stream velocity
x_1	chordwise distance from leading edge
x,y,z	Cartesian coordinates of wind axes (See fig. 2.)
$\frac{\Delta p}{q}$	load coefficient
α	angle of attack of body axis, radians
β	$\sqrt{M^2 - 1}$
β'	angle of yaw, $\alpha \sin \varphi$, radians
$\Gamma(y)$	spanwise distribution of circulation (defined by eq. (A1))
Δ	increment

ϵ	downwash angle, $-\frac{w}{V_o}$
θ	$\tan^{-1}\frac{z}{y}$
Λ	wing leading-edge sweep angle, $90^\circ - \omega$, radians
μ,λ,η	dimensionless rectangular coordinates of wind axes, $\frac{x}{r},\frac{y}{r},\frac{z}{r}$, (See fig. 2.)
ρ	air density of free stream
σ,τ	coordinates of source-point in xy plane
φ	angle of bank, radians
Φ_1,Φ_2,φ_1 $\varphi_2, \ldots$	velocity potentials
ω	wing semiapex angle, $\tan^{-1}\frac{s_m}{c_r}$, radians

Subscripts

B	body
i,j	indices of summation
l	lower
m	maximum
u	upper
W	wing
LT	linear theory
SBT	slender-body theory

I.- APPLICATION OF METHOD TO THE PREDICTION OF VORTEX PATHS AND DOWNWASH BEHIND TRIANGULAR-WING AND CYLINDRICAL-BODY COMBINATIONS AT SUPERSONIC SPEED

General Description of Method

The method used herein follows that of reference 13. The circulation distribution along the wing trailing edge of a given wing-body configuration is required as the initial condition. In this report, the circulation distribution is determined by modified slender-body theory. The circulation distribution is then replaced by a finite number of vortices which trail downstream and represent the wake vorticity. The effect of the afterbody is accounted for by vortices placed within the body at the image position of each of the wake vortices. It is assumed, in general, that the flow changes in the stream direction are such that in the velocity potential equation

$$(1 - M^2)\, \varphi_{xx} + \varphi_{yy} + \varphi_{xx} = 0$$

the first term is negligibly small, that is,

$$(1 - M^2)\, \varphi_{xx} = 0$$

so that

$$\varphi_{yy} + \varphi_{zz} = 0$$

Thus the solution is independent of Mach number. Such an assumption of two-dimensionality is valid for slender, pointed wings and bodies at subsonic speed, and at supersonic speed when the entire plan form lies within the body nose Mach cone, or near $M = 1$ for more general configurations.[2]

Consistent with this slender-body theory assumption, the bound vortices within the wing are neglected in computing vortex paths and downwash. The trailing vortices are extended to infinity upstream and downstream, and the induced velocities in crossflow planes are calculated by two-dimensional line-vortex theory and body potential crossflow. In the crossflow plane, therefore, the analysis considers the following picture:

---

[2] See reference 15 for a discussion of these limitations.

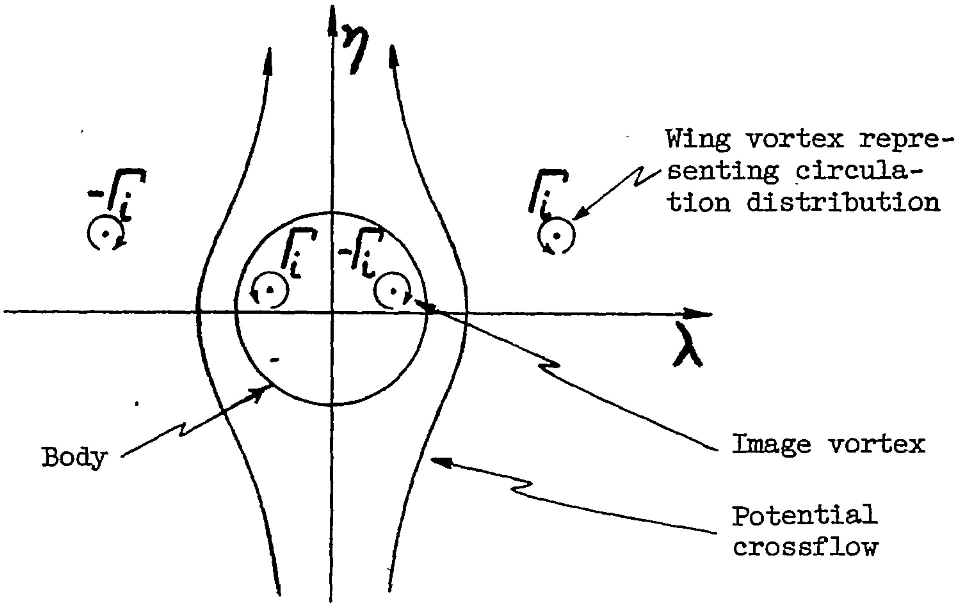

Sketch (a)

The motion of each of the vortices in the crossflow plane is computed, and the results applied to the wing-body problem by relating time in the crossflow plane motion to distance downstream of the wing trailing edge.

The wing and image trailing vortex system used in the stepwise calculations constitutes the only vortex pattern considered here. It is known that at high angles of attack and for large ratios of body diameter to wing span, viscous crossflow produces vortices above the body (e.g., fig. 1 and ref. 1) which significantly affect the flow field. A thorough understanding of the mechanism of formation, strength, and stability of crossflow vortices is as yet lacking. Consequently, no attempt has been made to account for them.

On the basis of a large number of computations made during this investigation, the following analysis was made of the effect of geometric parameters on the vortex wake and the induced flow field behind wings of wing-body combinations. Although only triangular wing and body combinations were studied, the general conclusions should be applicable to any wing plan form for which the circulation distribution is similar to the types contained herein.

Effect of Reduced Aspect Ratio, βA, and Span Loading on the Rolling Up of the Vortex Wake

Figure 3 shows the calculated detailed rolling up of 10 vortices representing a typical wake behind a low-aspect-ratio configuration. Vortex coordinates for this figure are listed in table I. It can be seen that at 10 body radii downstream of the wing trailing edge, 7 of the 10 vortices have already spiraled into a single group which trails downstream in approximately the free-stream direction. The circulation distribution along the trailing edge of the subsonic-leading-edge wing of this configuration is of almost elliptic shape. The vortex sheet behind a wing of a high-aspect-ratio combination, represented in figure 4, distorts much slower toward its final configuration and shows a different pattern. Vortex coordinates for this figure are listed in table II. The different shape of the vortex sheet is due to the change in span loading with reduced aspect ratio βA.

The difference in span loading for the high- and low-aspect-ratio configuration is a consequence of the supersonic or subsonic leading edge, respectively. As a consequence of its supersonic leading edge, the wing trailing edge of the high-aspect-ratio combination of figure 4 has a theoretical circulation distribution which is linear from about the mid-semispan to the tip. This linear distribution is represented by the eight equal, uniformly spaced vortices shown, the remaining two vortices arising from the slender-body type of loading (eq. (3) of part II) inboard of the intersection of leading-edge Mach line and the wing trailing edge. Now, it is characteristic of a uniform distribution of isolated vortices along a line, such as those shown in figure 5, that the rolling up proceeds in the form of a symmetrical, S-shaped curve rotating about the centroid. The final configuration of the vortices in figure 5 will consist of two equal vortex cores, each containing four vortices, rotating symmetrically about the fixed centroid. In figure 4, therefore, the S-shaped rolling up occurs for the uniform portion of the sheet, although the symmetry about and fixity of the centroid in space does not occur because the flow field is due not only to the 8 vortices but also to the other 12 wing vortices, 20 image vortices, and the body crossflow. The inboard portion of the vortex sheet displaces downward and outward in the conventional manner of figure 3. In summary, then, the effect of aspect ratio and the consequent change in circulation distribution is to change the shape of the rolling-up vortex sheet as in sketch (b). The final vortex pattern for the high-aspect-ratio case depends on the extent of the span over which the circulation distribution along the wing trailing edge is linear. A comparison of the calculated S-shaped sheet and an experimentally observed vortex sheet is shown in figures 1(a) and 1(b).

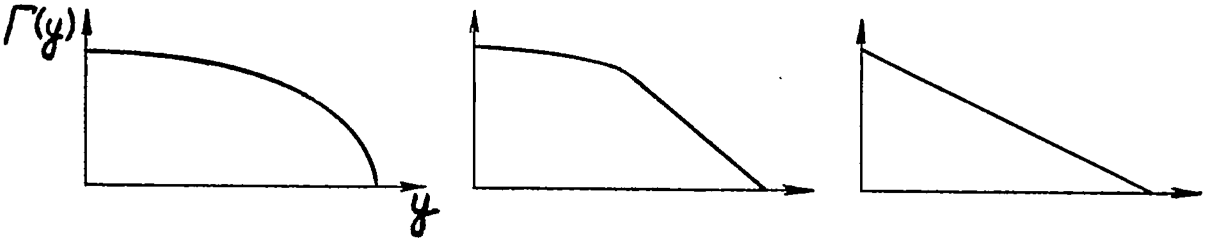

Low βA High βA Very high βA

Trailing-edge circulation distribution

Shape of rolling-up vortex sheet

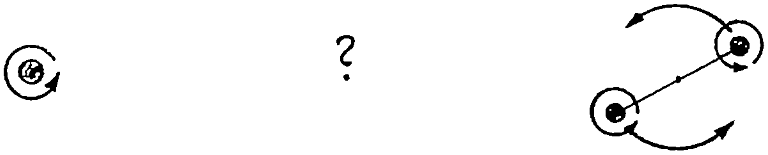

Final vortex pattern

Sketch (b)

Effects of Geometric Parameters on Vortex Paths and Downwash at a Tail Location

In the following sections, calculated vortex paths and downwash are presented for a wing-body-tail combination at a Mach number of 2.0. The tail location at which downwash is determined is 10 body radii downstream of the wing trailing edge, a possible missile-type configuration. The vorticity shed from each wing panel is represented by a single vortex. For the comparison of the relative importance on downwash at the tail of the wing vortex, image vortex, and body crossflow, a single vortex for each wing panel suffices, in general, although the computation of the actual magnitude of downwash requires several vortices. In part II of this report an investigation is made of the effect of the number of vortices used to represent the trailing vorticity on the computed downwash at chosen tail locations.

Effect of aspect ratio.- Figures 6(a), (b), and (c) present the effect of aspect ratio on downwash, calculated at a missile-type tail location, for a small body and wing combination ($r/s_m = 0.2$) at an angle of attack of 5°. For the low-aspect-ratio combination, the approximation that the total downwash is caused by wing vortices alone is good except in close proximity to the tail-body juncture. For increasing aspect ratios the approximation is good only at greater spanwise distances from the body. The reason for this result is simply that the downwash from the wing vortices decreases with increasing aspect ratio for the condition of a given ratio of body radius to wing semispan. The wing lift decreases with increasing aspect ratio because of span load changes, and the effect of the body upwash therefore becomes more pronounced. Slender-body theory predicts that the wake downwash angle exactly cancels the flow angle of attack inboard of the tip. It is interesting to note that inboard of the vortex location for the aspect ratio 2/3 wing ($\lambda \approx 4$) the average downwash angle is roughly the negative of the angle of attack of the wing-body configuration.

Effect of angle of attack.- Vortex paths behind wings of two triangular-wing and body combinations at various angles of attack are presented in figure 7. It is seen that increased angle of attack results in a more pronounced inward and downward motion of the wing vortex with increasing distance μ downstream, although for low-aspect-ratio combinations the initial vertical motion is upward due to body upwash. Farther downstream the distance between the body and the vortex wake increases, with a corresponding decrease in the effect of body upwash. The vortices from the wing panels of the low-aspect-ratio configuration then move downward more rapidly because of their nearness to each other.

Examination of the equations of motion of the vortex wake, presented in part II of this report, shows that for a given wing-body combination a single set of computations can be made for all angles of attack α. The results of figures 7(a) and (b) are replotted against $\mu\alpha$ in figure 7(c), which then applies to all angles of attack, at the same Mach number.

The effect of angle of attack on downwash is illustrated by figures 8(a), (b), and (c) for an aspect ratio 2/3 wing and large-body combination, and by figures 8(d), (e), and (f) for an aspect ratio 4 wing and small-body combination. For the low-aspect-ratio configuration, it appears that the largest portion of the total downwash is contributed by the body upwash because of the large body. The difference in the shape of the total downwash curves of figures 8(a), (b), and (c) is due to the fact that the vortex wake passes farther above the horizontal tail as the angle of attack increases. For the high-aspect-ratio configuration the total downwash is not primarily caused by any single component because of the small body size. Wing and image vortices together with body upwash must be considered in calculating total downwash at any angle of attack for such configurations.

Effect of ratio of body radius to wing semispan.- Another parameter governing the behavior of the vortex wake is the ratio of the body radius to the wing semispan, r/s_m. Figure 9 presents the results for an aspect ratio 2/3 wing of fixed span, alone and in combination with bodies of different radii. The variation of the vortex strength with body size, given by equation (3) with $y = r$, is plotted in figure 10. The vortex strength goes to zero for $r/s_m = 1$ since the entire wing then is enclosed by the body. It is seen in figure 9 that the initial slope of the vertical displacement of the vortex path near the wing trailing edge increases in magnitude as r/s_m increases. This is the result of increasing upwash in the body crossflow field coupled with correspondingly decreasing wing vortex strength (see fig. 10). The final uniform downward motion of the vortex pair begins when the body is far removed from the vortices, and the path lies above that for the wing alone case in which the vortex pair moves linearly downward from the trailing edge. The lateral motion of the trailing vortex is shown in the lower part of figure 9. Together with the decreased strength of the wing vortex for large values of r/s_m, there is an initial outboard shift of the vortex at the trailing edge. For the isolated elliptically loaded wing, y/s_m equals $\pi/4$ and it approaches 1 (the initial vortex location moves toward the wing tip) as r/s_m increases from 0 to 1. The lateral vortex motion downstream is affected by the sidewash component of the body crossflow field. The larger the body for a given wing, the more rapid is the inboard motion of the vortex.

Figures 6(a), 11(a), 8(a), and 11(b) show the effect of r/s_m on downwash for ratios of body radius to wing semispan of 0.2, 0.4, 0.6, and 0.72, respectively. The results shown in the figures can be anticipated qualitatively. For an r/s_m of 0.2, figure 6(a) shows that the downwash contributed by the image vortices almost entirely cancels the body upwash, except in close proximity to the body-tail juncture. Thus, for small ratios of body radius to wing semispan, downwash at the tail location is mostly given by the downwash caused by the wing vortices alone except near the juncture. Figure 11(a), for an r/s_m of 0.4, exhibits a decrease in downwash from the wing vortices, and the total downwash is not as well given by the wing vortices as in figure 6(a) especially near the body-tail juncture. Figure 8(a), for an r/s_m of 0.6, shows that except near the body-tail juncture the downwash in this case is largely that given by the body upwash. Finally, figure 11(b) for an r/s_m of 0.72, showing the same trend as figure 11(a) and figure 8(a), indicates that for very large ratios of body radius to wing semispan, such as for canard configurations, the downwash at the tail is almost entirely determined by the body upwash.

Comparison of Rolling Up of Vortex Sheet Behind Wing Alone and Wing-Body Combination

Plane wing and body.- It is interesting to compare the rolling-up process of the vortex sheet behind a wing alone with that behind a wing-body combination under the conditions of sketch (c).

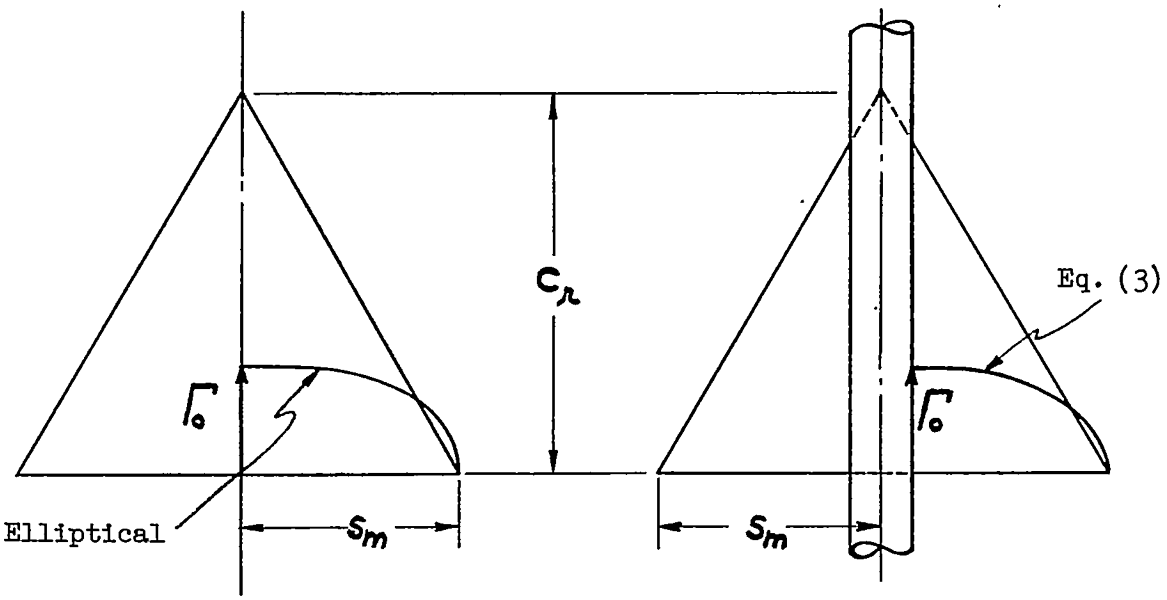

Sketch (c)

Both wings have the same aspect ratio, root chord, and Γ_o. However, this maximum Γ occurs at the center line for the wing (with elliptical distribution) and at the wing-body juncture for the wing-body combination (with near-elliptical circulation distribution). Figure 5 of reference 11 presents a picture of the rolling up of a vortex sheet behind an elliptically loaded wing as calculated by Westwater (ref. 16) in terms of the ratio of downstream distance d to rolling-up distance e. This ratio is related to μ in figure 3 as follows (using eq. (5) of ref. 11):

$$\frac{d}{e} \times \frac{e}{c} = \frac{d}{c} = \left(\frac{d}{e}\right)(K)\left(\frac{A}{C_L}\right)\left(\frac{b}{c}\right)$$

or

$$\frac{d}{b} = \left(\frac{d}{e}\right)(K)\left(\frac{A}{C_L}\right)$$

where

b wing span

C_L total lift coefficient

K constant based on the shape of the trailing-edge circulation distribution

The value of K is 0.28 for elliptic loading. Now equation (10) of reference 11 is:

$$\Gamma_o = 4sV_o \frac{C_L}{\pi A}$$

where Γ_o corresponds to elliptic loading for the wing alone. When the last two equations are combined,

$$\frac{d}{b} = \left(\frac{d}{e}\right)(0.28) \frac{4s}{\pi(\Gamma_o/V_o)}$$

or

$$\frac{d}{s} = \frac{2.24}{\pi}\left(\frac{d}{e}\right)\frac{s}{\Gamma_o/V_o}$$

In the present notation,

$$\frac{d}{s} = \frac{x}{s_m}$$

The lift coefficient of a triangular-wing and infinite cylindrical-body combination in terms of the wing alone lift coefficient is given by equation (38) of reference 15 as:

$$C_{L_{W+B}} = C_{L_W}\left(1 - \frac{r^2}{s_m^2}\right)^2$$

It is clear that while the same Γ_o is chosen in this comparison, the total lift of the combination is less than that of the wing alone because of the loss of exposed wing area. For the calculations of figure 3, Γ_o/V_o equals 0.575 and s_m equals 3.75. These values being assumed in the equation for d/s,

$$\frac{x}{s_m} = \left(\frac{2.24}{\pi}\right)\left(\frac{d}{e}\right)\left(\frac{3.75}{0.575}\right) = 4.65\left(\frac{d}{e}\right)$$

For figure 3:

$$\frac{x}{s_m} = \frac{x}{r} \times \frac{r}{s_m} = 0.2\mu$$

Therefore the streamwise stations in figure 3 correspond to 0.2, 0.4, 0.6, . . . 2 wing semispans downstream. The values of d/e in figure 5 of reference 11 correspond to values of x/s_m of 0, 0.233, 0.977, 1.953, 4.370, and 8.040. Cross sections through the vortex sheet at these six stations have been drawn in figure 12 as well as the nearest corresponding sheet configuration from figure 3. From figure 12 it can be seen that the rolling-up process of the vortex sheet behind a triangular-wing and small-body combination closely resembles that for a wing alone under the conditions of the preceding sketch.

Banked wing and body.- The qualitative difference between the rolling-up motion of a vortex wake behind an isolated wing and wing-body combination both banked at a given small angle and at angle of attack can be reasoned simply with the aid of sketch (d), illustrating conditions immediately behind the trailing edge.

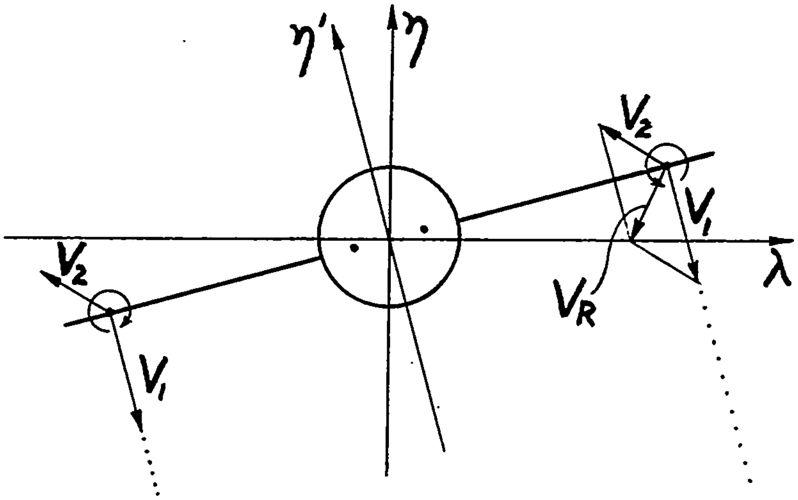

Sketch (d)

For the isolated wing, each panel vortex induces a velocity V_1 on the opposite vortex and both move in the dotted direction with uniform velocity. The motion in this case is symmetric with respect to the $\eta'\mu$ plane. Now the addition of a body, with potential crossflow symmetrical respect to the $\eta\mu$ plane, adds the same induced velocity V_2 at each vortex. The wing vortices in this case then move initially in the direction of the resultant velocity V_R. Henceforth, the velocity due to the body crossflow is different at each vortex. Thus it can be seen that the wake motion is different from that behind an isolated wing, that is, completely nonsymmetrical. Similar reasoning for wing vortices of unequal strength leads to the same conclusion.

For a cruciform wing and body combination at 45° angle of bank and at angle of attack, the superposed velocity fields (from the wing and body) are both symmetrical with respect to the $\eta\mu$ plane. Therefore the computed vortex wake motion should agree qualitatively with results for isolated cruciform wings.

II.- PRESENTATION AND EVALUATION OF METHOD

The remainder of this report will examine in detail the line-vortex method outlined in reference 13. The manner by which the initially required circulation distribution was obtained is first discussed. The method of replacing the wake circulation distribution and the afterbody by discrete vortices then follows. The determination of the flow field in transverse planes and the stepwise integration technique are next explained. After a few sample calculations, an evaluation is made of the errors inherent in the stepwise integration and of the effect of the number of vortices used on the computed downwash distribution at chosen tail locations.

Circulation Distribution at Wing Trailing Edge

Before the stepwise calculation of vortex paths behind the wings of wing-body combinations can be started, it is necessary to know the circulation distribution along the wing trailing edge. In general, the circulation distribution $\Gamma(y)$ and the wing span loading are not equivalent. The conditions for equivalence are derived in Appendix A. The method of this report has been applied to triangular-wing configurations which have readily obtainable circulation distributions. However, the stepwise calculation method is applicable to configurations with any wing plan form.

For a plane-wing and cylindrical-body combination, the span loading is equivalent to the circulation distribution and can be obtained by chordwise integration of the complete pressure coefficient $(\Delta p/q)_W$. Equations for $(\Delta p/q)_W$ are given in the slender-body analysis of reference 15. For such configurations, the circulation about the wing at any spanwise station y is given by linear theory as:

$$\Gamma(y) = \frac{V_o}{2}\int_0^c \left(\frac{\Delta p}{q}\right)_W dx_1 \tag{1}$$

The notation for this and the following equations is defined in figure 13, which shows the more general case of a noncylindrical body.

Equation (11) of reference 15 furnishes the wing loading coefficient for a plane-wing and cylindrical-body combination as:

$$\left(\frac{\Delta p}{q}\right)_W = 4\alpha \frac{\frac{ds}{dx}\left(1 - \frac{r^4}{s^4}\right)}{\sqrt{1 + \frac{r^4}{s^4} - \frac{y^2}{s^2}\left(1 + \frac{r^4}{y^4}\right)}} \tag{2}$$

Substitution of equation (2) in equation (1) and integration yields:

$$\Gamma(y) = \frac{2V_o\alpha}{s_m y}\sqrt{(s_m{}^2 - y^2)(s_m{}^2y^2 - r^4)} \tag{3}$$

When the body is not cylindrical, equation (2) is modified to:

$$\left(\frac{\Delta p}{q}\right)_W = 4\alpha\left[\frac{\dfrac{ds}{dx}\left(1 - \dfrac{r^4}{s^4}\right) + 2\,\dfrac{r}{s}\,\dfrac{dr}{dx}\left(\dfrac{r^2}{s^2} - \dfrac{r^2}{y^2}\right)}{\sqrt{1 + \dfrac{r^4}{s^4} - \dfrac{y^2}{s^2}\left(1 + \dfrac{r^4}{y^4}\right)}} - \frac{\dfrac{dr}{dx}\left(1 - \dfrac{r^4}{y^4}\right)}{\sqrt{\left(1 - \dfrac{y^2}{s^2}\right)\left(\dfrac{s^2}{r^2} - \dfrac{r^2}{y^2}\right)}}\right] \tag{4}$$

The last term of equation (4) is due to the spanwise velocity and does not contribute to the circulation distribution. Hence one obtains the required circulation distribution by insertion of only the first term of equation (4) in equation (1) and integration. The result is identically equation (3). This shows that the circulation distribution $\Gamma(y)$ along the trailing edge of a plane wing on a noncylindrical body is dependent only on the cross section of the configuration at the trailing edge, as could be anticipated. The circulation is, in fact, the jump in the crossflow potential at the trailing edge and hence must agree with the slender-body result, equation (3).

For cruciform wings on a cylindrical body at angle of attack and sideslip, the complete velocity potential (eq. (47) of ref. 15) is:

$$\begin{aligned}
\Phi_1 = {} & \pm\frac{V_o\alpha'}{\sqrt{2}}\left\{\left[-\left(1 + \frac{r^4}{r_1{}^4}\right)r_1{}^2\cos 2\theta + s^2\left(1 + \frac{r^4}{s^4}\right)\right] + \left[r_1{}^4\left(1 - \frac{r^4}{r_1{}^4}\right)^2 + \right.\right. \\
& \left.\left. 4r^4\cos^2 2\theta + s^4\left(1 + \frac{r^4}{s^4}\right)^2 - 2s^2\left(1 + \frac{r^4}{r_1{}^4}\right)\left(1 + \frac{r^4}{s^4}\right)r_1{}^2\cos 2\theta\right]^{\frac{1}{2}}\right\}^{\frac{1}{2}} - \\
& V_o\alpha' z \pm \frac{V_o\beta'}{\sqrt{2}}\left\{\left[\left(1 + \frac{r^4}{r_1{}^4}\right)r_1{}^2\cos 2\theta + t^2\left(1 + \frac{r^4}{t^4}\right)\right] + \right. \\
& \left[r_1{}^4\left(1 - \frac{r^4}{r_1{}^4}\right)^2 + 4r^4\cos^2 2\theta + t^4\left(1 + \frac{r^4}{t^4}\right)^2 + \right. \\
& \left.\left. 2t^2\left(1 + \frac{r^4}{t^4}\right)\left(1 + \frac{r^4}{r_1{}^4}\right)r_1{}^2\cos 2\theta\right]^{\frac{1}{2}}\right\}^{\frac{1}{2}} + V_o\beta' y
\end{aligned} \tag{5}$$

where

$$r_1^2 = y^2 + z^2, \qquad \theta = \tan^{-1}\frac{z}{y}$$

and

$$+ \text{ means } 0 < \theta < \pi$$

$$- \text{ means } \pi < \theta < 2\pi$$

The transformation to a configuration pitched α radians and banked φ radians is for small angles α:

$$\alpha' = \alpha \cos \varphi, \qquad \beta' = \alpha \sin \varphi \tag{6}$$

Now for banked cruciform configurations, the span load distribution is not equivalent to the circulation distribution. Hence, instead of equation (1) one must use the general relation between Γ and the jump in the velocity potential at the wing trailing edge:

$$\Gamma = \Delta\varphi_{TE} \tag{7}$$

For horizontal and vertical surfaces respectively, one obtains by substitution of equation (5) in equation (7):

$$\Gamma(y) = \frac{2V_o\alpha'}{s_m y}\sqrt{(s_m^2 - y^2)(s_m^2 y^2 - r^4)} \tag{8}$$

$$\Gamma(z) = \frac{2V_o\beta'}{t_m z}\sqrt{(t_m^2 - z^2)(t_m^2 z^2 - r^4)} \tag{9}$$

It is thus seen, by comparing equations (8) and (9) with (3), that the circulation distribution for a cruciform wing and body combination is derivable by assuming that each wing acts independently of the other as part of a plane wing and body combination at an angle of attack given by equation (6). This can be seen also by the linear superposition of potentials in equation (5).

The foregoing equations are based on the slender-body theory of reference 15, which is postulated for slender wing and body configurations at subsonic, transonic, and supersonic speeds. In order for the equations to apply at supersonic speeds, the entire configuration must lie well within the body nose Mach cone. Experimental data on models conforming to these restrictions agree well with the theory. In order to apply the results of slender-body theory to nonslender wing and body combinations, an aspect-ratio correction factor is employed. This factor, which for triangular-wing configurations is the ratio of the lift of a triangular wing calculated by linear theory to the lift calculated by slender-body theory, is discussed fully in Appendix B. The results may be summarized as follows: For subsonic-leading-edge wings ($\beta \tan \omega < 1$), equations (3), (8), and (9) should be multiplied by the factor

$$k = \frac{1}{E}\left(\sqrt{1 - \beta^2 \tan^2 \omega}\right)$$

For supersonic-leading-edge wings, ($\beta \tan \omega > 1$), these equations should be multiplied by equations (B7) or (B18) for the ranges of y indicated:

$$k = \frac{1}{\sqrt{\beta^2 \tan^2 \omega - 1}} \sqrt{\frac{s_m - y}{s_m + y}} \tag{B7}$$

for

$$r + \frac{s_m - r}{\beta \tan \omega} \leq y \leq s_m$$

$$k = \frac{1}{\sqrt{(s_m^2 - y^2)(\beta^2 \tan^2 \omega - 1)}} \left\{ s_m + \frac{1}{\pi} \left[(s_m - y) \sin^{-1} \frac{y\beta^2 \tan^2 \omega - s_m}{\beta \tan \omega (s_m - y)} - \right. \right.$$

$$\left. \left. (s_m + y) \sin^{-1} \frac{y\beta^2 \tan^2 \omega + s_m}{\beta \tan \omega (s_m + y)} \right] \right\} \tag{B18}$$

for

$$r \leq y \leq r + \frac{s_m - r}{\beta \tan \omega}$$

Replacement of Wake Circulation Distribution and Body by Discrete Vortices

After the circulation distribution $\Gamma(y)$ along the wing trailing edge has been determined, the next step is the replacement of the consequent wake circulation function by a finite number of vortices. A plot of the circulation function, equation (3), for example, looks like that portion of the solid curve above the wing in sketch (e):

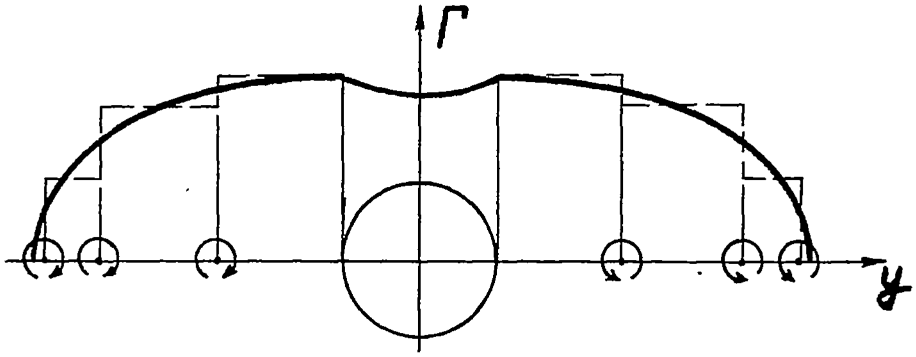

Sketch (e)

The loading over the body, which can be calculated from the corresponding body pressure coefficient (eq. (12) of ref. 15), is not explicitly required here. It will be seen that this loading is automatically accounted for by the vortex model set up for the wing loading. The curve $\Gamma(y)$ over the wing can be replaced by a suitable number of step functions (dashed lines in sketch), each of which corresponds to a vortex of strength equal to the step height and located at the step abscissa as shown. Although an infinite number of step functions would be required to duplicate the given curve, in practice the number selected are the fewest which render possible a reasonably accurate prediction of the trailing-vortex sheet behavior. Single-, three-, and ten-step function distributions have been used herein. Quantitative results will be presented later concerning the number of vortices used to replace the circulation distribution. For a single-step (one vortex) approximation, integrating equation (3) for the area under the $\Gamma(y)$ curve and equating the result to a single rectangular area lead to the simple result shown in figure 14, namely, that the spanwise distance from the body of a single vortex representing the circulation distribution on one panel of a plane, subsonic-leading-edge wing and body combination is approximately constant and equal to about 0.76 times the exposed wing semispan for all ratios of body radius to wing semispan. In this approximation by a single vortex the value of Γ_{max} at the wing-body juncture is assigned to the vortex. In all cases the two panels of the wing are treated independently. A circulation distribution which, unlike the preceding sketch, is asymmetrical across the wing trailing edge will, therefore, require an asymmetrical vortex distribution.

The effect of a circular body in the presence of this wing vortex distribution is accounted for by placing an image vortex for each wing vortex within the body at the inverse point, as indicated by sketch (f). The image vortex cancels the velocity normal to the body due to the wing vortex.

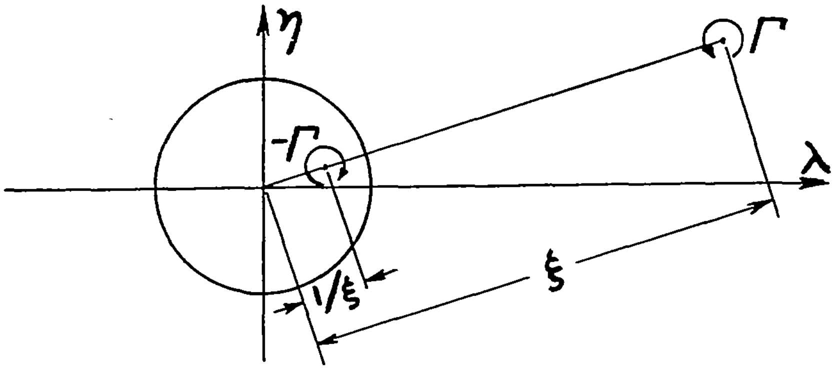

Sketch (f)

The foregoing discussion applies to the trailing-vortex filaments from the wing and the image vortices contained within the body. These filaments can be considered joined by bound vortices within the wing and adjacent body to form horseshoe vortices as shown in sketch (g). The portion of the total lift of the wing-body combination carried by the wing and by the body is represented by the bound filaments of length l_2 within the wing and l_1 within the body, respectively. A plot of $\Gamma(y)$ across the body is, therefore, obviated since the single vortex representing the body loading automatically appears at the inverse (image) point of the wing vortex. This vortex model, due to Lennertz (ref. 17), assumes that the ratio of body to wing lift is proportional to the ratio l_1/l_2 ($l_1 + l_2$ being the "effective semispan"), and is known from experiments to represent the distribution of lift between wing and body with good accuracy, deviating but slightly from slender-body theory.

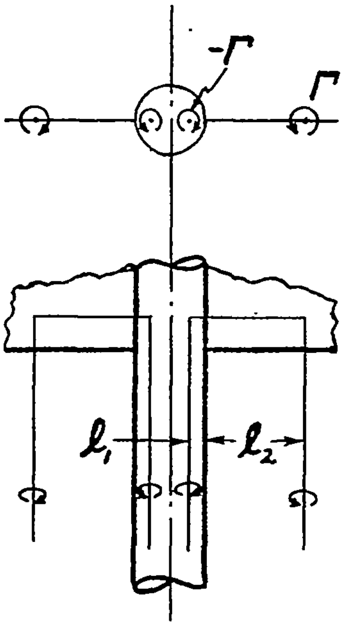

Sketch (g)

Consistent with the assumed two-dimensional nature of the solution, the segments of the vortices bound within the wing and adjacent body are neglected. It is then assumed that the remaining filaments extend upstream to infinity.

Determination of the Flow Field in Transverse Planes

The nonlinear differential equations governing the downstream motion of the vortex wake require a stepwise solution for the vortex positions at successive streamwise stations (or time increments). Consider a vortex pattern at any downstream station such as section A-A in figure 2. (The image vortices inside the body are not shown in the figure.) It is assumed that every vortex influences the flow field according to the Biot-Savart velocity law of planar, incompressible-flow vortex theory, as illustrated in the sketch (h). This assumption will be justified later.

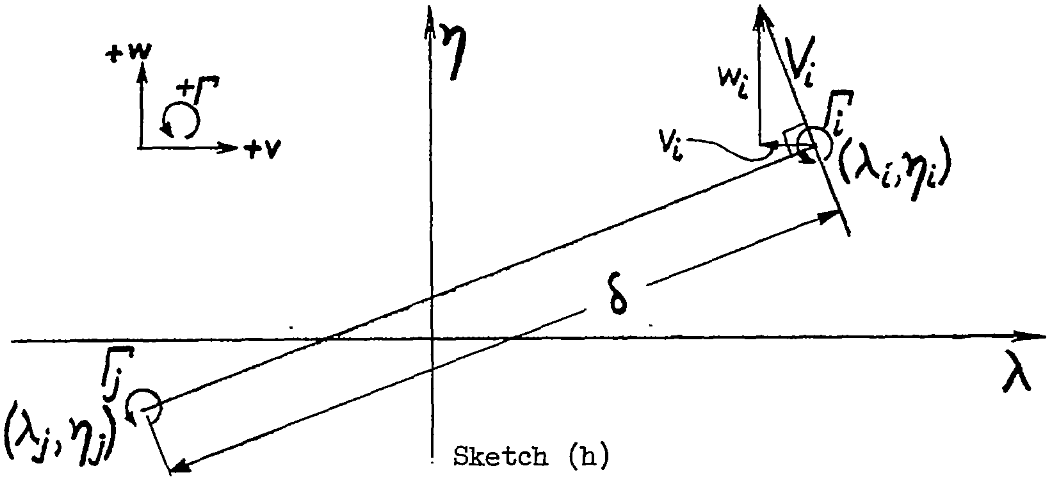

Sketch (h)

The velocity V_i induced at the ith vortex by the jth vortex is:

$$V_i = \frac{\Gamma_j}{2\pi r\delta} \qquad (10)$$

The vertical component, w_i, of V_i is:

$$w_i \equiv r\dot{\eta}_i = \frac{\Gamma_j}{2\pi r} \frac{\lambda_i - \lambda_j}{(\lambda_i - \lambda_j)^2 + (\eta_i - \eta_j)^2} \qquad (11)$$

The horizontal component, v_i, of V_i is:

$$v_i \equiv r\dot{\lambda}_i = \frac{-\Gamma_j}{2\pi r} \frac{\eta_i - \eta_j}{(\lambda_i - \lambda_j)^2 + (\eta_i - \eta_j)^2} \qquad (12)$$

In general, for a flow field containing n vortices, the velocity components induced at the position of the ith wing vortex by the other n-1 vortices are:

$$w_i = \frac{1}{2\pi r} \sum_{\substack{j=1 \\ \neq i}}^{n} \frac{\Gamma_j(\lambda_i - \lambda_j)}{(\lambda_i - \lambda_j)^2 + (\eta_i - \eta_j)^2} \qquad (13)$$

$$v_i = \frac{-1}{2\pi r} \sum_{\substack{j=1 \\ \neq i}}^{n} \frac{\Gamma_j(\eta_i - \eta_j)}{(\lambda_i - \lambda_j)^2 + (\eta_i - \eta_j)^2} \tag{14}$$

Equation (10) is derived from consideration of an infinitely long, incompressible-flow vortex filament, and is, therefore, applicable only to two-dimensional flow. For supersonic speeds, the use of equation (10) is consistent with the slender-body theory underlying this study for these reasons: Reference 7 shows that an infinitely long vortex filament parallel to a supersonic stream obeys the Biot-Savart law of incompressible flow. Omission of the bound vortex and wing chord loading causes the difference between initial and asymptotic downwash at the wing trailing edge seen in figure 15 reproduced from reference 7; the downwash along the wake center line approaches the asymptotic value within a chord length behind the trailing edge for the triangular wings of $\beta A < 4$. Hence the asymptotic downwash given by a two-dimensional trailing-vortex system has been used.

Superimposed on the velocity field due to the wing and image vortex system is the body potential crossflow velocity field. From the potential:

$$\varphi_1 = V_o \, \alpha z' \left(\frac{r^2}{y^2 + z'^2} \right) \tag{15}$$

where z' is measured from the body axis (instead of the wind axis), one readily obtains the velocity components induced by the body:

$$w = \frac{\partial \varphi_1}{\partial z'} = V_o \alpha r^2 \frac{y^2 - z'^2}{(y^2 + z'^2)^2} \tag{16}$$

$$v = \frac{\partial \varphi_1}{\partial y} = \frac{-2V_o \alpha r^2 y z'}{(y^2 + z'^2)^2} \tag{17}$$

or in dimensionless form:

$$\frac{w}{V_o} = \alpha \frac{\lambda^2 - \eta'^2}{(\lambda^2 + \eta'^2)^2} \tag{18}$$

$$\frac{v}{V_o} = \frac{-2\alpha \lambda \eta'}{(\lambda^2 + \eta'^2)^2} \tag{19}$$

where

$$\eta' = \eta + \mu \tan \alpha \cong \eta + \mu\alpha \qquad (20)$$

This transformation from the usual potential equations is necessitated here by the fact that the coordinates are not body centered, and the body is inclined, with respect to the free-stream direction.

These last equations assume that the body angle of attack is small enough so that $\tan \alpha \approx \alpha$, $\cos \alpha \approx 1$ (which is true for α up to approximately 20°), and that the contribution of the crossflow to the local streamwise velocity is negligible. As stated previously, viscous crossflow separation around the body, with its consequent vortex wake, is not considered here.

Stepwise Determination of Vortex Paths

The replacement of the wing trailing-edge circulation distribution by step functions and associated vortices, together with the placement of image vortices within the body, as detailed above, provide the starting point for the stepwise calculations to be described. The spanwise and heightwise coordinates of all vortices at $\mu = 0$ are known. The downstream incremental motion of these vortices will next be determined.

Now at any point in a transverse (yz) plane, the lateral velocity, v, is given by the sum of equations (14) and (19). The vertical velocity, w, is similarly given by the sum of equations (13) and (18). The streamwise velocity, u, perpendicular to the plane, is everywhere V_o. Consider the point where a vortex line passes through the transverse plane. In a time interval Δt the vortex filament moves with the fluid a vertical distance $\Delta z = w\,\Delta t$. Since $\Delta t = \Delta x/V_o$, $\Delta z = (w/V_o)\Delta x$, then nondimensionally:

$$\Delta\eta = \frac{w}{V_o}\Delta\mu \qquad (21)$$

Similarly the dimensionless lateral movement is:

$$\Delta\lambda = \frac{v}{V_o}\Delta\mu \qquad (22)$$

The last two equations then furnish points in transverse planes a distance $\Delta\mu$ apart, the locus of which is the path of a vortex filament moving in the wing-body flow field. With each vortex, a "strength" Γ_j/V_o (rather than Γ_j) will be associated in order that equations (13) and (14) will actually yield the velocity ratios w/V_o and v/V_o.

In the plane $\mu = 0$, which contains the wing trailing edge, as long as the wings have no incidence with respect to the body, all the vortex filaments have coordinates $\eta \equiv 0$. Therefore, the total spanwise velocity induced at the location of any given wing vortex can readily be seen to be zero, from equations (14) and (19). In fact, the initial motion of such a vortex sheet is always one of pure vertical displacement. The total vertical velocity summed from equations (13) and (18) is multiplied by a suitable increment $\Delta\mu$ yielding an incremental distance $\Delta\eta$ moved by the given vortex line, according to equation (21). Values of $\Delta\eta$ are thus calculated for all the wing vortices, the entire group of which is so transported to the plane $\mu = \Delta\mu$. The coordinates of each wing vortex in this new plane are found simply by adding the computed increments to the coordinates at the previous station. Of course, symmetrical properties are used wherever possible to obviate the calculation of the paths of vortices from each half of a wing. Corresponding to the new location of each wing vortex line at the station $\mu = \Delta\mu$, the image vortices within the body are repositioned according to the following formulas:

$$\lambda_{image} = \frac{\lambda}{\lambda^2 + (\eta + \mu \tan \alpha)^2} \tag{23}$$

$$\eta_{image} = -\mu \tan \alpha + \frac{\eta + \mu \tan \alpha}{\lambda^2 + (\eta + \mu \tan \alpha)^2} \tag{24}$$

where (λ,η) are the coordinates of the wing vortex at the new station $\mu = \Delta\mu$. This readjustment of the image vortex positions, required by the downstream displacement of the inclined body away from the free-stream direction, is made because the image vortices are bound within the body; the image vortex displacement, in fact, measures the amount of lift carried by the afterbody (see ref. 13).

With the new positions of wing and image vortices this procedure is repeated. That is, the total lateral and vertical velocity induced at each wing vortex location is calculated and multiplied by an incremental distance $\Delta\mu$. The new wing vortex positions are obtained by adding the computed increments to the original coordinates. The image vortices are then repositioned according to the new wing vortex locations, and the stepwise calculation continued to the desired downstream station.

This stepwise procedure is simply a method for integrating numerically n simultaneous differential equations of motion of $n/2$ wing vortices for the downstream paths. A closed solution for the three-dimensional paths is, in general, extremely complicated, if not impossible. While the equations of the vortex motions in a transverse or crossflow plane can be written, introduction of time dependence (equivalent to the streamwise coordinate) renders a closed solution extremely difficult. Reference 13, using complex variable notation, cites explicitly the entire path of a pair of vortices in the presence of a cylinder in the transverse plane. The equations were derived by Villat in reference 18. Even for this simple case, where $n = 4$, recourse is necessary to numerical solution for the time or streamwise coordinate. This solution will be analyzed in greater detail subsequently, as well as the manner of choosing the proper spacing $\Delta\mu$ of successive stations.

Sample Calculations

Three examples will now be presented to illustrate the calculative procedure and resulting vortex paths. They are:

1. A plane-wing and cylindrical-body combination at angle of attack.

2. A cruciform-wing and cylindrical-body configuration at angle of attack and bank.

3. A plane-wing and cylindrical-body combination with the body at angle of attack and the wing panels at differential incidence.

The procedure has been systematized by prepared computation forms such as table III which is used when the circulation distribution on one wing panel is replaced by a single vortex.

Example 1, plane triangular-wing and cylindrical-body combination at angle of attack.- The data for this example are: wing aspect ratio = 2/3, ratio of body radius to wing semispan = 0.6, angle of attack = 5°, and Mach number = 2.0.

The leading edge of the wing is subsonic ($\beta \tan \omega = 0.2912 < 1$), so the trailing-edge circulation distribution $\Gamma(y)$ is calculated from equation (3) and multiplied by the aspect-ratio correction factor $k = 0.917$ (see Appendix B). A plot of $\Gamma(y)$ vs. y like that of figure 14 is obtained, with a maximum ordinate $\Gamma/V_o = 0.12796$ in this example. First, this distribution is replaced by a single vortex per wing panel, with the location consequently given by figure 14 as $s'/(s_m - r) = 0.763$, or $\lambda_1 = 1.509$ $(r/s_m = 0.6)$. The vertical coordinate of the vortex at the wing trailing edge $(\mu = 0)$ is zero in this case. The dimensionless spanwise coordinate of the image vortex is, therefore, $\lambda_2 = 1/\lambda_1 = 0.663$.

Referring now to table III(a), the above values of Γ_1/V_o, λ_1, η_1 λ_2, and η_2 are filled into the proper boxes of columns ②, ③, and ④. By symmetry, the values of λ_3, λ_4, η_3, and η_4 can be readily filled in, and an increment $\Delta\mu$ is chosen (1 here). Columns ⑤ through ⑨, based on equations (13) and (14), are then computed in order, the last two giving the vertical and horizontal velocity components induced at vortex 1 by the other three vortices (columns ⑧ and ⑨, respectively). Rows ⑩ through ㉓, based on equations (18) through (22), next add the potential crossflow velocity components at vortex 1. Thus, rows ㉒ and ㉓ give the new coordinates of vortex 1 for use in table III(b), while the bottom calculation furnishes the coordinates of the corresponding new image vortex 2 position.

Columns ② through ④ of the table III(b), for station $\mu = 1$, can now be filled in and the procedure repeated, as illustrated. This stepwise computation is continued for as many stations downstream as desired, each part of this example representing positions at increments of one body radius ($\Delta\mu = 1$) downstream of the wing trailing edge. The results are summarized graphically by figure 16.

For the same given data, the calculated circulation distribution for one wing panel is now replaced by three vortices of equal strength $\Gamma/V_o = 0.042653$. Their spanwise locations are determined graphically, equating areas under the curve of $\Gamma(y)$ vs. y, and in this example are: $\lambda_1 = 1.652$, $\lambda_2 = 1.558$, and $\lambda_3 = 1.316$. The three image vortex locations are again calculated as the inverse points, giving: $\lambda_4 = 0.75988$, $\lambda_5 = 0.64185$, and $\lambda_6 = 0.60533$. The results of this case are shown in figure 17.

Example 2, cruciform triangular-wing and cylindrical-body configuration at angle of attack and bank.- The configuration data of the preceding example are again assumed in addition to which another pair of wing panels now exists, forming a cruciform wing-body arrangement banked 45°. The strengths of the assumed four vortices originating from the four wing panels are identical, as required by equations (8) and (9). These equations with equation (6) provide the required circulation distribution $\Gamma(y)$ and $\Gamma(z)$ which is corrected for aspect ratio as explained in Appendix B. Figure 14 again furnishes the initial positions of the four wing vortices, whose corresponding four image vortices are then located at the inverse points. The calculative procedure follows that described above. Because of planar (xz) symmetry, only the paths of a pair of vortices on one side of the body need be computed. The results of this case are presented in figure 18, which shows that there is a tendency toward "leapfrogging," sketch (i)[3] although the process appears to be retarded initially by the body.

---

[3] The phenomenon of "leapfrogging" vortices is discussed in detail for isolated wings in reference 12.

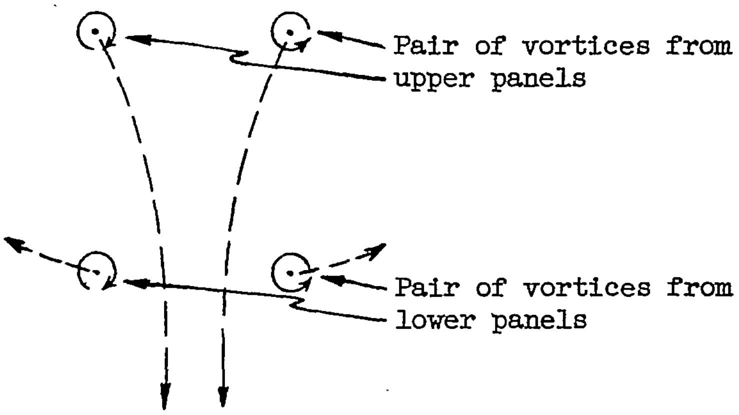

"Leapfrogging" paths in crossflow plane

Sketch (i)

<u>Example 3, plane-wing and cylindrical-body combination with the body at angle of attack and the wing panels at differential incidence</u>.- The given data for this case are the same as for the first example with two exceptions. One wing panel is deflected and the other is at zero incidence with respect to the body axis such that the vortex from each panel has the same strength. Now the vortices from both wing panels are rotating in the same direction. The vortex shed from the deflected panel is assumed to start above the xy plane because of the angular displacement about the hinge line of that panel's trailing edge. It is further assumed that the vortex from each panel is shed at the same spanwise station.

Figure 19 illustrates an effect characteristic of wings differentially inclined. The vortex from the wing panel which has no incidence to the body moves essentially the same way as in the plane wing case. However, the vortex from the wing panel which is at a negative angle of attack travels sharply upward and inboard. This marked motion is due to two effects: First, the vortex starts at the trailing edge with some $\eta > 0$ because of the negative angle of attack of the panel, and second, the body crossflow and image vortex-induced velocities are cumulative in this case instead of being subtractive as in the plane case. At a sufficiently high angle of attack, it may be possible for the rising vortex to jump over the body to the same side as the other vortex. Such an occurrence would cause a sharp increase in rolling moment from the tail surfaces.

For the case of a pair of wing panels inclined together, the trailing vortex paths can be estimated qualitatively by consideration of the vortex picture in the crossflow plane. Thus, for a pair of wing panels inclined at a positive angle of attack on a body whose axis is parallel to the free stream, the vortex paths trail below the free-stream direction with concavity upwards since there is no body upwash and the effect of the image vortices is to depress the wing vortex wake. For a pair of wing panels at a negative angle of attack on a body at a positive angle of attack, the trailing vortices are inclined upward since the body crossflow and vortex-induced velocities are additive.

These and all other computations except those with 10 vortices per wing panel were performed with a desk calculator. It was found that the solution of vortex paths downstream of the wing could be accomplished in about fifteen minutes per station for a single-wing vortex, and two hours per station for a three-wing vortex scheme. In general, the number of computations per solution increases approximately as the square of the number of vortices assigned per wing panel.

Evaluation of the Effect of Stepwise Integration on Vortex Paths

In the present line-vortex method, the principal factors governing the labor expended in the solution to a given problem are the size of the "time" increment $\Delta\mu$ and the number of vortices used to replace the trailing vorticity. The first factor will now be discussed in detail.

The necessity for a stepwise solution for vortex paths stems from the difficulty of integrating n simultaneous differential equations of vortex motion (eqs. (13) and (14), together with eqs. (18) and (19)). The differential equations are therefore solved with a small, finite $\Delta\mu$. In this report, the use of equations (21) and (22) implies the use of Euler's linear integration method, that is,

$$(\nu_i)_{\mu+\Delta\mu} = (\nu_i)_\mu + \left(\frac{d\nu_i}{d\mu}\right)_\mu \Delta\mu$$

where

$$\nu_i = \lambda_i \text{ or } \eta_i, \qquad \text{and} \qquad i = 1, 2, 3, \ldots \eta/2$$

A Taylor series expansion shows the higher order terms neglected:

$$(\nu_i)_{\mu+\Delta\mu} = (\nu_i)_\mu + \left(\frac{d\nu_i}{d\mu}\right)_\mu \Delta\mu + \left(\frac{d^2\nu_i}{d\mu^2}\right)_\mu \frac{\Delta\mu^2}{2!} + \left(\frac{d^3\nu_i}{d\mu^3}\right)_\mu \frac{\Delta\mu^3}{3!} + \ldots$$

Thus, it may be seen that the use of Euler's method without appreciable error requires either the second and higher derivatives to be small or $\Delta\mu$ to be small. The following discussion indicates the importance of the higher order terms for vortex motion.

Comparison of known exact solution of vortex motion with stepwise integration.- A simple example of the mutual interaction of two vortices, for which the exact solution is known, furnishes an insight into the nature of the cumulative error incurred by this stepwise-integration method. It is easily shown by the methods of hydrodynamics (e.g., p. 320 of ref. 19) that two vortices of strengths Γ_1 and Γ_2 will, due to their own mutual influence, each rotate about their common "centroid" in a circular path with constant angular velocity which is equal to $(\Gamma_1 + \Gamma_2)/2\pi$ divided by the square of the distance between the vortices. This motion is illustrated in figure 20. The solid lines radiating from the centroid represent the ends of a constant time increment (proportional to $\Delta\mu$) and the solid, spiral-like curves are the corresponding paths computed by a stepwise approximation. The dashed radial lines and spirals relate to a time interval half of that used before. It appears from figure 20 that the error or discrepancy between circular and spiral paths increases while the rate of growth of this error decreases with time (or distance downstream of the initial position). Further, it is seen that a decreased size of time increment results in a decreased error, for this example, in approximately the same ratio. Of course, this case of completely circular vortex motion cannot be solved accurately by Euler's linear scheme without using extremely small increments. However, for many of the computed vortex paths behind the configurations considered in this report it will now be shown that Euler's method is sufficiently accurate.

Effect of size of increment $\Delta\mu$ on computed vortex paths.- The error incurred by using the linear integration method can be judged by calculating vortex paths with different increments $\Delta\mu$ and extrapolating the results to $\Delta\mu = 0$. This has been done for single- and three-vortex schemes at $\alpha = 5^\circ$ and typical results appear in figures 21 and 22. Both figures show that the stepwise method employing finite increments $\Delta\mu$ yields results which converge fairly rapidly to the exact solution (for which $\Delta\mu \longrightarrow d\mu \longrightarrow 0$). Here the error, using a given value of $\Delta\mu$, is indicated by the difference between the value of λ or η extrapolated to $\Delta\mu = 0$ and the value of λ or η at the given value of $\Delta\mu$. As in figure 20, the error is seen to increase with time or distance μ downstream of the wing. For a single-vortex scheme (fig. 21), the error is approximately proportional to $\mu\Delta\mu$ and is small, in general. The error becomes greater and less predictable, for the same increment size, with a multiple-vortex scheme (fig. 22). A single-vortex scheme is therefore less subject to integration error than a multiple-vortex scheme. The reason why the error increases nonlinearly for the three-vortex scheme of figure 22 can be explained by reference to figure 22(c) which shows the projection of the vortex paths on the crossflow plane. For small values of μ the vortex paths are fairly linear, with the vortex position error given by figure 22(a) being small and essentially linear with $\Delta\mu$. Further downstream, as the effect of the rolling-up process becomes marked, the paths are seen to become spiral-like. Each vortex-position error curve becomes increasingly nonlinear as the vortex path approaches a maximum or minimum vertical position in the crossflow plane. The use of smaller increments $\Delta\mu$ then reveals the tendency toward convergence of the path to one of a lesser radius of curvature, as illustrated previously for the case of truly circular paths.

From these results it appears that the selection of a suitable increment $\Delta\mu$ for any given case should be made by trial calculation with several values of $\Delta\mu$ for a few stations downstream of the wing. As long as the computed vortex paths are relatively linear in the crossflow plane, the largest value of $\Delta\mu$ should be chosen which permits the extrapolated error in vortex location to be the maximum tolerable at the furthest downstream station at which downwash is desired; $\Delta\mu$ should be decreased locally wherever the vortex paths appear to be approaching a maximum or minimum height in the crossflow plane.

More accurate numerical integration schemes than Euler's method can be found in reference 20. Curve-fitting and extrapolation formulas are presented which by taking account of the higher order derivatives of the path enable one to maintain sufficient accuracy of vortex positions with a given $\Delta\mu$ even when the paths are markedly nonlinear.

Comparison of computed paths with exact solution for vortex paths in crossflow plane.- The exact solution known for the vortex path in the crossflow plane corresponding to the single-panel vortex representation mentioned previously can be used to check the accuracy of the stepwise integration. Equation (VI-4) of reference 13 cites the result obtained by Villat (ref. 18). In the present notation, it is:

$$2\lambda\left(1-\frac{1}{\xi^2}\right)-\frac{\Gamma}{4\pi V_o}\ln\left[\frac{4\lambda^2(\xi^2-1)^2}{(\xi^2-1)^2+4\lambda^2}\right]=2\lambda_o\left(1-\frac{1}{\lambda_o^2}\right)-\frac{\Gamma}{\pi V_o}\ln\left[\frac{2\lambda_o(\lambda_o^2-1)}{\lambda_o^2+1}\right] \tag{25}$$

where

$$\xi^2 = \lambda^2 + (\eta + \mu\alpha)^2$$

$$\lambda_o \equiv (\lambda)_{\mu=o}$$

At an infinite distance downstream the vortices are infinitely far removed from the body $(\eta + \mu\alpha \longrightarrow \infty)$ so that the asymptotic spacing $2(\lambda)_{\mu=\infty}$ of the vortex pair is given by the relation:

$$2(\lambda)_{\mu=\infty}-\frac{\Gamma}{2\pi V_o}\ln 2(\lambda)_{\mu=\infty}=2\lambda_o\left(1-\frac{1}{\lambda_o^2}\right)-\frac{\Gamma}{2\pi V_o}\ln\left[\frac{2\lambda_o(\lambda_o^2-1)}{\lambda_o^2+1}\right] \tag{26}$$

Two solutions by the stepwise method have been checked against equations (25) and (26). This has been done by inserting pairs of values of the coordinates μ and η, from the stepwise-calculated paths, into equation (25) and solving for the λ coordinate by trial. The comparison appears in figure 23, showing the results to be practically coincident.

Effect of Number of Vortices on Downwash at Tail Locations

Comparisons were made of the downwash along a line, representing a horizontal tail plane, resulting from the separate presence of one, three, and ten vortices, all derived from a given circulation distribution. Possible tail locations for both a missile-type and high-tail airplane-type configuration were chosen.

Missile-type configuration.- For the former, $\mu = 10$ was selected; that is, a tail location 10 body radii downstream of the wing trailing edge. Therefore downwash was first computed along the line $\mu = 10$, $\eta = -10 \tan \alpha$, $1 < \lambda < 6$, which is a horizontal line through the body center line of the missile-type configuration.

Figures 24(a) and (b) show the effect of number of vortices on downwash at the chosen missile tail location with and without components of the body potential crossflow in the stepwise computations. These omissions were made for two reasons: One was to determine the extent to which the stepwise calculations could be simplified without obtaining dissimilar results in downwash, and the other was an attempt to account for the flow around the body at high angles of attack. As an assumption for the high-angle-of-attack crossflow, the potential crossflow (eqs. (18) and (19)) was replaced by equation (18) alone with $\eta' \equiv 0$. This assumption implies that the velocity distribution on the lee side of the body is the same at any vertical station as along the horizontal diameter, as indicated in sketch (j).

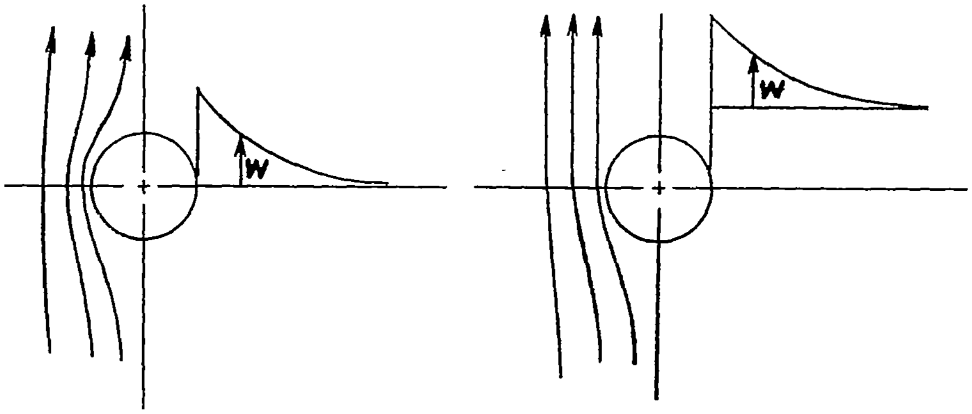

Potential crossflow. Assumed center line crossflow.

Sketch (j)

For the aspect ratio 2/3 configuration of figure 24(a), with $r/s_m = 0.6$, the number of vortices used has a negligibly small effect on downwash except when the body crossflow is entirely omitted in the stepwise calculations. Observance of the various vortex positions at the tail location, shown at the top of figure 24(a), shows that the vortices from the wing panels are subject to a relatively strong body crossflow so that their computed positions are greatly in error if the body upwash is neglected. Thus, when at least the upwash component of the body crossflow (the center line crossflow in sketch (j)) is added to the stepwise calculations there is no appreciable effect of either the number of vortices used or the strength distribution for a given multiple-vortex scheme. Figure 24(a) also shows that only a small change in downwash results from replacing the potential body crossflow by the assumed center line crossflow.

For the aspect ratio 4 wing and body combination of figure 24(b), with $r/s_m = 0.2$, it is seen that there is little effect of body crossflow on the downwash at the tail. This could be expected because of the relatively large wing. While the use of a single vortex does not adequately approximate the magnitude of downwash over a tailspan equal to the wingspan, a 3-vortex scheme appears to be as satisfactory as a 10-vortex scheme. Reference to the computed vortex locations shown at the top of the figure indicates that the vortex sheet from a high-aspect-ratio wing at low angles of attack rolls up so slowly and extends over such a large spanwise distance that a single vortex cannot give the correct distribution of downwash.

At higher angles of attack, the vortex wake will be even further from the horizontal tail plane because the body will be inclined below the free-stream direction more than the vortex wake according to figure 7. Although the vortex strengths increase directly with angle of attack, the downwash at the tail decreases very rapidly with distance from the wake. Consequently, the effect of number of vortices should be smaller at higher angles of attack.

Airplane-type configuration.- Now a possible horizontal tail location for a high-tail airplane-type configuration is $\mu = 3$ and $\eta \cong 2$, that is, 3 body radii downstream of the trailing edge of the wing and 2 body radii above the body axis. Figure 25 presents the effect of the number of vortices used on the downwash at this tail location. The aspect ratio 2/3 configuration of figure 25(a), with $r/s_m = 0.6$, shows no noticeable effect of number of vortices on either the distribution or magnitude of downwash simply because of the distance of the horizontal tail plane above the vortex wake. Neither is there any appreciable effect of assuming the body crossflow to be the center line crossflow. The aspect ratio 4 configuration of figure 25(b), with $r/s_m = 0.2$, shows that 3 vortices give the same downwash as 10 vortices. However, from figure 7 the vortex wake behind the wings of both high- and low-aspect-ratio configurations at small values of μ is seen to be fairly close to the free-stream direction at all angles of attack. Therefore it can be expected that with increasing angle of attack, the tail plane approaches the wing vortex wake and the use of at least three vortices to represent the wake behind wings of such high-tail airplane-type configurations will be required to obtain the correct magnitude of downwash across the tailspan.

To obtain the shape of a vortex wake behind a wing, clearly a multiple trailing-vortex system, such as the 10-vortex systems used herein, is required. However, for the computation of downwash at tail locations a minimum number of vortices is desirable and this number depends mainly on the distance between the wing wake and tail surfaces. The number varied from about one to three for the configurations studied herein, depending on whether that distance was large or small. An empirical relation, based on the calculations made in this study, for estimating the nearest integral number of vortices required per wing panel is:

$$N = 1 + \frac{0.16A}{\frac{r}{s_m}\left|h - \mu\alpha\right|}$$

where h is the height of the horizontal tail above the body axis in terms of body radii.

<u>Note on calculations involving large numbers of vortices</u>.- In setting up the initial (trailing-edge) vortex distribution from the given circulation distribution $\Gamma(y)$, one must exercise great care when n is large (i.e., $n > 20$). The spacing of the vortices which approximate $\Gamma(y)$ stepwise must be checked to insure a smooth curve of their divided differences. Otherwise, spurious effects such as the "loss" of a vortex, caused by excessive induced velocity, sketched below, can occur (see fig. 24(a)).

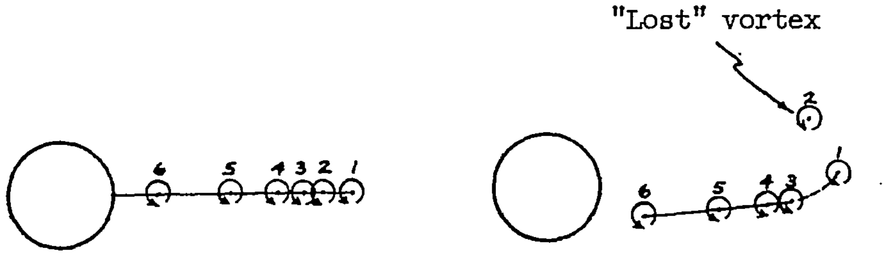

Initial vortex distribution at $\mu = 0$

Incorrect result at $\mu = \Delta\mu$ due to vortex No. 2

Sketch (k)

CONCLUSIONS

An investigation has been made of a line-vortex method for computing vortex paths, downwash, and sidewash behind wings of wing-body combinations. Application of the method to the calculation of wake shapes, vortex paths, and downwash behind triangular-wing and cylindrical-body combinations with various prescribed data leads to the following conclusions:

1. Wake shapes calculated by two-dimensional line-vortex theory agree qualitatively at least with wakes observed in a supersonic wind tunnel. Calculated vortex paths using this line-vortex method agree well with a known exact crossflow-plane solution.

2. A missile-type wing-body-tail combination with the horizontal tail located in the body diametral plane 10 body radii downstream of the wing trailing edge at 5° angle of attack was considered. It was found that if the plane wing is of low aspect ratio (order of 2/3), downwash can be computed at the horizontal tail from the wing vortices alone for small values of the ratio of body radius to wing semispan (order of 0.2) and from the body upwash alone for large values of that ratio (order of 0.7). For high-aspect-ratio wings (order of 4) on small bodies, downwash at the tail location can be well approximated only by considering all the flow components - wing vortices, image vortices, and body crossflow.

3. A multiple trailing-vortex system is, of course, required to determine the shape of the wake behind a wing. However, for the computations of downwash at a tail location the number of vortices required per panel depends mainly on the distance between the wing wake and tail surfaces. The number varies from about one to three for the configurations studied herein, depending on whether this distance is large or small. An empirical relation, based on the calculations made in this report, for estimating the nearest integral number of vortices N required per wing panel is:

$$N = 1 + \frac{0.16A}{\frac{r}{s_m}\left|h - \mu\alpha\right|}$$

where h is the height of the horizontal tail above the body axis, μ the distance of the tail from the wing trailing edge (both in terms of body radius), α is the angle of attack in radians, A is the wing aspect ratio, and r/s_m the ratio of body radius to wing semispan.

4. The rolling up of a vortex wake behind wings of unbanked wing-body combinations qualitatively resembles the wake pattern behind comparable isolated wings. The comma-shaped rolling-up pattern of the vortex wake behind a subsonic-leading-edge triangular wing panel, with

the eventual single-vortex core, is due to the nearly elliptic circulation distribution along the wing trailing edge. In contrast, a supersonic-leading-edge triangular wing panel generates an S-shaped vortex wake behind the portion of the trailing edge which has a linear circulation distribution, and the S-shaped wake eventually rolls up into two vortices.

5. The spanwise distance from the body of a single vortex representing the circulation distribution on one panel of a plane, subsonic-leading-edge wing and body combination is approximately constant and equal to about 0.76 times the exposed wing semispan for all ratios of body radius to wing semispan.

6. The type of vortex wake, and resultant downwash from a wing, is significantly affected by the circulation distribution along the wing trailing edge. It should be noted that the circulation distribution which must be used in setting up the initial vortex distribution along the wing trailing edge is not equivalent to span loading when the wings are in sideslip or the body noncylindrical.

Ames Aeronautical Laboratory
National Advisory Committee for Aeronautics
Moffett Field, Calif., June 1, 1954

APPENDIX A

NONEQUIVALENCE OF WING SPAN LOADING AND CIRCULATION DISTRIBUTION $\Gamma(y)$ ALONG THE TRAILING EDGE OF A WING

The circulation function Γ in fluid dynamics is defined by the contour integral:

$$\Gamma \equiv \oint \overline{q} \cdot \overline{ds}$$

where

$$\overline{q} \equiv u\overline{i} + v\overline{j} + w\overline{k}$$

and

$$\overline{ds} \equiv dx\overline{i} + dy\overline{j} + dz\overline{k}$$

Let Γ be evaluated around a streamwise chord of a flat plate such as AB in figure 13. Then:

$$\Gamma = \oint u \; dx_1 = \int_0^c u_u \; dx_1 + \int_c^0 u_l \; dx_1$$

where u_u means $(u)_{z \longrightarrow +0}$, and u_l means $(u)_{z \longrightarrow -0}$.

Within the limits of linear theory, $u_l = -u_u$, so that:

$$\Gamma = 2\int_0^c u_u \; dx_1 \qquad \text{or} \qquad \frac{\Gamma}{V_0} = 2\int_0^c \frac{u_u}{V_0} \; dx_1 \tag{A1}$$

The span loading on a wing is defined by the relation:

$$\frac{\partial L}{\partial y} = q\int_0^c \left(\frac{\Delta p}{q}\right)_W dx_1 \tag{A2}$$

From the Bernoulli equation one obtains the lifting pressure coefficient for a general wing-body combination as:

$$\frac{\Delta p}{q} = \frac{-2(u_l - u_u)}{V_0} - \frac{(v_l^2 - v_u^2) + (w_l^2 - w_u^2)}{V_0^2} \tag{A3}$$

For a noncylindrical body-wing combination, two linear crossflow velocity potentials must be added; φ_2 associated with a cylindrical body-wing combination and Φ_2 for an expanding body can be superposed as follows:

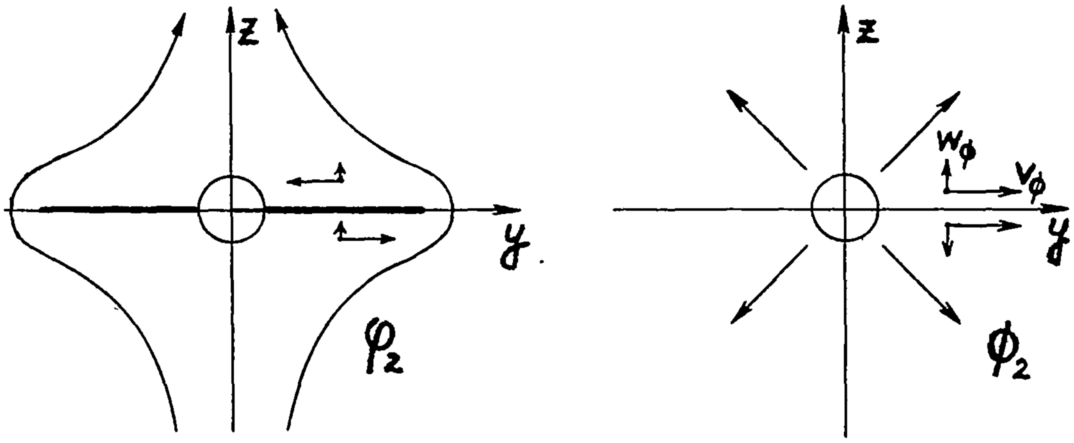

Sketch (l)

When the potential subscript 2 is dropped,

$$\left.\begin{aligned} u_l - u_u = f(\varphi) = -2u_{\varphi_u}, &\qquad w_l - w_u = g(\Phi) = -2w_{\Phi_u} = 0 \\ v_l = |v_{\varphi_l}| + |v_{\Phi_l}|, &\qquad v_u = |v_{\Phi_u}| - |v_{\varphi_u}| \\ v_l^2 - v_u^2 = 2|v_{\Phi_u}|(|v_{\varphi_l}| + &|v_{\varphi_u}|) = 4|v_{\Phi_u}||v_{\varphi_u}| \end{aligned}\right\} \qquad (A4)$$

using the symmetrical properties of each potential.

Substituting equations (A4) into (A3), one has:

$$\left(\frac{\Delta p}{q}\right)_W = \frac{4u_\varphi}{V_o} - \frac{4v_\Phi v_\varphi}{V_o^2} \qquad (A5)$$

where the derivatives are evaluated on the wing $(z = 0)$. Equation (4) in the text is the result of substituting the expressions for potentials φ and Φ in equation (A5). It can thus be seen that the second term in equation (4) representing the contribution of the spanwise velocities (the second term of eq. (A5)), can be of the same order of magnitude as the first term, and not negligible as in the linearized theory for wings alone.[1]

---

[1] The above derivation appears in reference 21 where it is pointed out that for axisymmetric bodies, crossflow velocities may considerably exceed axial velocities, that is, $O(u) < O(v)$.

Now the span loading is obtained by substituting equation (A5) in (A2):

$$\frac{\partial L}{\partial y} = q\int_0^c 4\,\frac{u_\varphi}{V_o}\,dx_1 - q\int_0^c 4\,\frac{v_\varphi v_\Phi}{{V_o}^2}\,dx_1$$

and using equation (A1):

$$\frac{\partial L}{\partial y} = 2q\,\frac{\Gamma}{V_o} - \frac{4q}{{V_o}^2}\int_0^c v_\varphi v_\Phi dx_1 \tag{A6}$$

Thus it is seen that the span loading along the wing trailing edge of a noncylindrical body-wing combination differs from the circulation distribution by the last integral term. In fact, it can be shown, by writing equation (A3) in terms of velocity potential and comparison with equation (7), that to any order theory span loading is not equivalent to circulation distribution as long as sideslip angle of flow is not zero or the body noncylindrical. For a banked cruciform configuration, therefore, this nonequivalence is always present.

APPENDIX B

CORRECTION OF SLENDER-BODY THEORY TO ACCOUNT FOR MODERATE ASPECT RATIO

The theory developed in reference 15, for the lift of wings and wing-body combinations, is based on the assumption of slenderness. The aspect ratio of the configuration analyzed by this theory must be low enough so that the wings are near the axis of the Mach cone. A correction factor is required, therefore, to apply slender-body results to higher-aspect-ratio wings according to the formula:

$$L_{W+B} = (k)(L_{W+B})_{SBT} \tag{B1}$$

The correction factor k is obtained by comparison of slender-body theory with the more exact linear theory (applicable to high-aspect-ratio wings) for triangular wings (ref. 22), that is:

$$k \equiv \frac{(L_W)_{LT}}{(L_W)_{SBT}} \tag{B2}$$

It has here been assumed that this wing aspect-ratio factor k can be used for the winged portion of wing-body combinations and for other than triangular-wing plan forms. Thus one can correct the lift of a higher-aspect-ratio configuration by means of equation (B1). This assumption is justified for small values of the parameter $\beta \tan \omega$ (see fig. 26) when k is approximately one, and slender-body theory is itself applicable. Satisfactory results should also be obtained for large wing-to-body area ratios since the wing then carries the major portion of the lift of the combination. Experimental data confirm the validity of these assumptions for wing-body configurations of aspect ratios on the order of 1 to 4.

For triangular wings with subsonic leading edges, the lift distribution given by linear theory has the same shape as that given by slender-body theory. Therefore the k factor can be defined as in equation (B2) by total lift ratios, and is independent of the spanwise coordinate y. For such wings, the method of reference 15 (applied to wings alone) yields results identical to the low-aspect-ratio triangular-wing results of Jones (ref. 23). However, it is known that Jones' results overestimate lift-curve slope when the parameter $\beta \tan \omega$ is not small relative to unity. The factor by which lift-curve slopes calculated by slender-body theory must be multiplied to agree with linear theory is given as:

$$\left.\begin{aligned} k &= \frac{1}{E\left(\sqrt{1-\beta^2 \tan^2 \omega}\right)} \qquad \beta \tan \omega \leq 1 \\ k &= \frac{2}{\pi \beta \tan \omega} \qquad \beta \tan \omega \geq 1 \end{aligned}\right\} \tag{B3}$$

These equations have been plotted in figure 26.

However, for supersonic leading edges ($\beta \tan \omega > 1$), the lift distributions are not functionally identical so that equation (B1) must be written in terms of local chord lift. Then k becomes a function of y, namely, the ratio of section lifts or circulation by linear and slender-body theory. Now in linear theory, the pressure coefficient on a supersonic-leading-edge triangular wing outboard of the Mach line is:

$$\frac{\Delta p}{q} = \frac{4\alpha}{\sqrt{\beta^2 - \tan^2 \Lambda}} \tag{B4}$$

Substitution of this expression in equation (1) yields the circulation distribution (in this case equivalent to the span loading):

$$\Gamma(y) = \frac{2V_o\alpha \tan \Lambda(s_m - y)}{\sqrt{\beta^2 - \tan^2 \Lambda}} \tag{B5}$$

For a wing alone $r = 0$ in equation (3), thus giving the slender-body theory result:

$$\Gamma(y) = 2V_o\alpha\sqrt{{s_m}^2 - y^2} \tag{B6}$$

Hence, for the part of the wing trailing edge outboard of the Mach cone, the factor k for a wing-body combination is the ratio of equation (B5) to (B6), or:

$$k = \frac{1}{\sqrt{\beta^2 \tan^2 \omega - 1}} \sqrt{\frac{s_m - y}{s_m + y}} \tag{B7}$$

for

$$r + \frac{s_m - r}{\beta \tan \omega} \leq y \leq s_m$$

Fortunately, the accuracy of the k factor can be checked in this case since an exact answer for $\Gamma(y)$ for the wing-body combination can be calculated by linear theory without excessive labor. Referring to figure 27, at any point $P(x,y)$ on the wing trailing edge outboard of the point of intersection of the Mach cone with the trailing edge, the potential φ_3 can be evaluated by integration of the distribution of sources at points (σ,τ) within the forecone of P, that is:

$$\varphi_3(x,y) = -\frac{V_o}{\pi}\iint\limits_{\substack{\text{forecone}\\ \text{of P}}} \frac{\alpha}{r_n}\,d\sigma\,d\tau \tag{B8}$$

where, in the plane of the wing $(z = 0)$, the hyperbolic radius r_n is:

$$r_n = \sqrt{(x-\sigma)^2 - \beta^2(y-\tau)^2} \tag{B9}$$

and the angle of attack α is the sum of the body angle of attack, α_B, and the body angle of upwash:

$$\alpha = \alpha_B\left(1 + \frac{r^2}{\tau^2}\right) \tag{B10}$$

On the wing, the forecone of point P produces the shaded area shown with the corresponding boundaries of integration. Thus:

$$\varphi_3(x,y) = -\frac{V_o\alpha_B}{\pi}\left[\int_{\frac{\beta y-x}{\beta-\tan\Lambda}}^{y} d\tau \int_{\tau\tan\Lambda}^{x-\beta(y-\tau)} \frac{\left(1+\frac{r^2}{\tau^2}\right)d\sigma}{\sqrt{(x-\sigma)^2-\beta^2(y-\tau)^2}} + \int_{y}^{\frac{\beta y+x}{\beta+\tan\Lambda}} d\tau \int_{\tau\tan\Lambda}^{x+\beta(y-\tau)} \frac{\left(1+\frac{r^2}{\tau^2}\right)d\sigma}{\sqrt{(x-\sigma)^2-\beta^2(y-\tau)^2}}\right] \tag{B11}$$

The integrals not containing r have been evaluated in reference 24, and in the present coordinate system give:

$$\varphi_4 = -\frac{V_o\alpha_B(x-y\tan\Lambda)}{\sqrt{\beta^2-\tan^2\Lambda}} \tag{B12}$$

The integrals containing r^2/τ^2 yield:

$$\varphi_5 = -\frac{V_o\alpha_B r^2(x-y\tan\Lambda)}{y\sqrt{\beta^2y^2-x^2}} \tag{B13}$$

Therefore the total potential at P is $\varphi_3 = \varphi_4 + \varphi_5$ or:

$$\varphi_3(x,y) = -V_o\alpha_B(x-y\tan\Lambda)\left(\frac{1}{\sqrt{\beta^2-\tan^2\Lambda}} + \frac{r^2}{y\sqrt{\beta^2y^2-x^2}}\right) \tag{B14}$$

The circulation distribution $\Gamma(y)$ along the wing trailing edge $x = c_r$ is then (see eq. (7)):

$$\Gamma(y)_{TE} = 2V_o\alpha_B\tan\Lambda(s_m-y)\left(\frac{1}{\sqrt{\beta^2-\tan^2\Lambda}} + \frac{r^2}{y\sqrt{\beta^2y^2-s_m{}^2\tan^2\Lambda}}\right) \tag{B15}$$

where

$$r + \frac{s_m-r}{\beta}\tan\Lambda \leq y \leq s_m$$

Thus equation (B15) furnishes the linear-theory answer for $\Gamma(y)$ along the trailing edge outside of the Mach cone, while equation (3) multiplied by equation (B7) is the approximation to the linear theory assumed by equation (B1) with $k = k(y)$. This approximation is compared with linear theory in figure 28 at the spanwise position of the Mach line $y = r + (s_m-r)/\beta\tan\omega$ for various values of r/s_m as a function of $\beta\tan\omega$. It is seen that the approximation assumed by equation (B1) with $k = k(y)$ is satisfactory, producing a maximum error of about 20 percent and only about 10 percent for the range of the parameter $\beta\tan\omega$ from 0 to 4.

For the region of the wing inboard of the Mach cone, the pressure coefficient given by linear theory is (for a wing alone):

$$\frac{\Delta p}{q} = \frac{4\alpha}{\sqrt{\beta^2-\tan^2\Lambda}}\left[1 + \frac{1}{\pi}\sin^{-1}\frac{\frac{y}{x}\beta^2\cot\Lambda - 1}{\beta\left(\cot\Lambda - \frac{y}{x}\right)} - \frac{1}{\pi}\sin^{-1}\frac{\frac{y}{x}\beta^2\cot\Lambda + 1}{\beta\left(\cot\Lambda + \frac{y}{x}\right)}\right] \tag{B16}$$

Integration of equation (1) then results in:

$$\Gamma(y)_{TE} = \frac{2V_o\alpha}{\sqrt{\beta^2 \tan^2 \omega - 1}} \left\{ s_m + \frac{1}{\pi}\left[(s_m - y)\sin^{-1} \frac{y\beta^2 \tan^2 \omega - s_m}{(s_m - y)\beta \tan \omega} - (s_m + y)\sin^{-1} \frac{y\beta^2 \tan^2 \omega + s_m}{(s_m + y)\beta \tan \omega} \right] \right\} \tag{B17}$$

Therefore the factor $k(y)$ to be used for $\Gamma(y)$ along the wing trailing edge inboard of the Mach cone is the ratio of equation (B17) to equation (B6) or:

$$k(y) = \frac{1}{\sqrt{(s_m{}^2 - y^2)(\beta^2 \tan^2 \omega - 1)}} \left\{ s_m + \frac{1}{\pi}\left[(s_m - y)\sin^{-1} \frac{y\beta^2 \tan^2 \omega - s_m}{(s_m - y)\beta \tan \omega} - (s_m + y)\sin^{-1} \frac{y\beta^2 \tan^2 \omega + s_m}{(s_m + y)\beta \tan \omega} \right] \right\} \tag{B18}$$

for

$$r \leq y \leq r + \frac{s_m - r}{\beta \tan \omega}$$

REFERENCES

1. Allen, H. Julian, and Perkins, Edward W.: A Study of Effects of Viscosity on Flow Over Slender Inclined Bodies of Revolution. NACA Rep. 1048, 1951.

2. Lagerstrom, P. A., and Graham, Martha E.: Downwash and Sidewash Induced by Three-Dimensional Lifting Wings in Supersonic Flow. Rep. SM-13007, Douglas Aircraft Co., Inc., Apr. 14, 1947.

3. Lomax, Harvard, Sluder, Loma, and Heaslet, Max. A.: The Calculation of Downwash Behind Supersonic Wings With an Application to Triangular Plan Forms. NACA Rep. 957, 1950.

4. Ward, G. N.: Calculation of Downwash Behind a Supersonic Wing. Aero. Quart., vol. 1, pt. 1, May 1949, pp. 35-38.

5. Martin, John C.: The Calculation of Downwash Behind Wings of Arbitrary Plan Form at Supersonic Speeds. NACA TN 2135, 1950.

6. Robinson, A., and Hunter-Tod, J. H.: Bound and Trailing Vortices in the Linearised Theory of Supersonic Flow, and the Downwash in the Wake of a Delta Wing. Rep. 10, Coll. of Aero., Cranfield, Oct. 1947.

7. Mirels, Harold, and Haefeli, Rudolph C.: Line-Vortex Theory for Calculation of Supersonic Downwash. NACA Rep. 983, 1949. (Formerly NACA TN 1925.) (See also Jour. Aero. Sci., vol. 17, no. 1, Jan. 1950, pp. 13-21.)

8. Haefeli, Rudolph C., Mirels, Harold, and Cummings, John L.: Charts for Estimating Downwash Behind Rectangular, Trapezoidal, and Triangular Wings at Supersonic Speeds. NACA TN 2141, 1950.

9. Lagerstrom, P. A., and Graham, Martha E.: Methods for Calculating the Flow in the Trefftz-Plane Behind Supersonic Wings. Rep. SM-13288, Douglas Aircraft Co., Inc., July 28, 1948.

10. Graham, Martha E.: Some Linearized Computations of Supersonic Wing-Tail Interference. Rep. SM-13430, Douglas Aircraft Co., Inc., Dec. 23, 1948.

11. Spreiter, John R., and Sacks, Alvin H.: The Rolling Up of the Trailing Vortex Sheet and its Effect on the Downwash Behind Wings. Jour. Aero. Sci., vol. 18, no. 1, Jan. 1951, pp. 21-32.

12. Sacks, Alvin H.: Behavior of Vortex System Behind Cruciform Wings - Motions of Fully Rolled-Up Vortices. NACA TN 2605, 1952.

13. Lagerstrom, P. A., and Graham, Martha E.: Aerodynamic Interference in Supersonic Missiles. Rep. SM-13743, Douglas Aircraft Co., Inc., July 1950.

14. Lomax, Harvard, and Byrd, Paul F.: Theoretical Aerodynamic Characteristics of a Family of Slender Wing-Tail-Body Combinations. NACA TN 2554, 1951.

15. Spreiter, John R.: The Aerodynamic Forces on Slender Plane- and Cruciform-Wing and Body Combinations. NACA Rep. 962, 1950.

16. Westwater, F. L.: The Rolling Up of the Surface of Discontinuity Behind an Aerofoil of Finite Span. R. & M. No. 1692, British A.R.C., 1935.

17. Lennertz, J.: Influence of the Airplane Body on the Wings. Vol. IV of Aerodynamic Theory, div. K, ch. III, sec. 1, W. F. Durand, ed., Julius Springer (Berlin), 1935, pp. 152-157. (Reprinted, C.I.T., Jan. 1943)

18. Villat, Henri: Lecons sur la Theorie des Tourbillons. Gauthier-Villars et Cie, Paris, 1930.

19. Milne-Thomson, L. M.: Theoretical Hydrodynamics. Second ed., The MacMillan Co., New York, 1950.

20. Milne, William Edmund: Numerical Solution of Differential Equations. John Wiley and Sons, Inc., New York, 1953.

21. Spreiter, John R.: On Slender Wing-Body Theory. Jour. Aero. Sci., vol. 19, no. 8, Aug. 1952, pp. 571-572.

22. Brown, Clinton E.: Theoretical Lift and Drag of Thin Triangular Wings at Supersonic Speeds. NACA Rep. 839, 1946.

23. Jones, Robert T.: Properties of Low-Aspect-Ratio Pointed Wings at Speeds Below and Above the Speed of Sound. NACA Rep. 835, 1946.

24. Puckett, Allen E.: Supersonic Wave Drag of Thin Airfoils. Jour. Aero. Sci., vol. 13, no. 9, Sept. 1946, pp. 475-484.

TABLE I.- VORTEX COORDINATES λ, η VERSUS DOWNSTREAM DISTANCE μ FOR 10-VORTEX CALCULATION OF FIGURE 3

μ	λ_1	η_1	λ_2	η_2	λ_3	η_3	λ_4	η_4	λ_5	η_5	λ_6	η_6	λ_7	η_7	λ_8	η_8	λ_9	η_9	λ_{10}	η_{10}
0	4.98400	0	4.94130	0	4.85070	0	4.70670	0	4.50530	0	4.24130	0	3.90130	0	3.45730	0	2.86400	0	1.95200	0
.5	4.98400	.23998	4.94130	-.01831	4.85070	-.03362	4.70670	-.03563	4.50530	-.03633	4.24130	-.03728	3.90130	-.03797	3.45730	-.03784	2.86400	-.03765	1.95200	-.03526
1.0	4.92143	.28803	4.95033	.10055	4.87897	-.02834	4.72001	-.06016	4.51151	-.06944	4.24436	-.07355	3.90287	-.07558	3.45808	-.07555	2.86441	-.07525	1.95219	-.07050
1.5	4.84318	.31648	4.92515	.17185	4.92378	.02114	4.75109	-.06926	4.52619	-.09760	4.25135	-.10814	3.90634	-.11259	3.45976	-.11303	2.86527	-.11276	1.95258	-.10571
2.0	4.75866	.31859	4.88702	.22868	4.96182	.08524	4.79233	-.06294	4.54893	-.11897	4.26259	-.14019	3.91191	-.14866	3.46244	-.15015	2.86662	-.15012	1.95319	-.14086
2.5	4.68296	.29273	4.84010	.27330	4.98181	.16389	4.83678	-.04277	4.57839	-.13322	4.27818	-.16931	3.91972	-.18359	3.46618	-.18683	2.86848	-.18732	1.95402	-.17595
3.0	4.62884	.24905	4.78430	.30620	4.97680	.24657	4.87955	-.00890	4.61361	-.14027	4.29810	-.19549	3.92964	-.21733	3.47102	-.22301	2.87088	-.22432	1.95509	-.21096
3.5	4.59820	.20169	4.72124	.32493	4.94880	.32197	4.91594	.03732	4.65389	-.13972	4.32229	-.21884	3.94224	-.24986	3.47696	-.25866	2.87361	-.26110	1.95639	-.24587
4.0	4.58598	.15991	4.65501	.32797	4.90388	.38496	4.94209	.09296	4.69812	-.13073	4.35062	-.23940	3.95683	-.28113	3.48398	-.29372	2.87728	-.29762	1.95792	-.28067
4.5	4.58614	.12765	4.58997	.31587	4.84791	.43347	4.95581	.15421	4.74471	-.11227	4.38291	-.25704	3.97350	-.31103	3.49207	-.32811	2.88129	-.33384	1.95969	-.31535
5.0	4.59374	.10589	4.52993	.28941	4.78544	.46752	4.95656	.21742	4.79101	-.08360	4.41894	-.27141	3.99217	-.33946	3.50123	-.36179	2.88586	-.36975	1.96171	-.34990
5.5	4.60489	.09419	4.47832	.25138	4.71987	.48787	4.94484	.27962	4.83309	-.04492	4.45842	-.28199	4.01282	-.36632	3.51146	-.39472	2.89099	-.40533	1.96398	-.38431
6.0	4.61648	.09120	4.43795	.20484	4.65376	.49556	4.92163	.33851	4.87047	.00257	4.50097	-.28813	4.03544	-.39156	3.52277	-.42688	2.89669	-.44055	1.96650	-.41856
6.5	4.62633	.09485	4.41028	.15392	4.58909	.49179	4.88814	.39225	4.89880	.05615	4.54606	-.28912	4.06005	-.41516	3.53514	-.45828	2.90296	-.47541	1.96928	-.45265
7.0	4.63346	.10290	4.39499	.10269	4.52743	.47781	4.84576	.43934	4.91792	.11415	4.59298	-.28426	4.08668	-.43713	3.54855	-.48693	2.90980	-.50991	1.97232	-.48658
7.5	4.63784	.11362	4.39052	.05418	4.47002	.45491	4.79606	.47858	4.92760	.17440	4.64079	-.27297	4.11594	-.45749	3.56297	-.51893	2.91719	-.54402	1.97562	-.52033
8.0	4.63985	.12598	4.39493	.01020	4.41783	.42444	4.74074	.50910	4.92793	.23525	4.68832	-.25487	4.14601	-.47683	3.57835	-.54797	2.92513	-.57774	1.97918	-.55390
8.5	4.63981	.13953	4.40652	-.02835	4.37161	.38770	4.68156	.53041	4.91918	.29531	4.73428	-.22990	4.17867	-.49333	3.59466	-.57653	2.93361	-.61105	1.98300	-.58728
9.0	4.63784	.15405	4.42396	-.06100	4.33189	.34598	4.62022	.54240	4.90174	.35331	4.77735	-.19832	4.21324	-.50870	3.61186	-.60389	2.94262	-.64392	1.98708	-.62046
9.5	4.63383	.16934	4.44618	-.08743	4.29906	.30053	4.55827	.54568	4.87614	.40808	4.81655	-.16071	4.24963	-.52223	3.62993	-.63062	2.95216	-.67637	1.99143	-.65343
10.0	4.62762	.18512	4.47224	-.10736	4.27332	.25259	4.49707	.53950	4.84306	.45858	4.85032	-.11789	4.28769	-.53378	3.64884	-.65649	2.96222	-.70838	1.99604	-.68619

TABLE II.- VORTEX COORDINATES λ, η VERSUS DOWNSTREAM DISTANCE μ FOR 10-VORTEX CALCULATION OF FIGURE 4

μ	λ_1	η_1	λ_2	η_2	λ_3	η_3	λ_4	η_4	λ_5	η_5	λ_6	η_6	λ_7	η_7	λ_8	η_8	λ_9	η_9	λ_{10}	η_{10}
0	4.89330	0	4.67200	0	4.45870	0	4.24400	0	4.02530	0	3.80930	0	3.59200	0	3.36000	0	2.85600	0	1.94400	0
.5	4.89330	.03242	4.67200	.01934	4.45870	.01073	4.24400	.00422	4.02530	-.00095	3.80930	-.00712	3.59200	-.01471	3.36000	-.02469	2.85600	-.01778	1.94400	-.00967
1.0	4.89174	.06476	4.67160	.03868	4.45867	.02147	4.24409	.00845	4.02530	-.00190	3.80944	-.01424	3.59250	-.02941	3.36128	-.04933	2.85618	-.03555	1.94414	-.01933
1.5	4.88861	.09698	4.67080	.05800	4.45862	.03222	4.24428	.01269	4.02529	-.00283	3.80971	-.02134	3.59349	-.04408	3.36385	-.07393	2.85654	-.05329	1.94442	-.02899
2.0	4.88392	.12903	4.66961	.07729	4.45854	.04296	4.24456	.01693	4.02526	-.00373	3.81011	-.02840	3.59498	-.05869	3.36771	-.09848	2.85709	-.07099	1.94484	-.03861
2.5	4.87766	.16088	4.66804	.09652	4.45844	.05369	4.24494	.02117	4.02521	-.00458	3.81063	-.03541	3.59694	-.07322	3.37287	-.12297	2.85783	-.08863	1.94539	-.04819
3.0	4.86981	.19246	4.66612	.11568	4.45833	.06441	4.24543	.02540	4.02512	-.00536	3.81125	-.04234	3.59936	-.08766	3.37935	-.14741	2.85875	-.10618	1.94608	-.05771
3.5	4.86035	.22373	4.66387	.13475	4.45822	.07511	4.24605	.02962	4.02497	-.00606	3.81196	-.04918	3.60222	-.10198	3.38718	-.17176	2.85987	-.12363	1.94690	-.06717
4.0	4.84923	.25462	4.66135	.15374	4.45813	.08580	4.24681	.03383	4.02474	-.00666	3.81273	-.05592	3.60549	-.11617	3.39639	-.19602	2.86118	-.14097	1.94785	-.07656
4.5	4.83642	.28505	4.65860	.17264	4.45807	.09647	4.24772	.03802	4.02440	-.00719	3.81353	-.06256	3.60912	-.13021	3.40703	-.22015	2.86269	-.15817	1.94892	-.08586
5.0	4.82185	.31495	4.65569	.19147	4.45807	.10714	4.24881	.04220	4.02391	-.00753	3.81433	-.06908	3.61308	-.14411	3.41914	-.24412	2.86440	-.17522	1.95011	-.09507
5.5	4.80547	.34419	4.65270	.21025	4.45814	.11781	4.25011	.04635	4.02324	-.00778	3.81510	-.07549	3.61731	-.15787	3.43279	-.26787	2.86631	-.19212	1.95141	-.10417
6.0	4.78719	.37265	4.64971	.22902	4.45830	.12850	4.25164	.05049	4.02234	-.00790	3.81580	-.08179	3.62174	-.17149	3.44805	-.29133	2.86843	-.20884	1.95282	-.11317
6.5	4.76692	.40018	4.64684	.24786	4.45857	.13924	4.25344	.05461	4.02117	-.00788	3.81639	-.08799	3.62630	-.18498	3.46500	-.31443	2.87076	-.22538	1.95433	-.12209
7.0	4.74457	.42655	4.64420	.26687	4.45896	.15005	4.25555	.05873	4.01968	-.00772	3.81684	-.09410	3.63091	-.19839	3.48373	-.33704	2.87331	-.24174	1.95594	-.13081
7.5	4.72004	.45149	4.64192	.28622	4.45948	.16097	4.25800	.06284	4.01782	-.00742	3.81711	-.10015	3.63546	-.21176	3.50434	-.35900	2.87608	-.25791	1.95764	-.13944
8.0	4.69325	.47464	4.64011	.30614	4.46013	.17205	4.26083	.06695	4.01553	-.00699	3.81717	-.10617	3.63984	-.22519	3.52695	-.38013	2.87908	-.27388	1.95942	-.14793
8.5	4.66417	.49553	4.63883	.32696	4.46091	.18354	4.26409	.07109	4.01276	-.00644	3.81700	-.11220	3.64393	-.23882	3.55166	-.40017	2.88231	-.28965	1.96128	-.15628
9.0	4.63289	.51358	4.63803	.34914	4.46180	.19491	4.26783	.07526	4.00946	-.00578	3.81658	-.11829	3.64761	-.25283	3.57857	-.41878	2.88578	-.30523	1.96322	-.16450
9.5	4.59970	.52808	4.63744	.37318	4.46280	.20685	4.27210	.07951	4.00559	-.00505	3.81590	-.12451	3.65079	-.26751	3.60775	-.43553	2.88949	-.32062	1.96523	-.17257
10.0	4.56522	.53831	4.63645	.39962	4.46391	.21924	4.27694	.08386	4.00110	-.00427	3.81497	-.13094	3.65345	-.28320	3.63918	-.44988	2.89344	-.33583	1.96730	-.18050

TABLE III.- SINGLE WING VORTEX FORM

(a) $\alpha = 5^\circ$; $\varphi = 0^\circ$; $M = 2$; $r = 3/4$; $\mu = 0$; $\Delta\mu = 1$

Vortex-induced velocities

Vortex No. j	$\frac{\Gamma_j}{V_0}$	λ_j	η_j	$\lambda_1 - \lambda_j$ λ_1 - ③	$\eta_1 - \eta_j$ η_1 - ④	⑤^2 + ⑥^2	$\dot{\eta}_1$ ② × ⑤/⑦	$\dot{\lambda}_1$ -② × ⑥/⑦	$\frac{1}{2\pi r}\sum \dot{\eta}_1$	$\frac{1}{2\pi r}\sum \dot{\lambda}_1$
①	②	③	④	⑤	⑥	⑦	⑧	⑨	⑩	⑪
1	0.12796	1.50870	0	0	0	0	0	0	-0.02860	0
2	-.12796	.66284	0	.84586	0	.71548	-.15128	0		
3	.12796	-.66284	0	2.17154	0	4.71559	.05893	0		
4	-.12796	-1.50870	0	3.01740	0	9.10470	-.04241	0		

Crossflow velocities

$\eta_1 + \mu \tan \alpha$	λ_1^2	⑫^2	(⑬ + ⑭)^2	⑬ - ⑭	$-2\lambda_1$ × ⑫	α × ⑯/⑮	α × ⑰/⑮	$\Delta\mu$(⑩ + ⑱)	$\Delta\mu$(⑩ + ⑲)	η_1 + ⑳	λ_1 + ㉑
⑫	⑬	⑭	⑮	⑯	⑰	⑱	⑲	⑳	㉑	㉒	㉓
0	2.27618	0	5.18100	2.27618	0	0.03834	0	0.00974	0	0.00974	1.50870

Image vortex position

$\mu + \Delta\mu$	$\tan \alpha$	㉔ × ㉕	λ_1 + ⑳	η_1 + ㉑	㉖ + ㉘	㉗^2 + ㉙^2	λ_2 = ㉗/㉚	㉙/㉚	η_2 = - ㉖ + ㉜
㉔	㉕	㉖	㉗	㉘	㉙	㉚	㉛	㉜	㉝
1	0.08749	0.08749	1.50870	0.00974	0.09723	2.28563	0.66008	0.04254	-0.04495

NACA

TABLE III.- SINGLE WING VORTEX FORM

(b) $\alpha = 5^{\circ}$; $\varphi = 0^{\circ}$; $M = 2$; $r = 3/4$; $\mu = 1$; $\Delta\mu = 1$ - Concluded

Vortex induced velocities										
Vortex No. j	$\frac{\Gamma_j}{V_0}$	λ_j	η_j	$\lambda_1 - \lambda_j$ λ_1 - ③	$\eta_1 - \eta_j$ η_1 - ④	⑤^2 + ⑥^2	$\dot{\eta}_1$ ② × ⑤/⑦	$\dot{\lambda}_1$ -② × ⑥/⑦	$\frac{1}{2\pi r}\sum \dot{\eta}_1$	$\frac{1}{2\pi r}\sum \dot{\lambda}_1$
①	②	③	④	⑤	⑥	⑦	⑧	⑨	⑩	⑪
1	0.12796	1.50870	0.00974	0	0	0	0	0	-0.02835	-0.00174
2	-.12796	.66008	-.04495	.84862	.05469	.72315	-.15016	.00968		
3	.12796	-.66008	-.04495	2.16878	.05469	4.70660	.05896	-.00149		
4	-.12796	-1.50870	.00974	3.01740	0	9.10470	-.04241	0		

Crossflow velocities											
$\eta_1 + \mu \tan \alpha$	λ_1^2	⑪^2	(⑫ + ⑬)^2	⑫ - ⑬	$-2\lambda_1$ × ⑪	α × ⑯ / ⑮	α × ⑰ / ⑮	$\Delta\mu$(⑩ + ⑱)	$\Delta\mu$(⑩ + ⑲)	η_1 + ⑳	λ_1 + ㉑
⑫	⑬	⑭	⑮	⑯	⑰	⑱	⑲	⑳	㉑	㉒	㉓
0.09723	2.27618	0.00945	5.22410	2.26673	-0.029338	0.03787	-0.00500	0.00952	-0.00674	0.01926	1.50196

Image vortex position									
$\mu + \Delta\mu$	$\tan \alpha$	㉔ × ㉕	λ_1 + ⑳	η_1 + ㉑	㉖ + ㉘	㉗^2 + ㉙^2	λ_2 = ㉗ / ㉚	㉙ / ㉚	η_2 = - ㉖ + ㉜
㉔	㉕	㉖	㉗	㉘	㉙	㉚	㉛	㉜	㉝
2	0.08749	0.17498	1.50196	0.01926	0.19424	2.29361	0.65485	0.08469	-0.09029

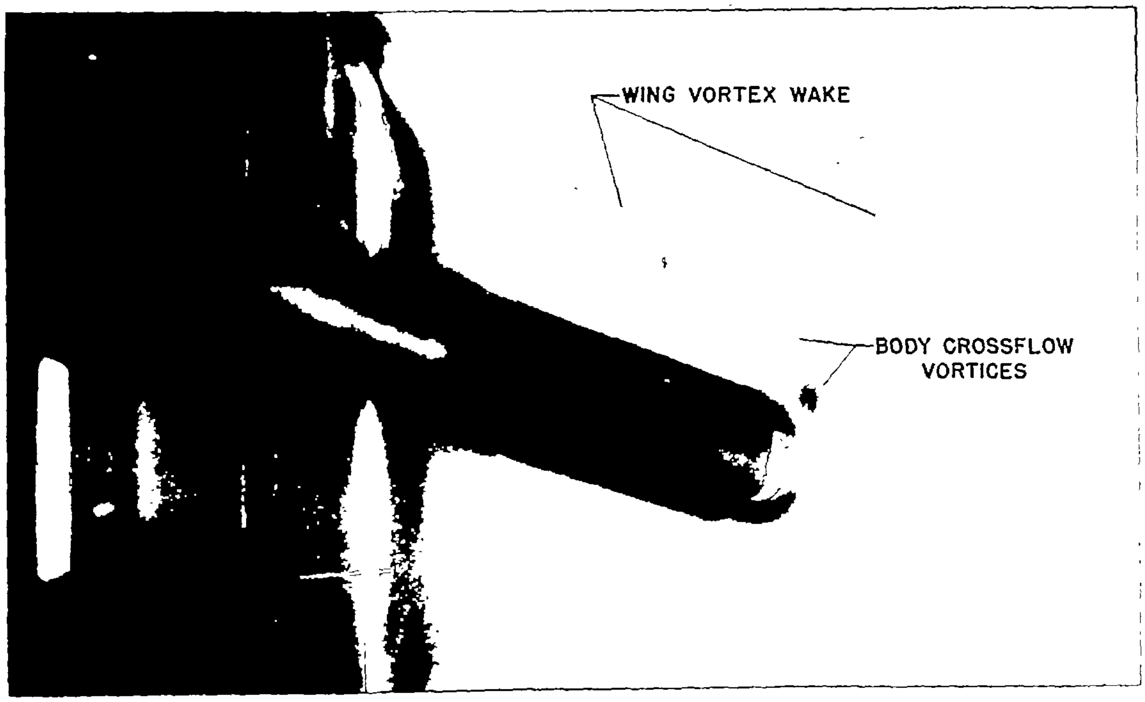

(a) Vapor-screen photograph.

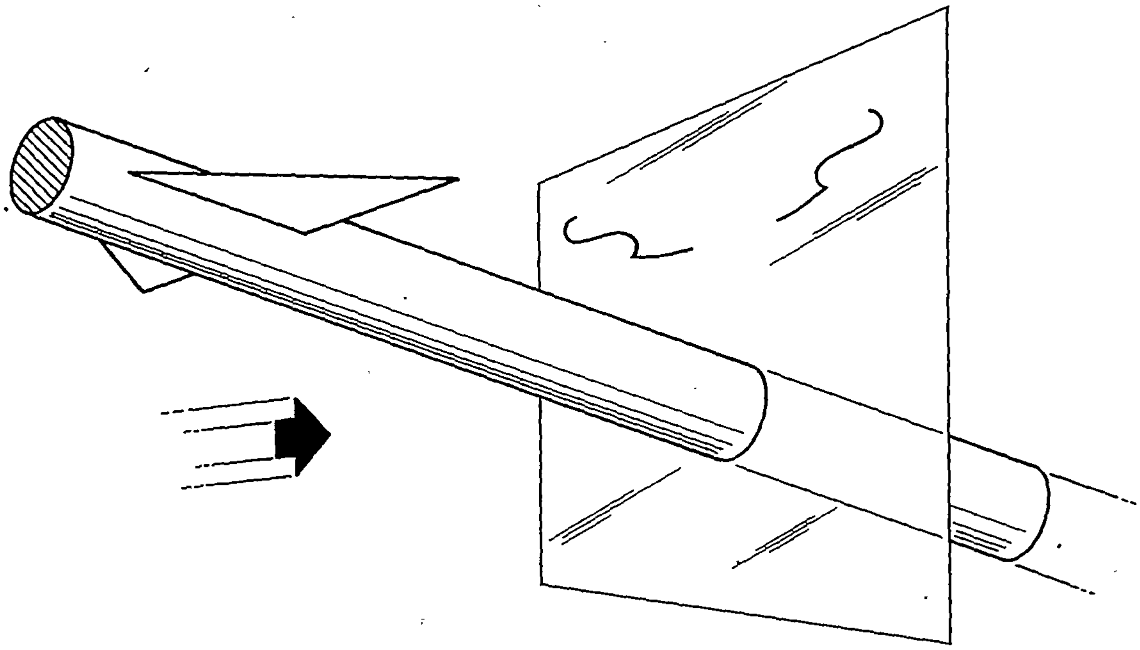

(b) Calculated theoretical wing vortex wake.

Figure 1.- Vortex wake behind wing of high-aspect-ratio supersonic wing and body combination at angle of attack.

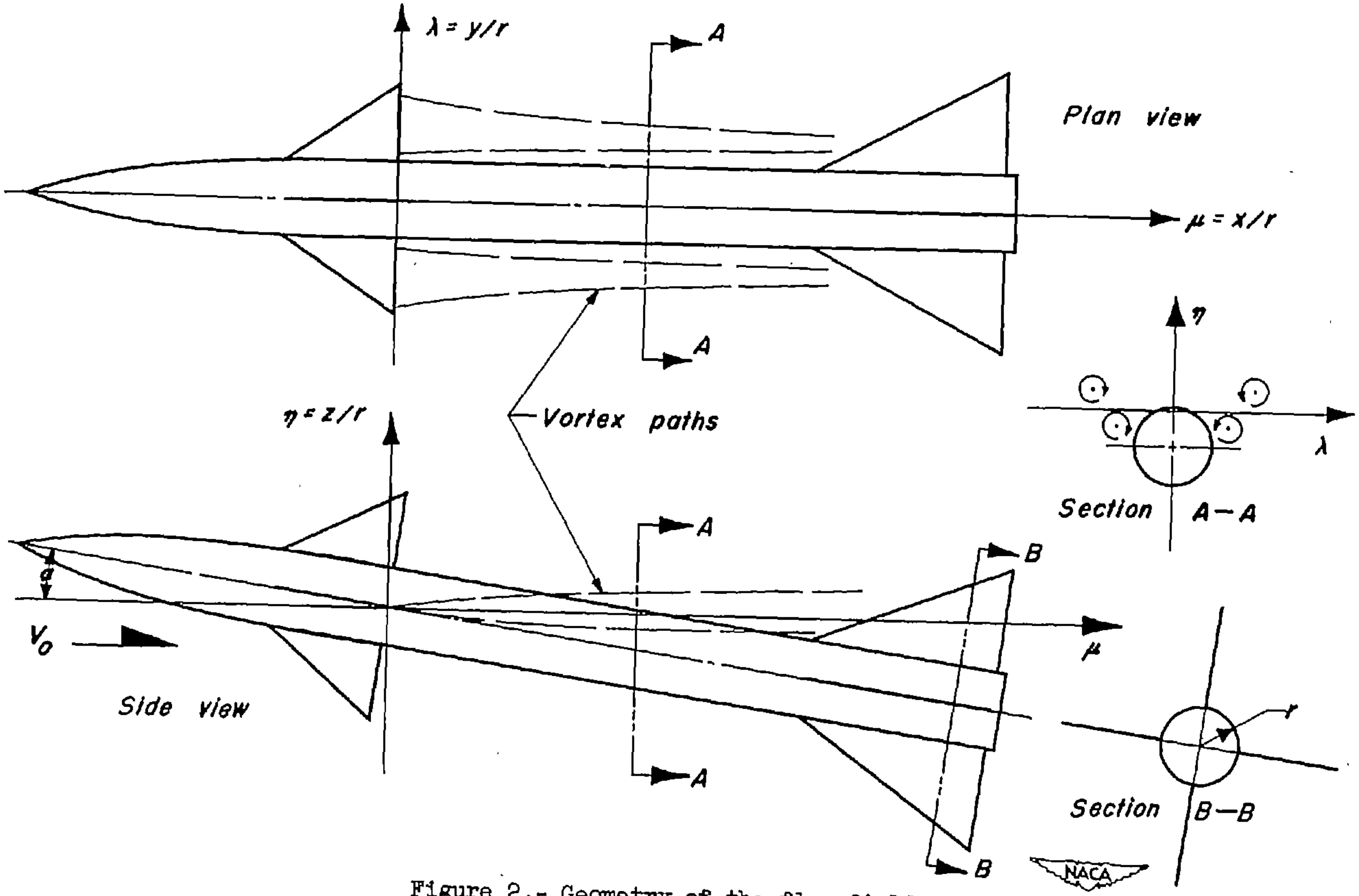

Figure 2.- Geometry of the flow field.

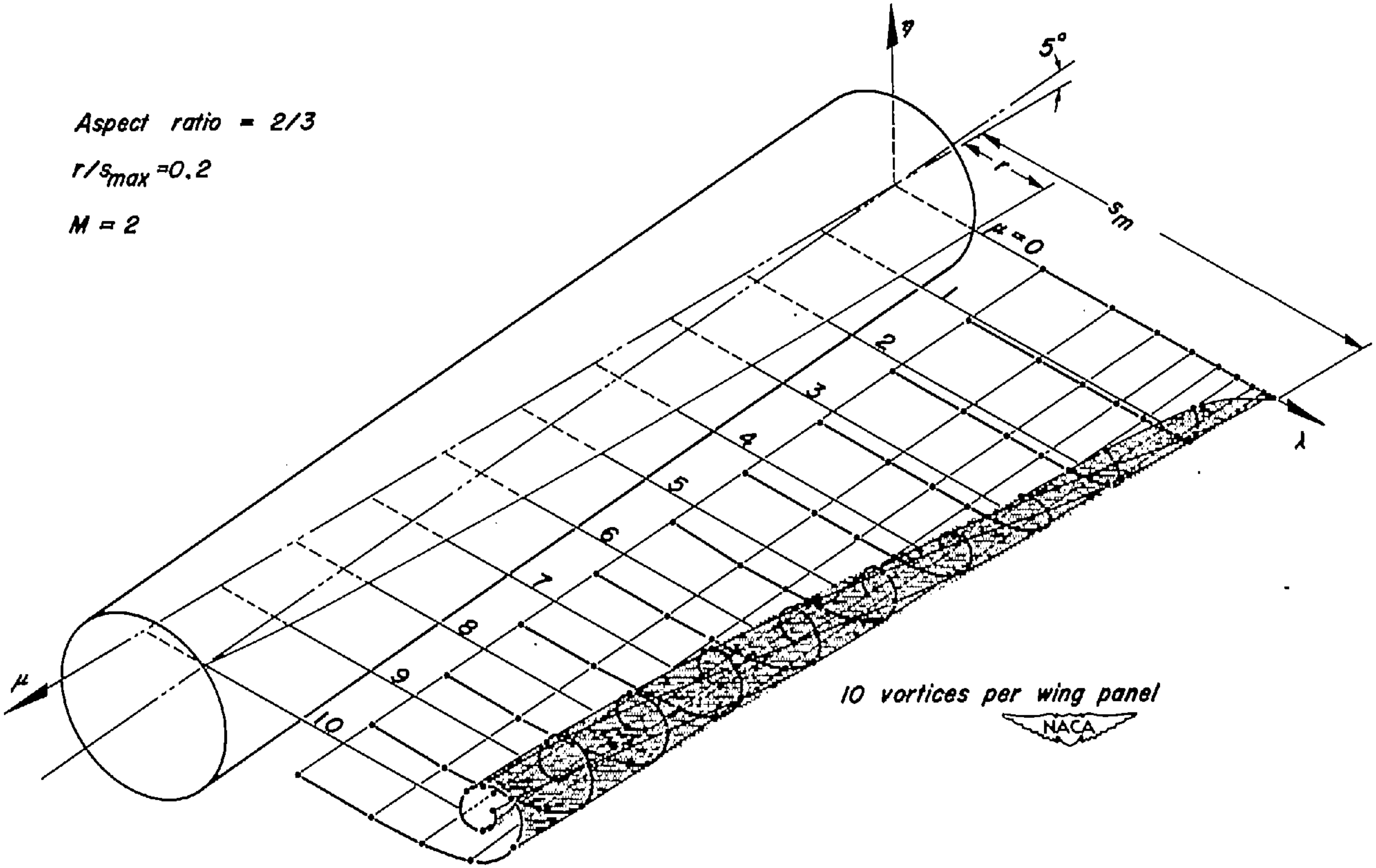

Figure 3.- Rolling up of a vortex sheet behind wing of subsonic leading-edge wing and body configuration.

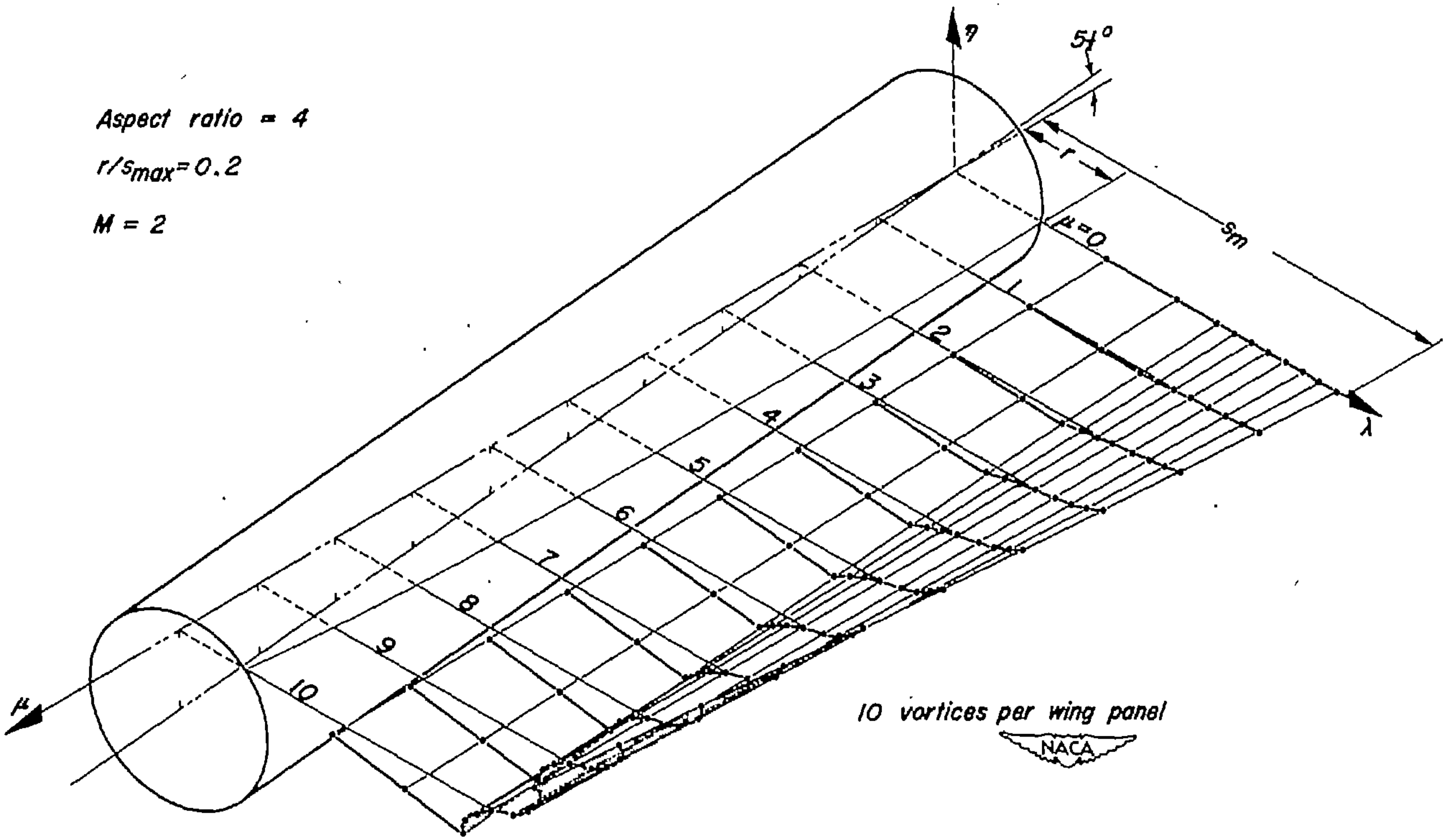

Figure 4.- Rolling up of a vortex sheet behind wing of supersonic leading-edge wing and body configuration.

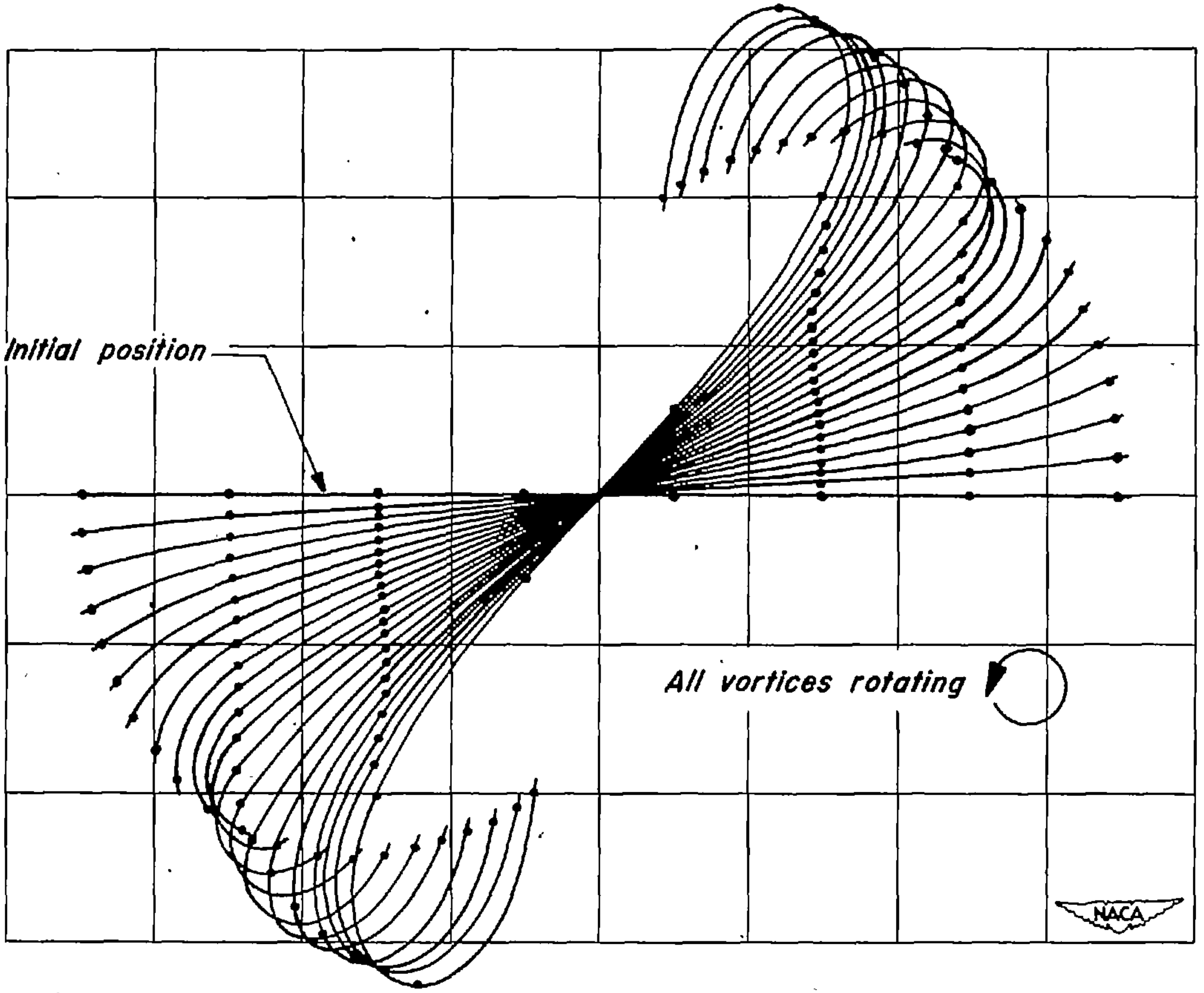

Figure 5.- Rolling up of a vortex sheet segment containing eight equal-strength, equally spaced vortices.

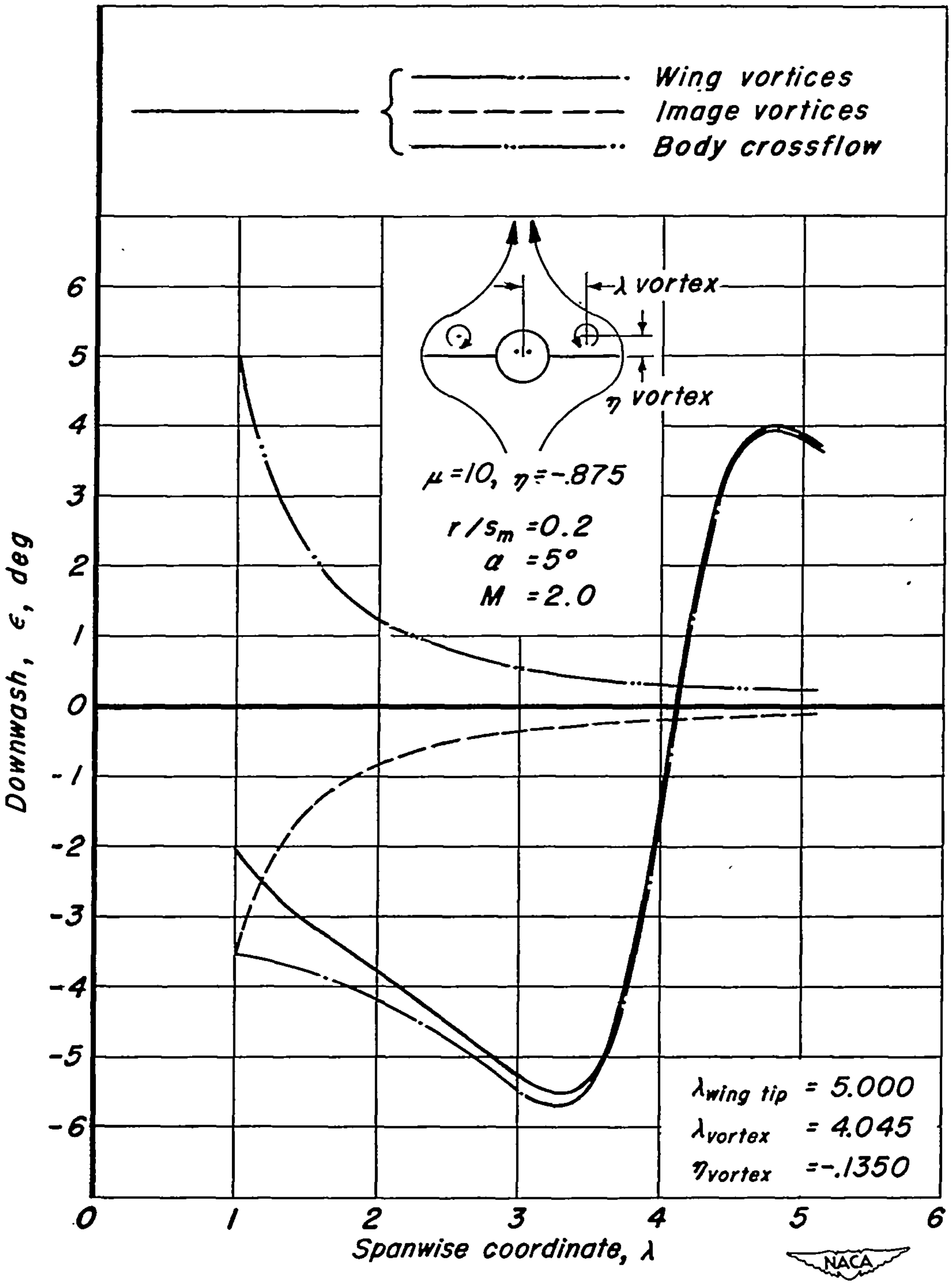

(a) Aspect ratio = 2/3

Figure 6.- Contribution of wing vortices, image vortices, and body crossflow to total downwash at tail location for various aspect ratios.

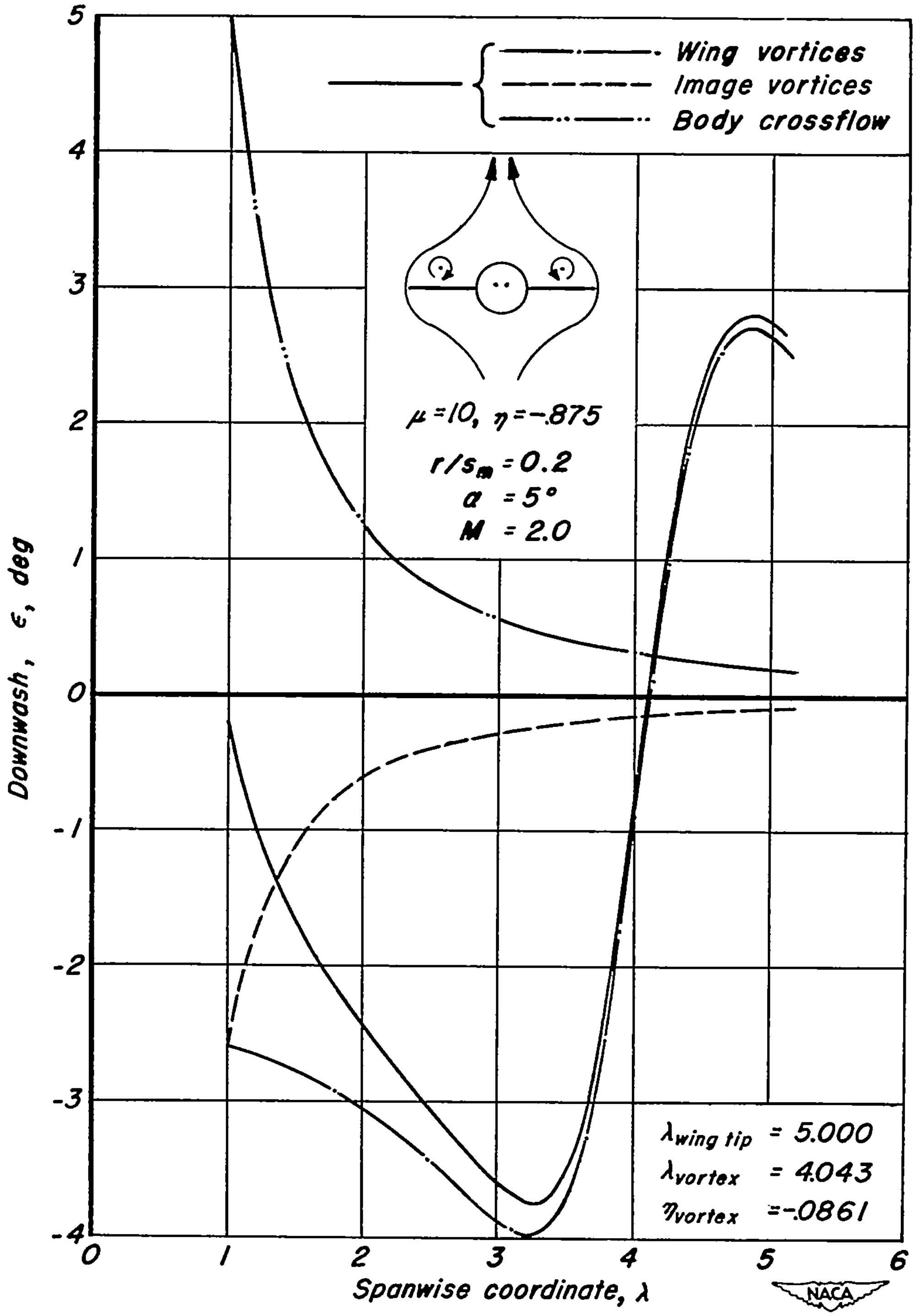

(b) Aspect ratio = 2

Figure 6.- Continued.

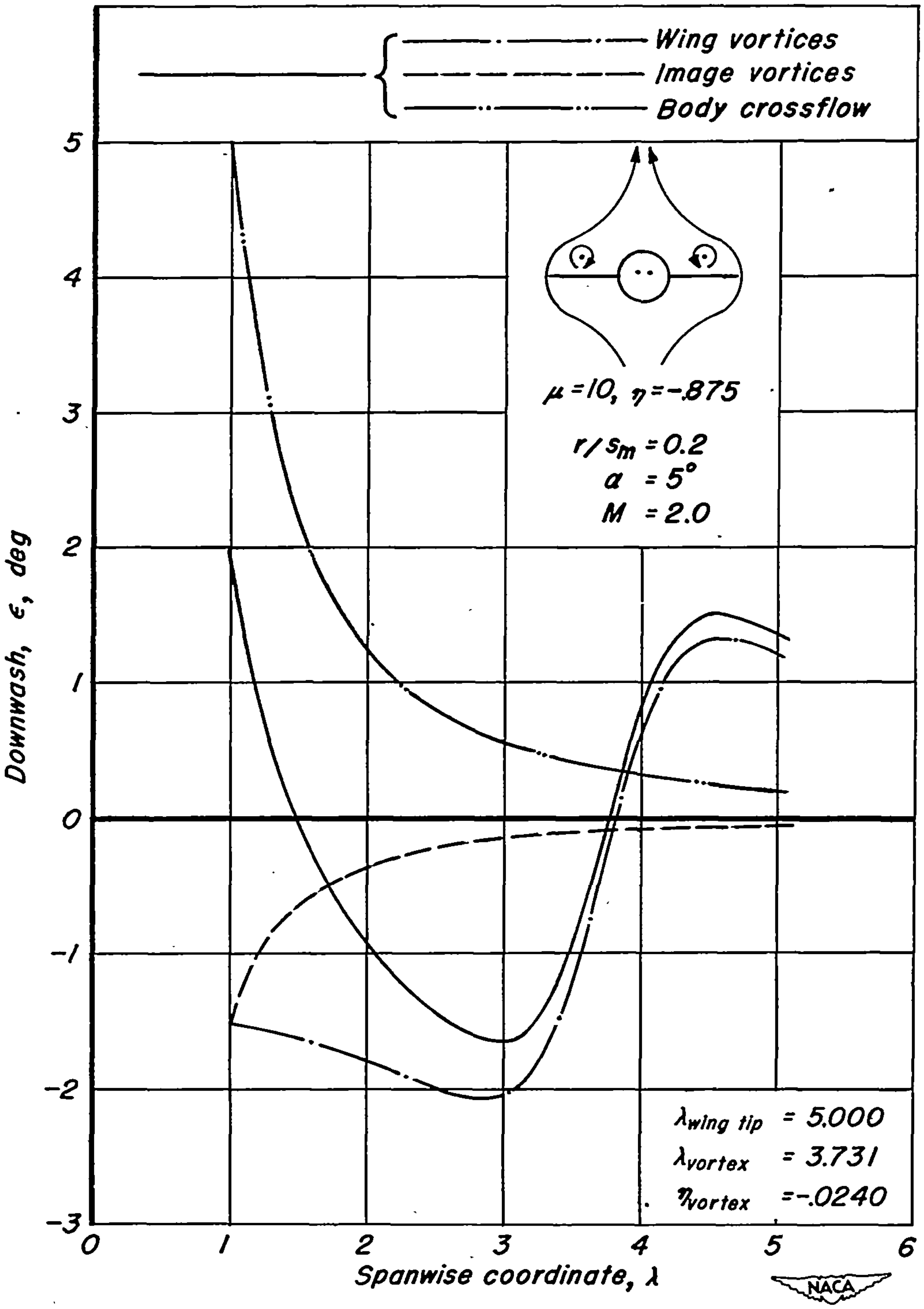

(c) Aspect ratio = 4

Figure 6.- Concluded.

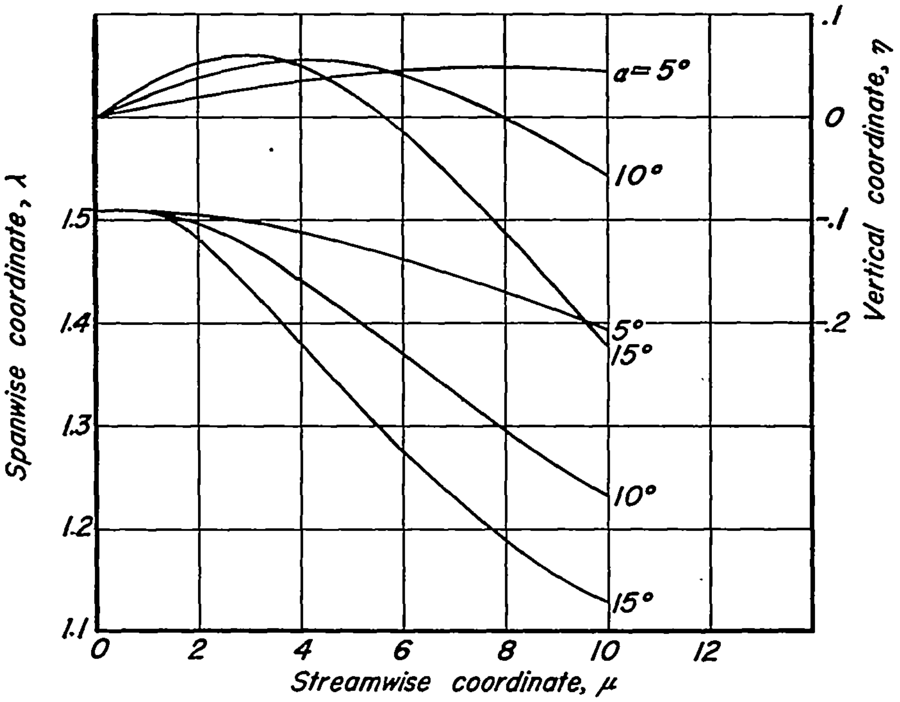

(a) Aspect ratio = 2/3, M = 2, r/s_m = 0.6

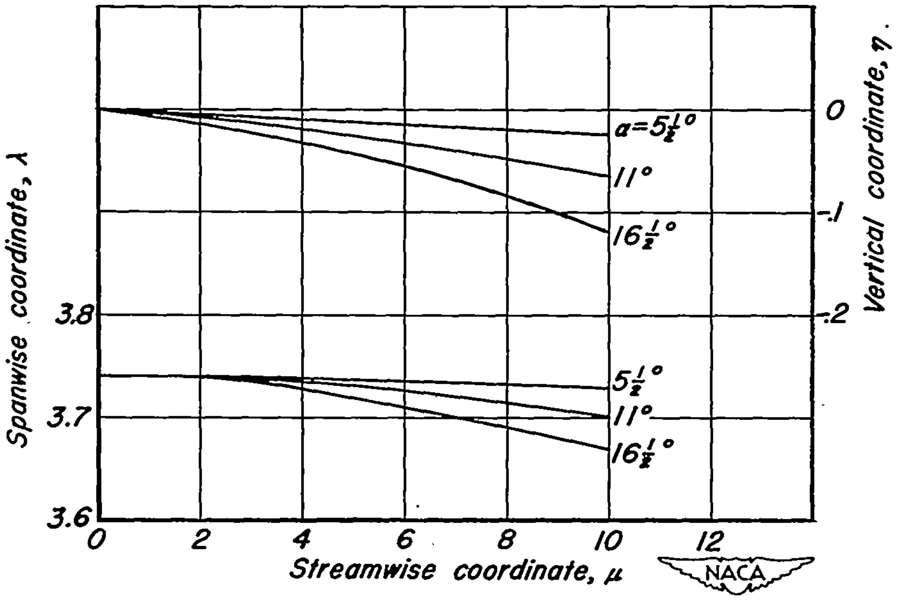

(b) Aspect ratio = 4, M = 2, r/s_m = 0.2

Figure 7.- Vortex paths behind two wing-body combinations at various angles of attack.

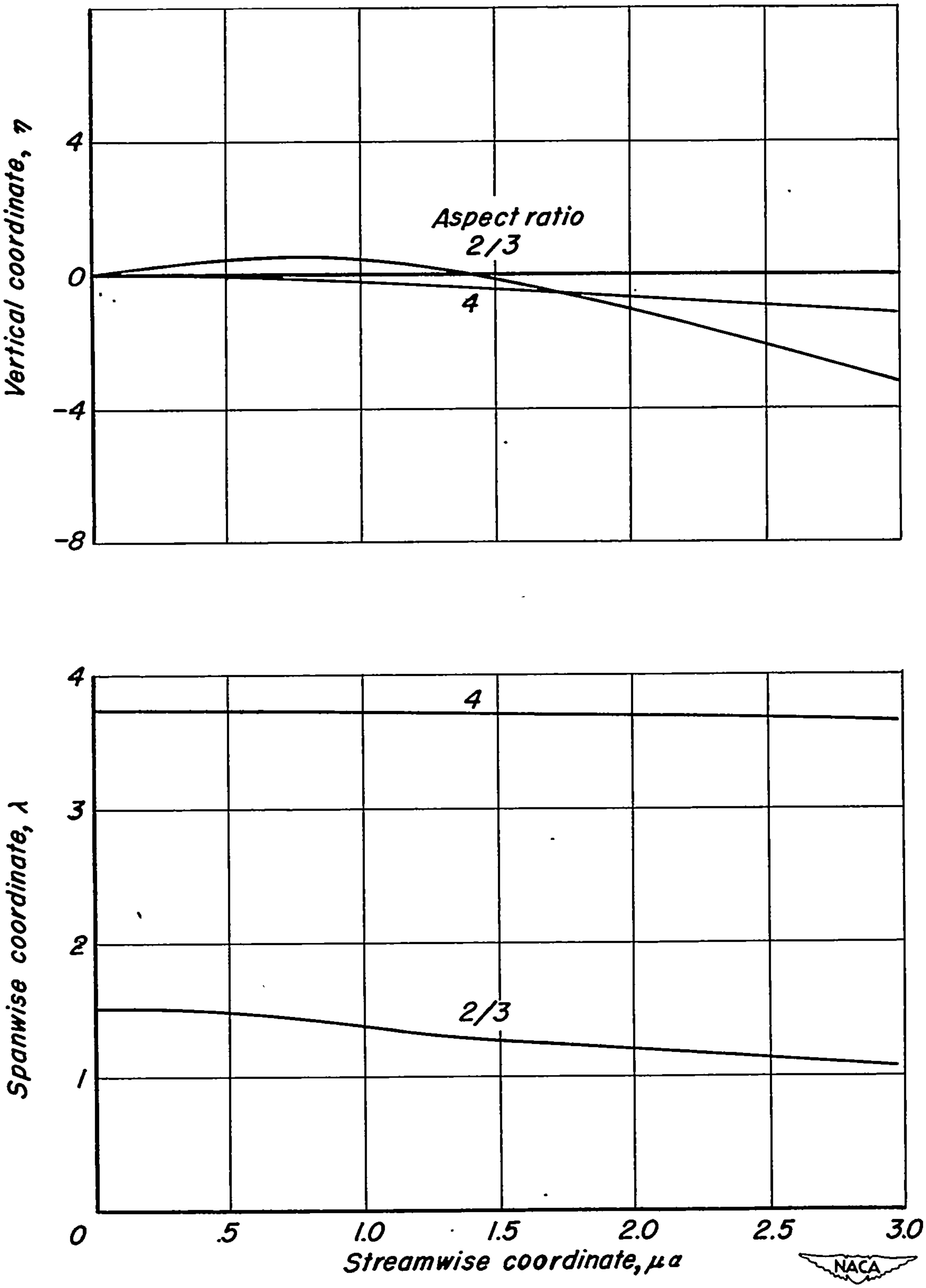

(c) Replot of figures 7(a) and (b) against μα.

Figure 7.- Concluded.

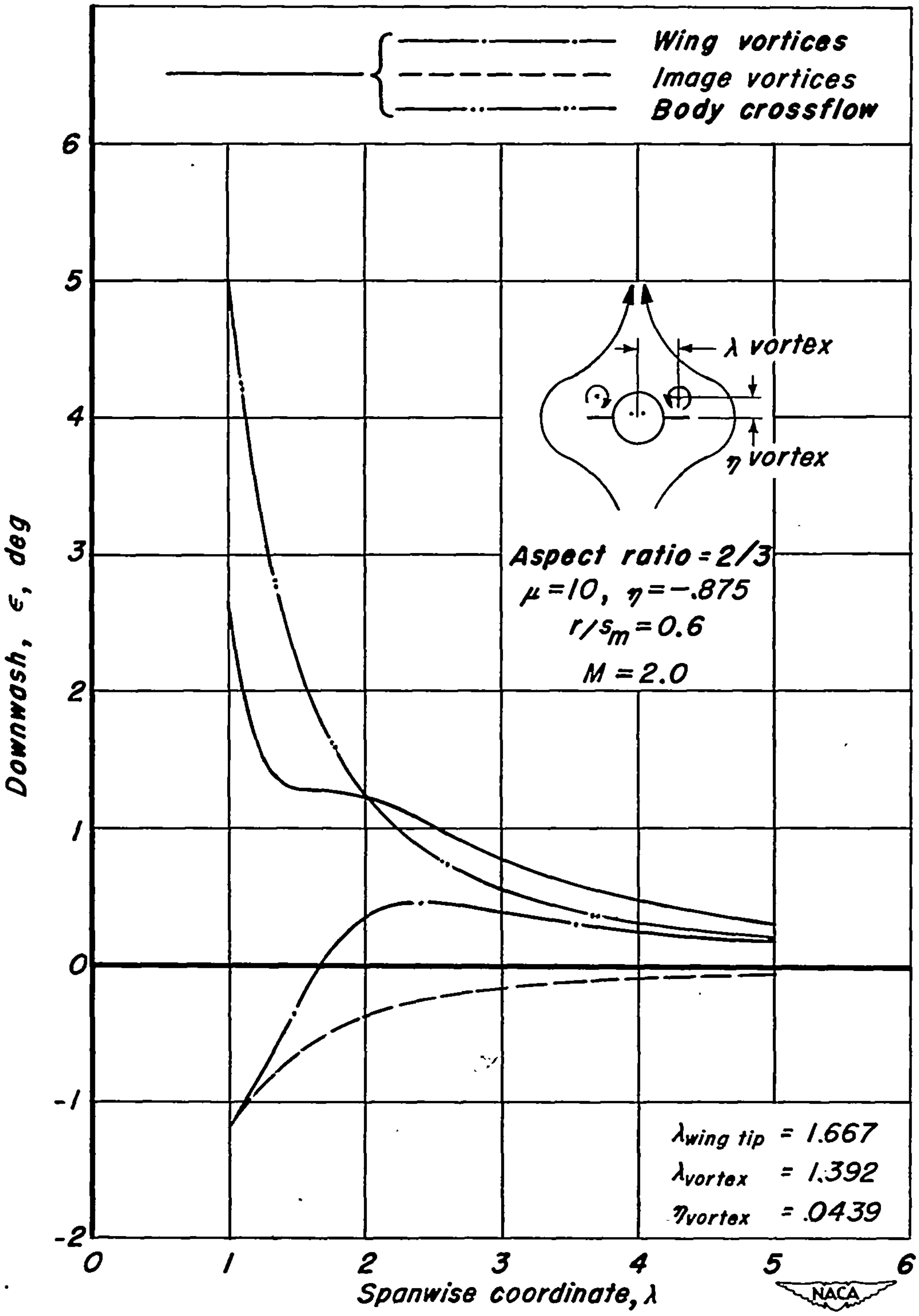

(a) $\alpha = 5^{\circ}$

Figure 8.- Contribution of wing vortices, image vortices, and body crossflow to total downwash at tail location.

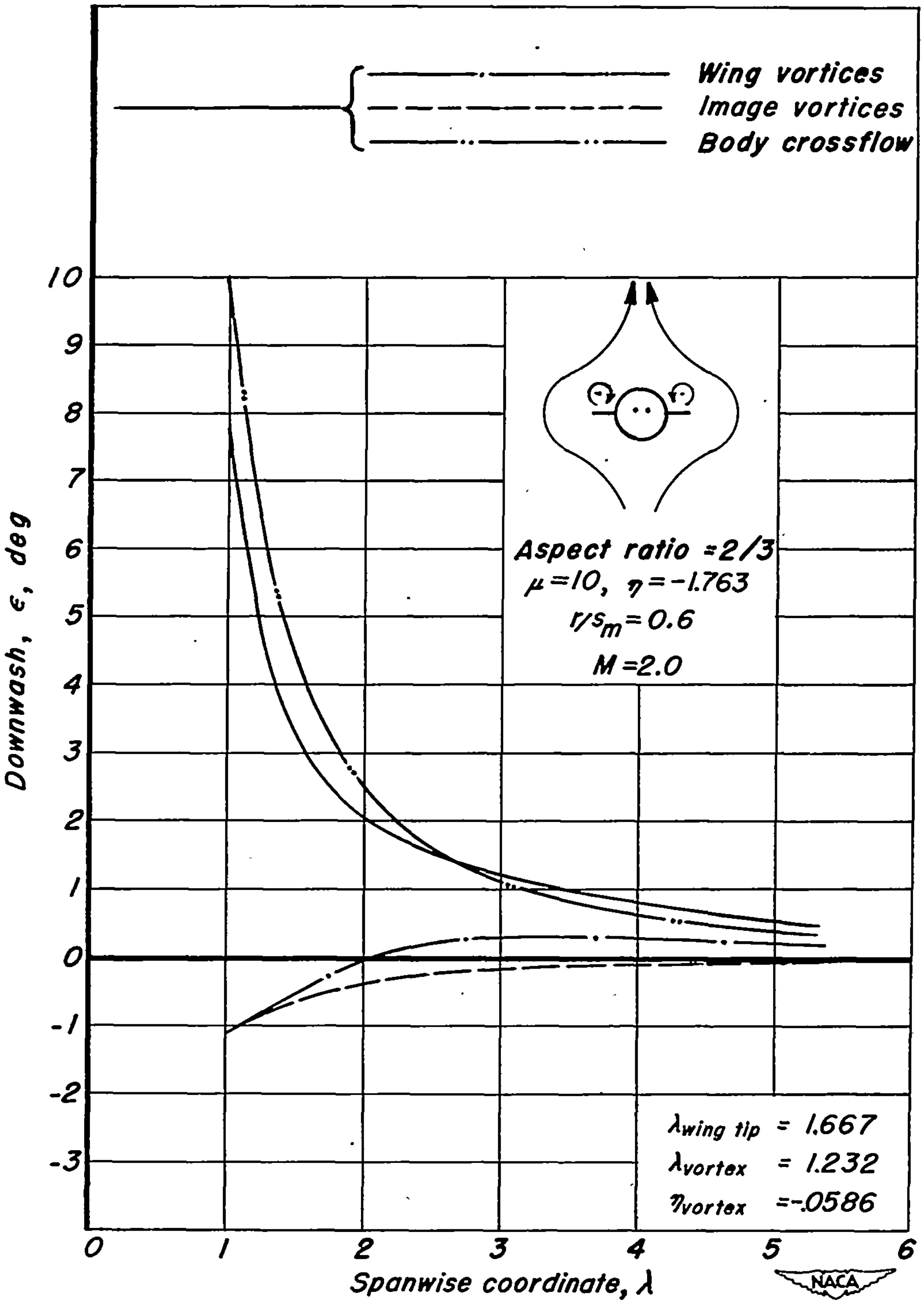

(b) α = 10°

Figure 8.- Continued.

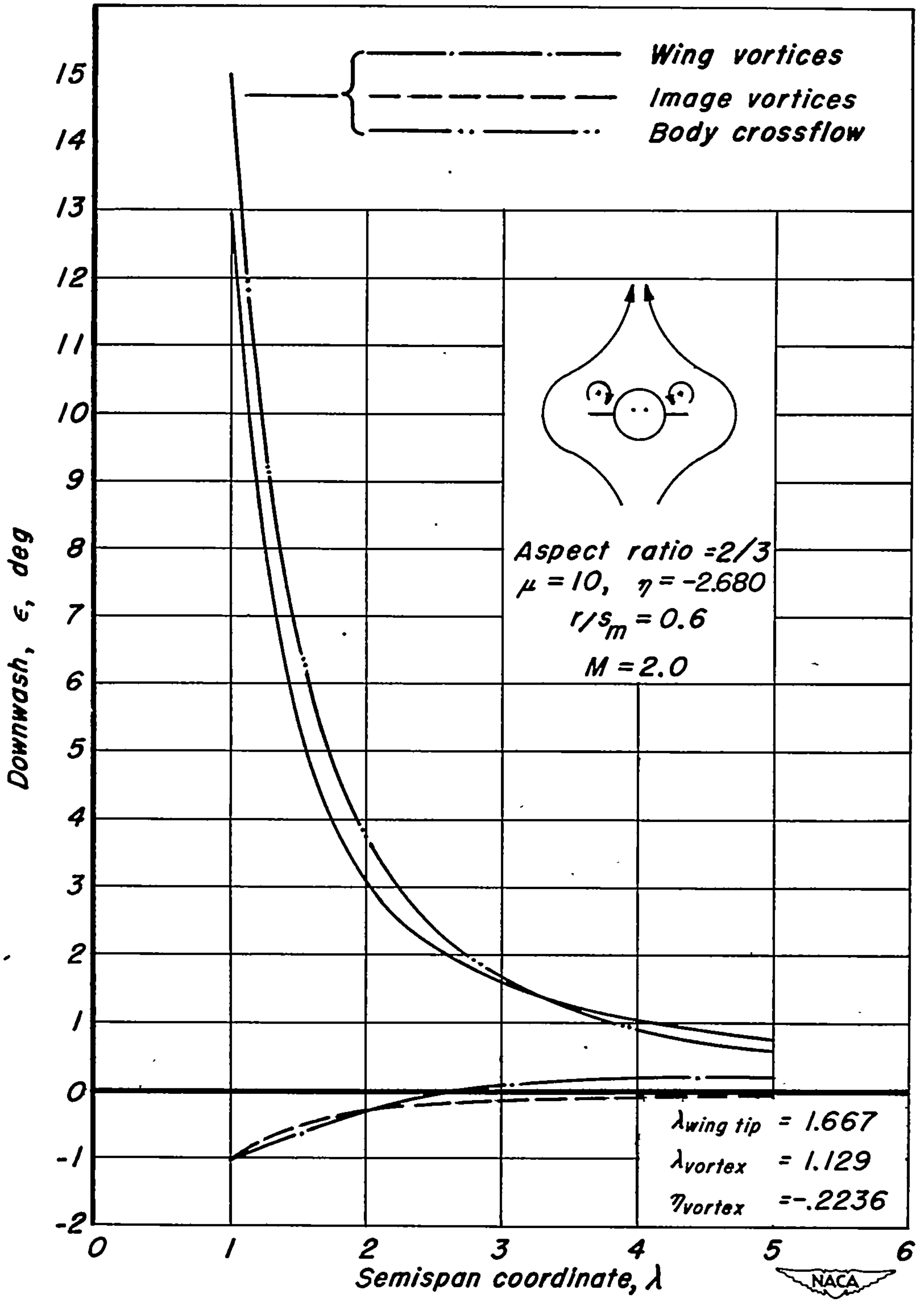

(c) α = 15°

Figure 8.- Continued.

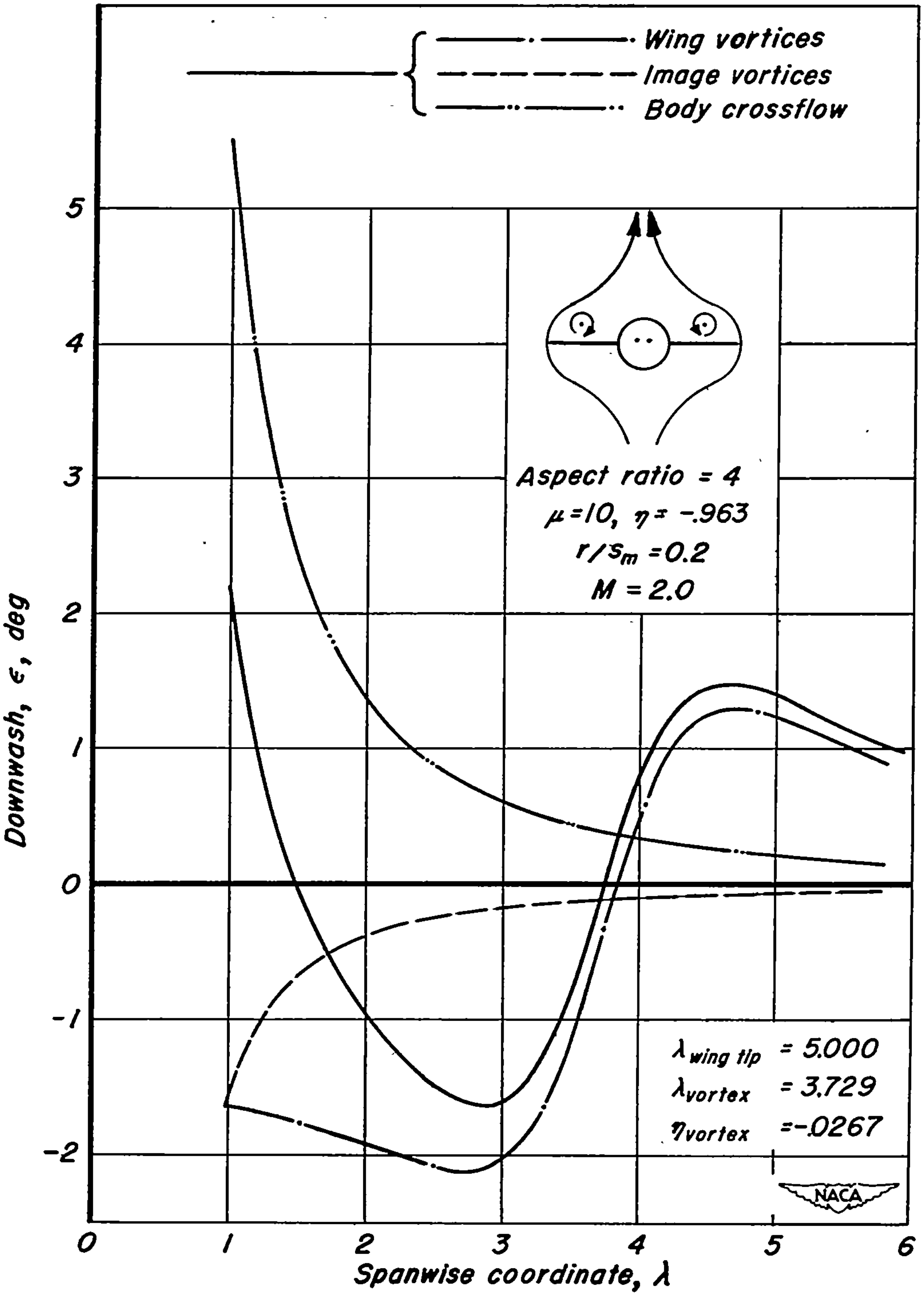

(d) $\alpha = 5\text{-}1/2^{\circ}$

Figure 8.- Continued.

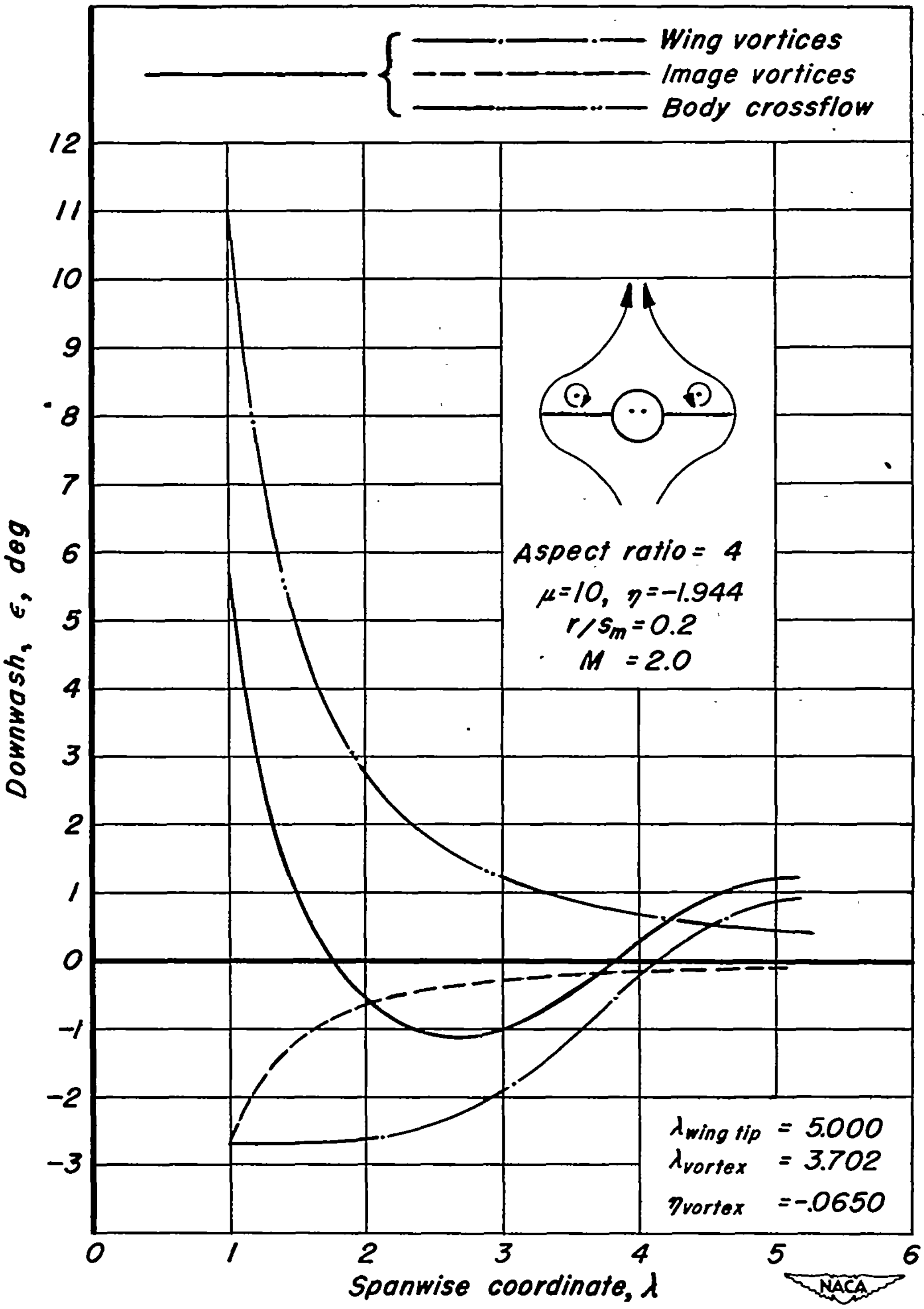

(e) $\alpha = 11^{\circ}$

Figure 8.- Continued.

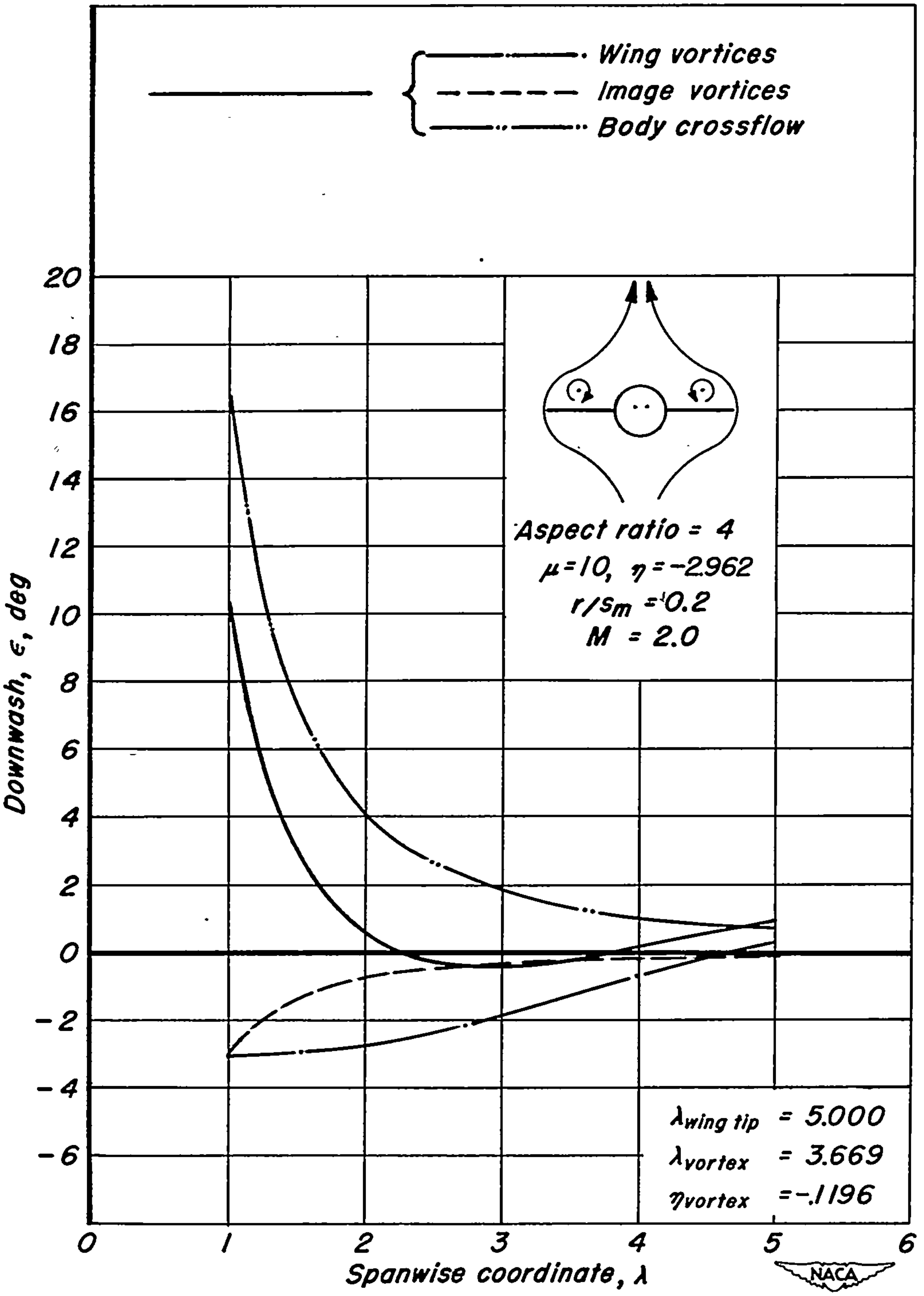

(f) α = 16-1/2°

Figure 8.- Concluded.

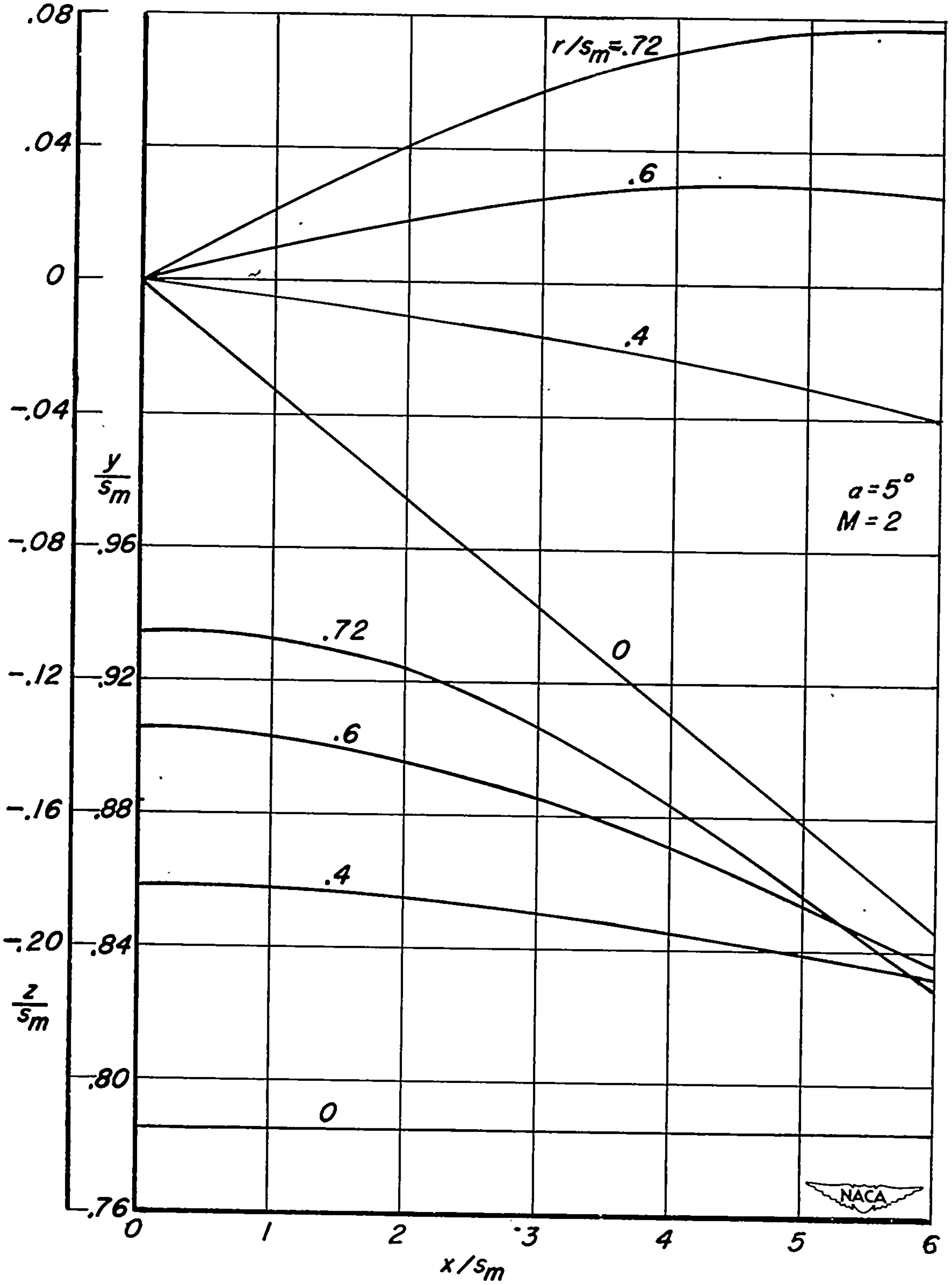

Figure 9.- Vortex paths behind wings of 2/3-aspect-ratio triangular-wing and body combinations with various ratios of body radius to wing semispan r/s_m.

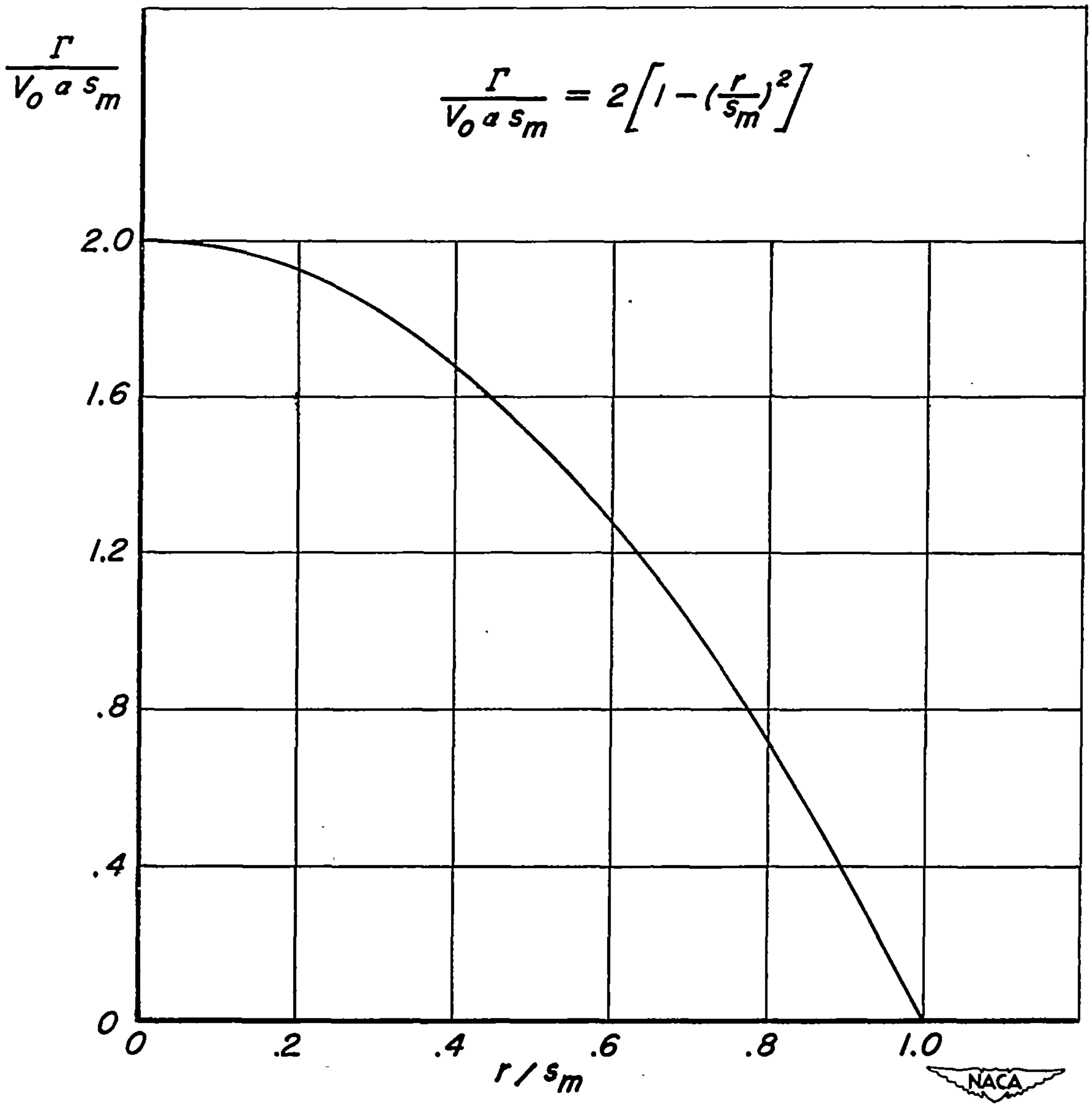

Figure 10.- Variation of single-vortex strength with body radius to wing semispan ratio for subsonic leading-edge configuration.

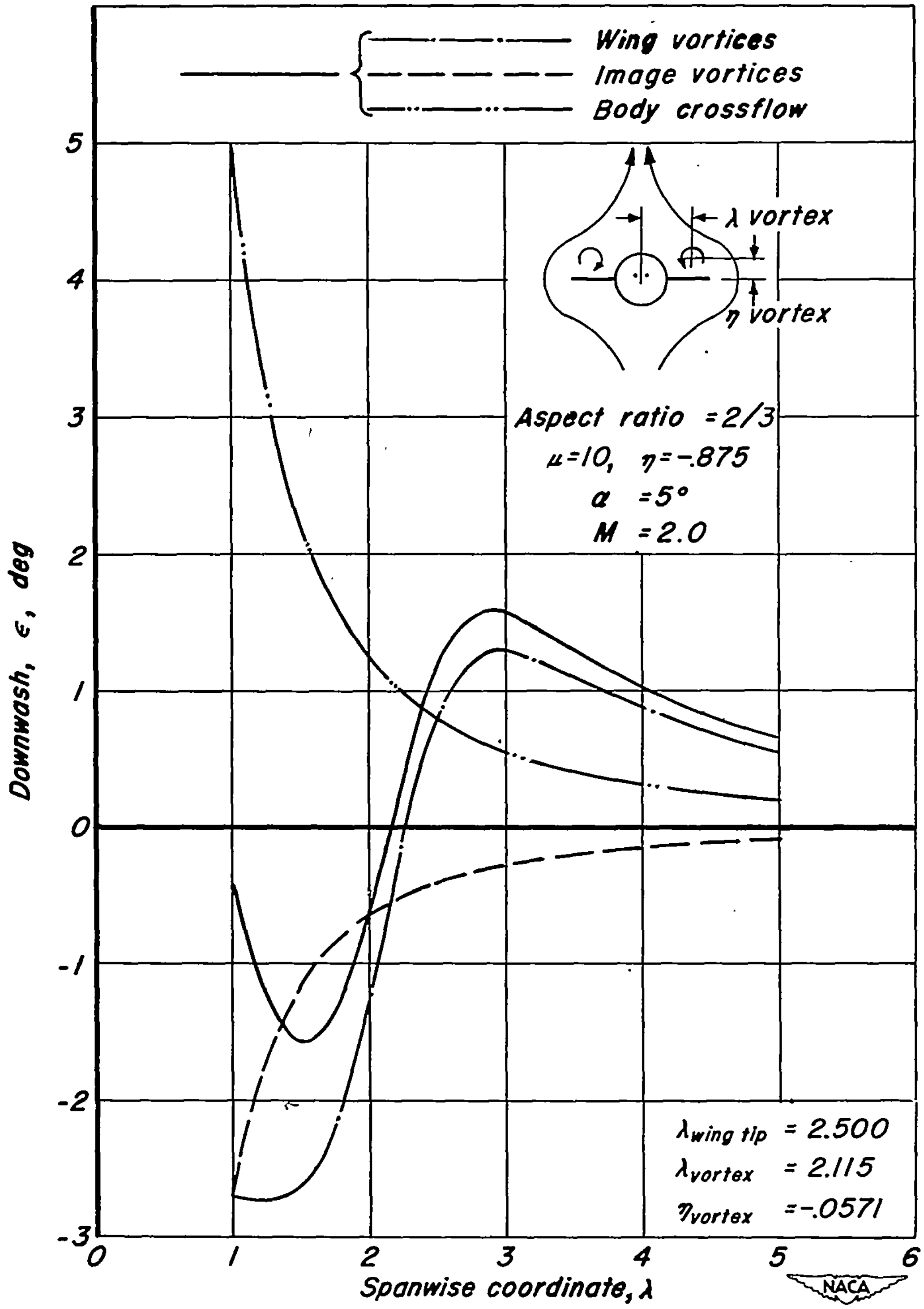

(a) $r/s_m = 0.4$

Figure 11.- Contribution of wing vortices, image vortices, and body crossflow to total downwash at tail location.

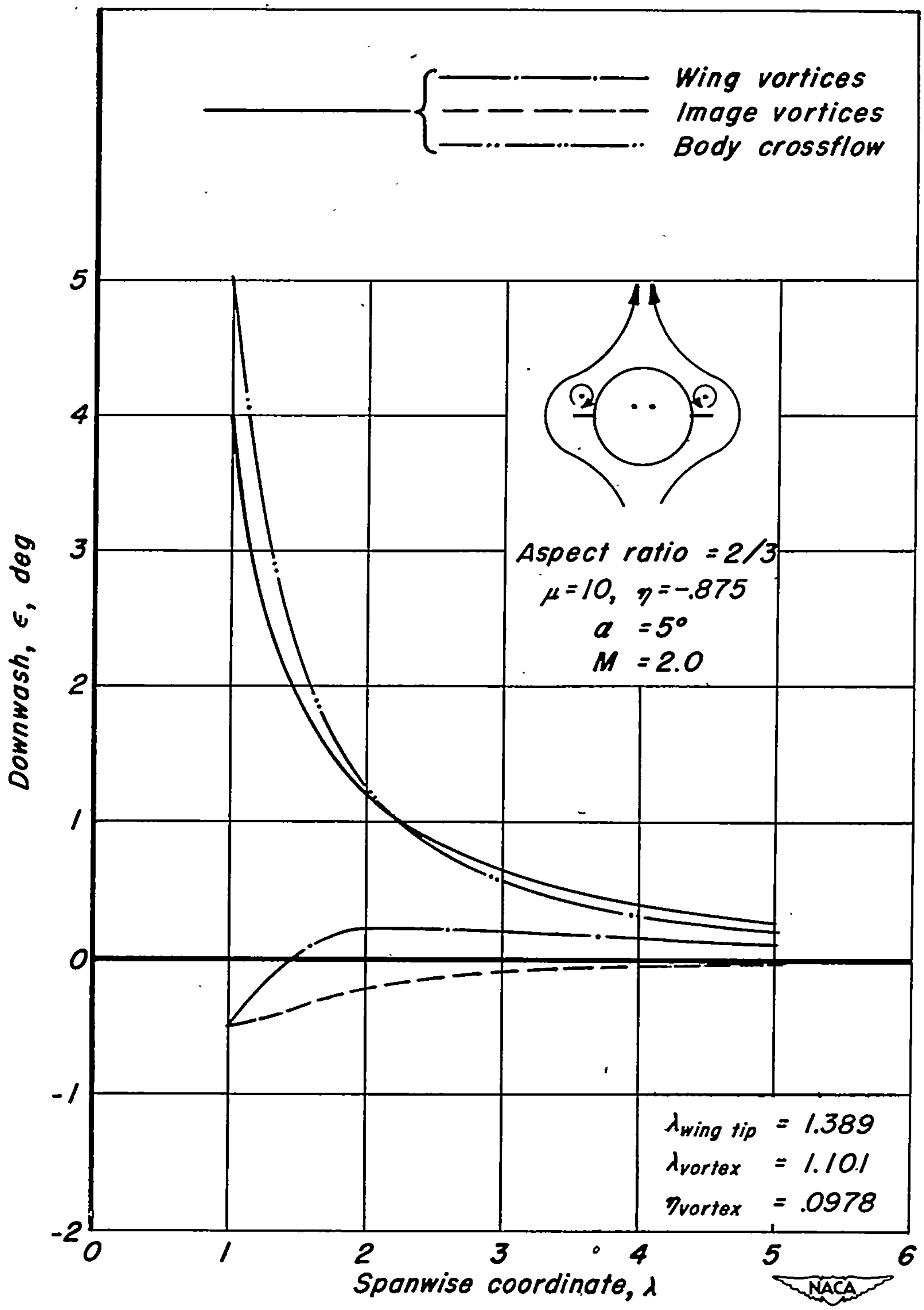

(b) $r/s_m = 0.72$

Figure 11.- Concluded.

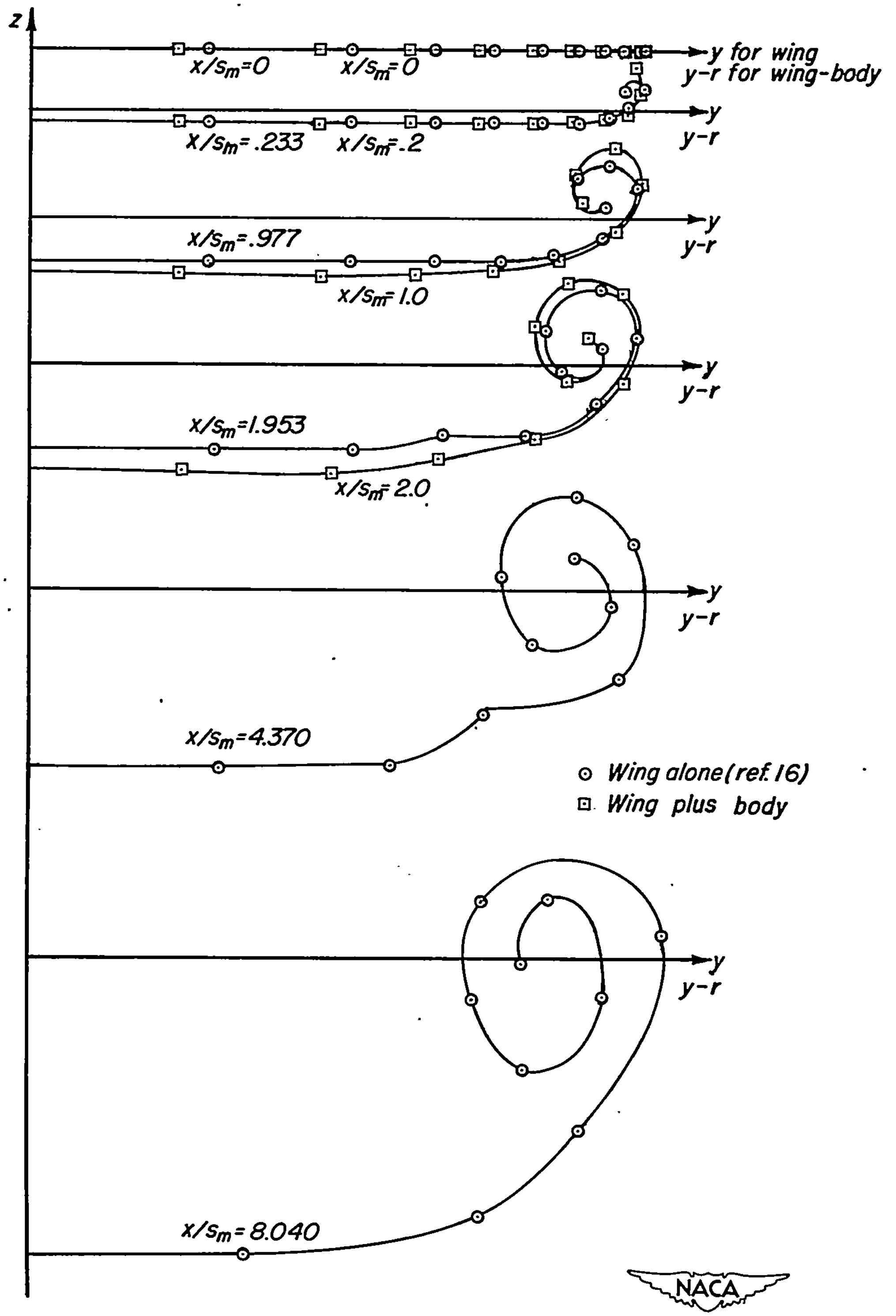

Figure 12.- Comparison of rolling up of vortex sheet behind wing-body combination ($A = 2/3$, $r/s_m = 0.2$) with wing alone.

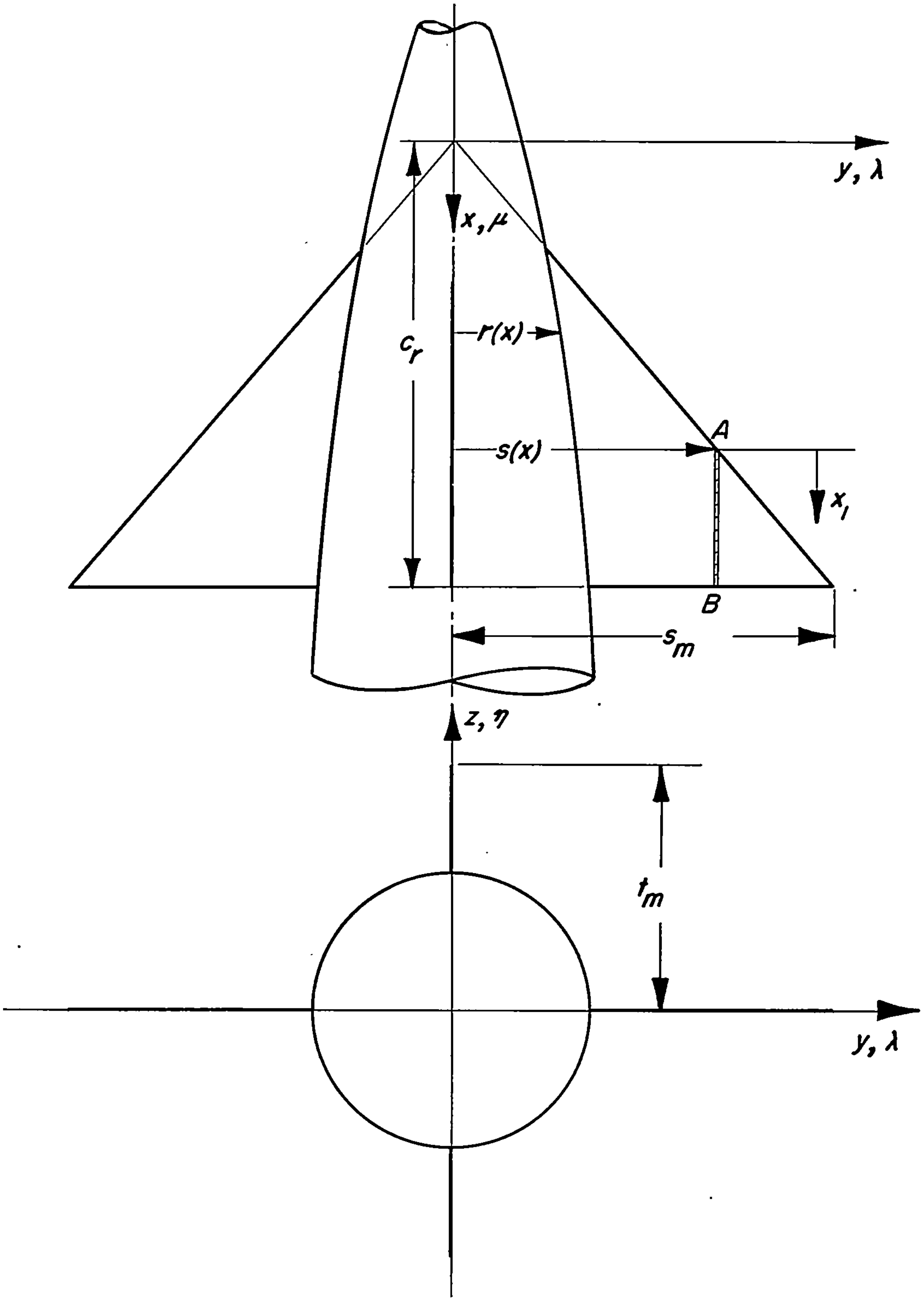

Figure 13.- Illustration of coordinates and dimensions of general wing-body configuration.

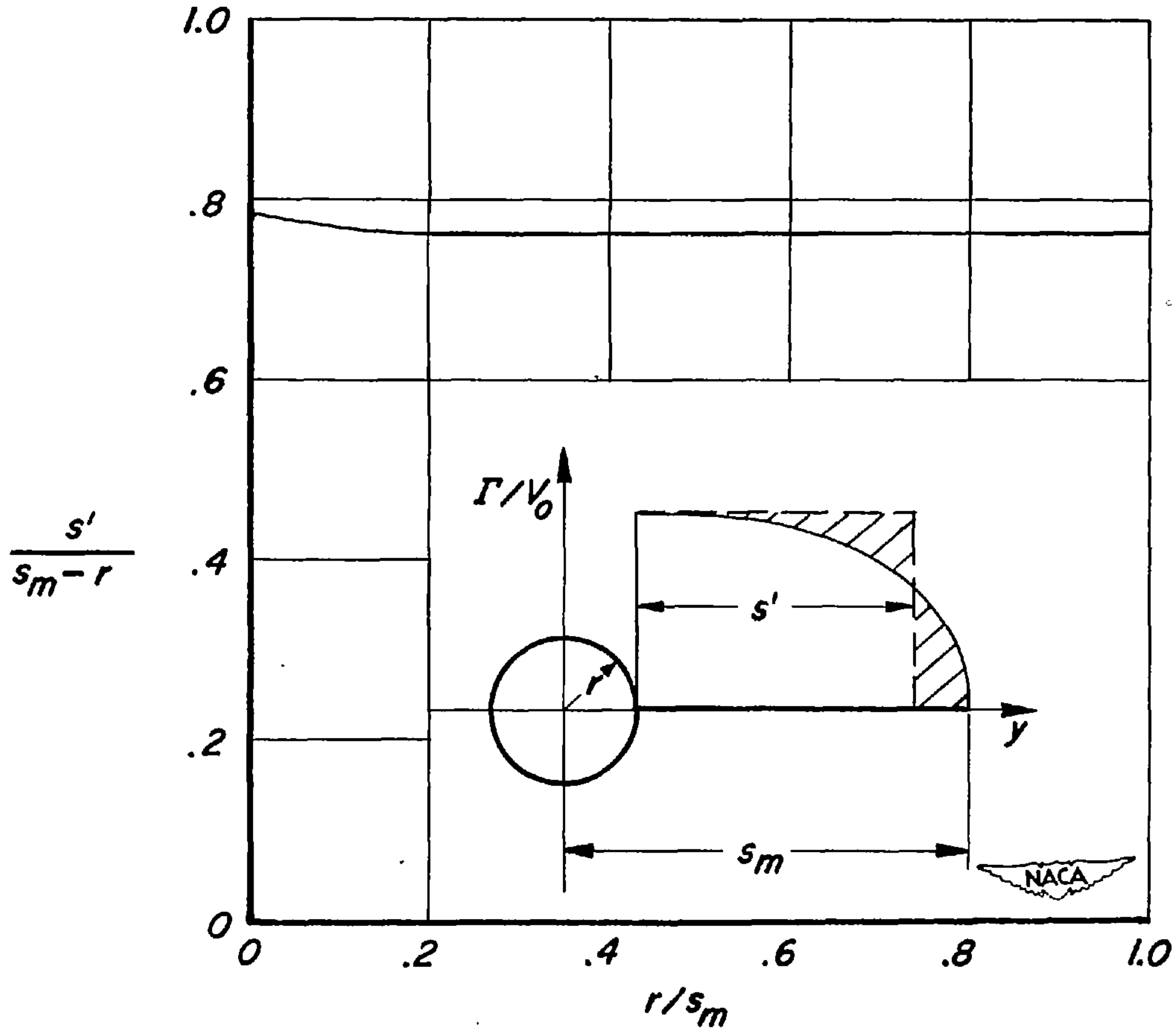

Figure 14.- Spanwise position of single vortex approximating circulation distribution.

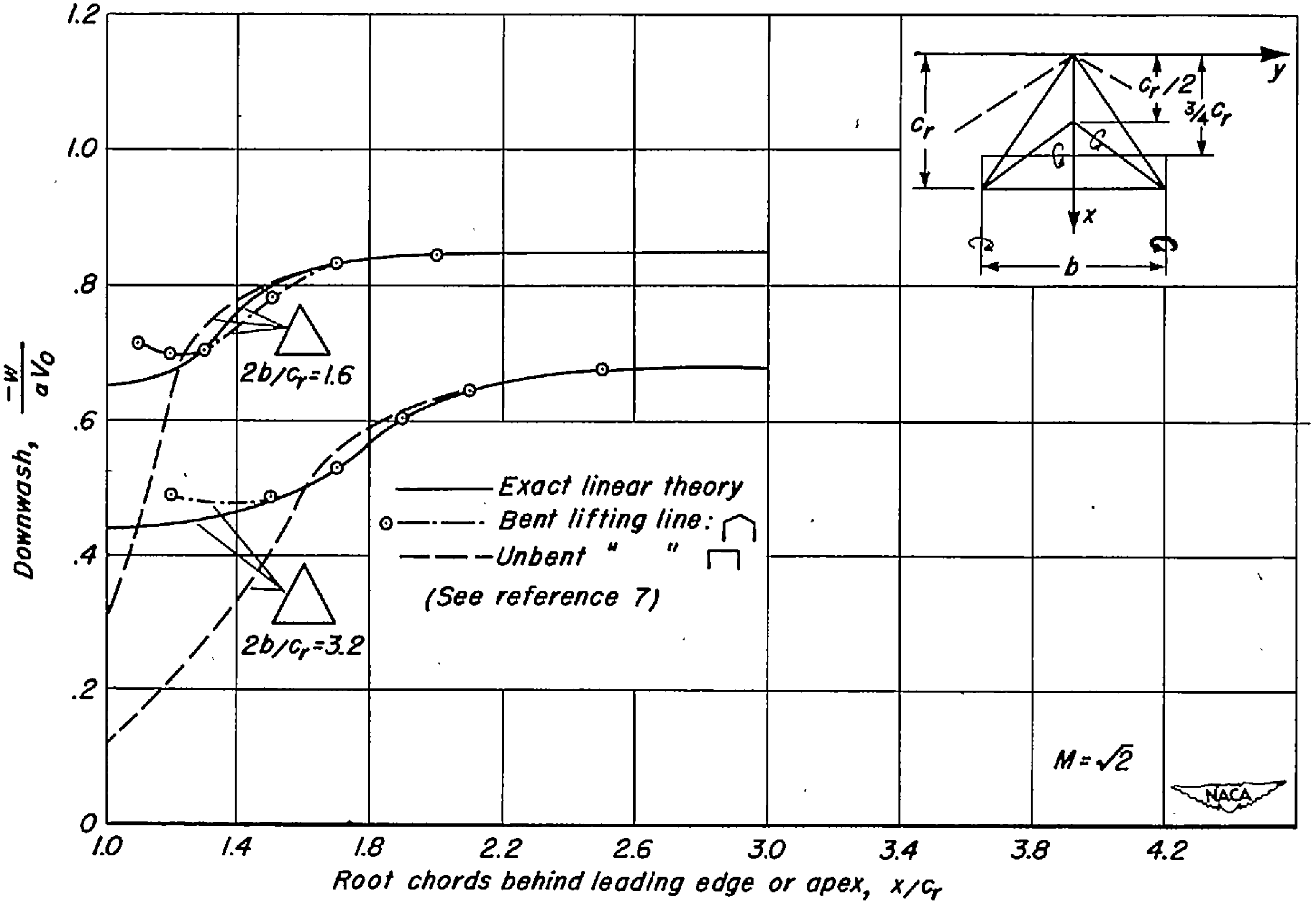

Figure 15.- Downwash along line y = z = 0 behind triangular wings, from reference 7.

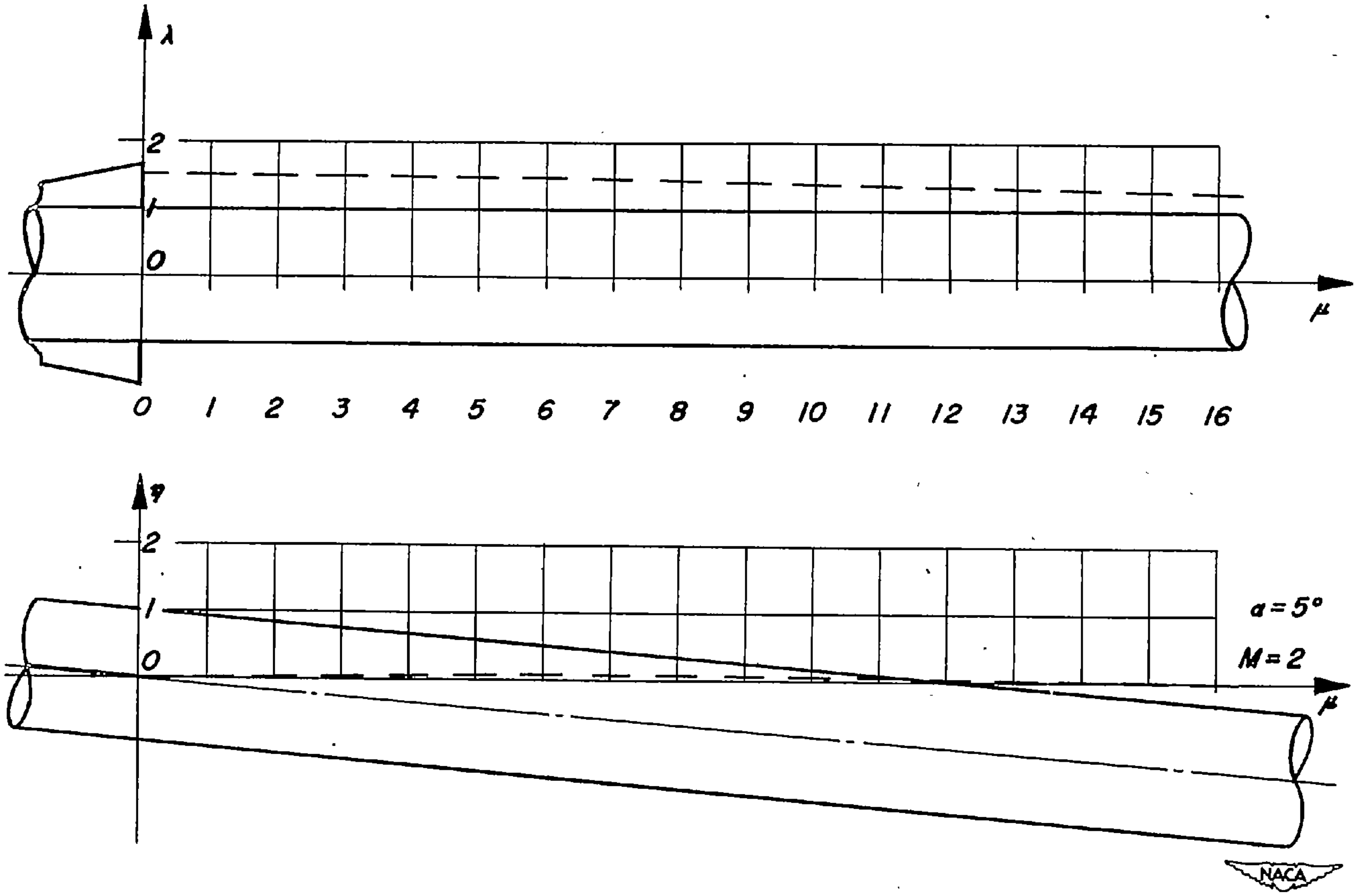

Figure 16.- Calculated vortex path behind plane wing and body combination of example 1.

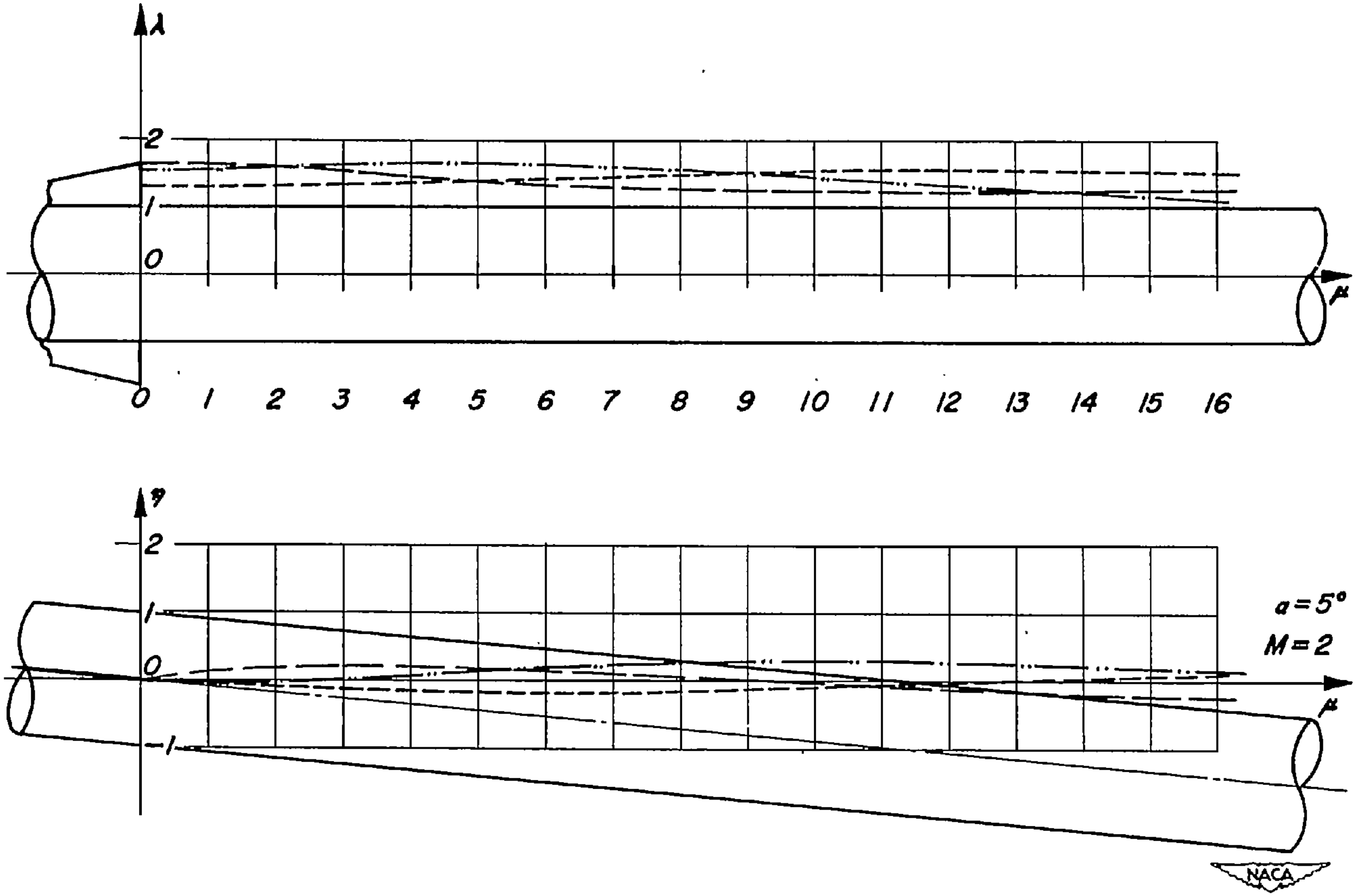

Figure 17.- Calculated vortex paths behind plane wing and body combination of example 1.

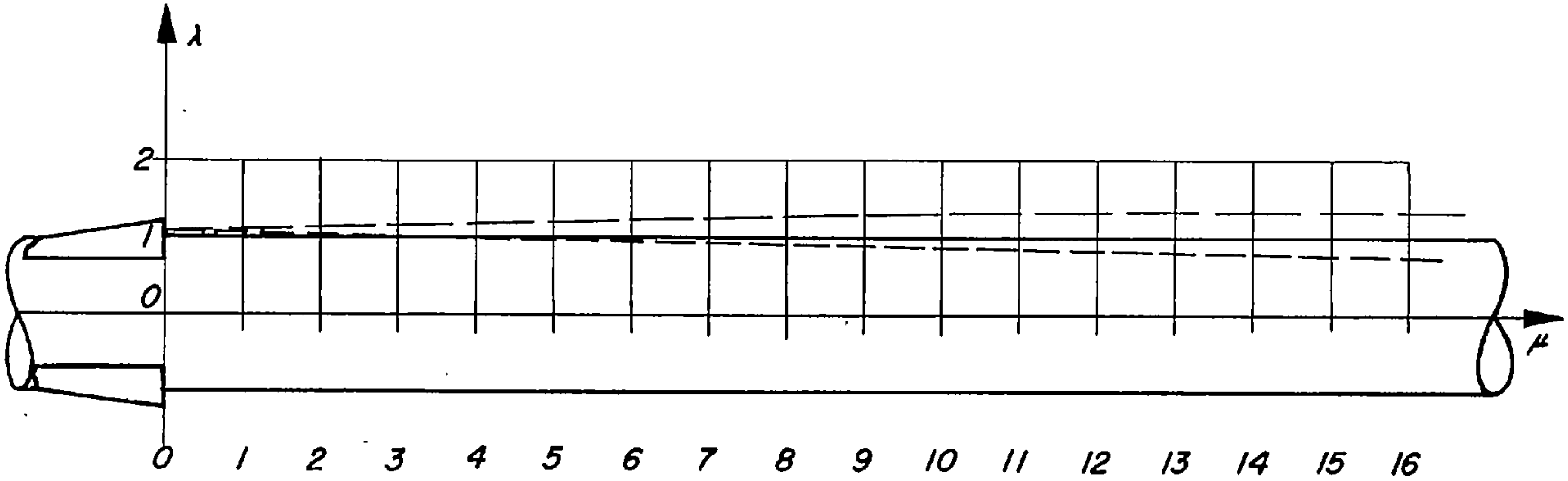

Plan view

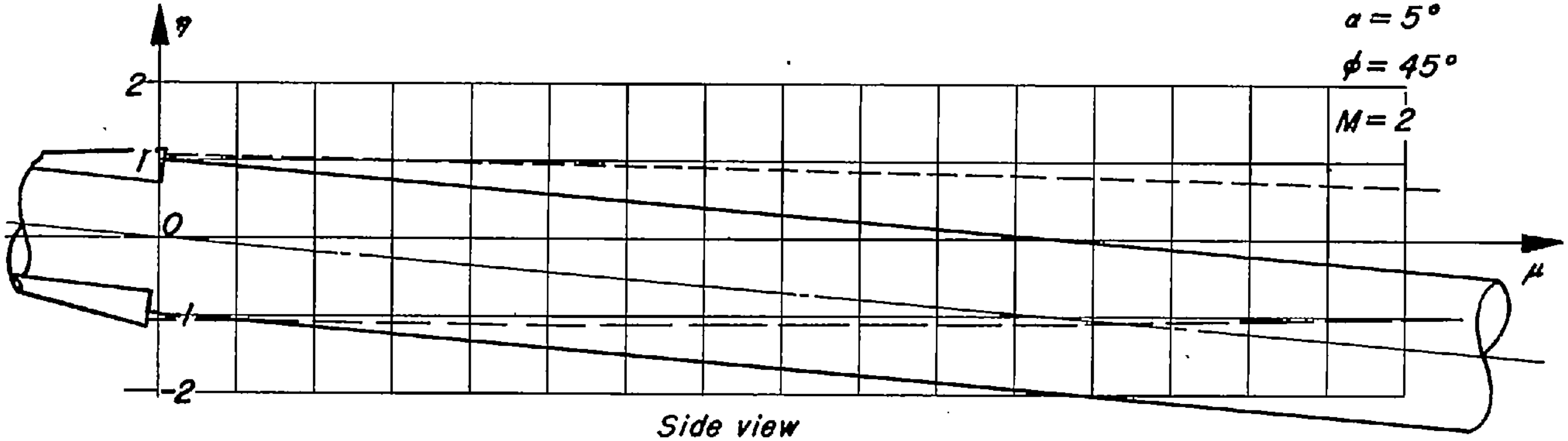

Side view

Figure 18.- Calculated vortex paths behind cruciform wing and body combination of example 2.

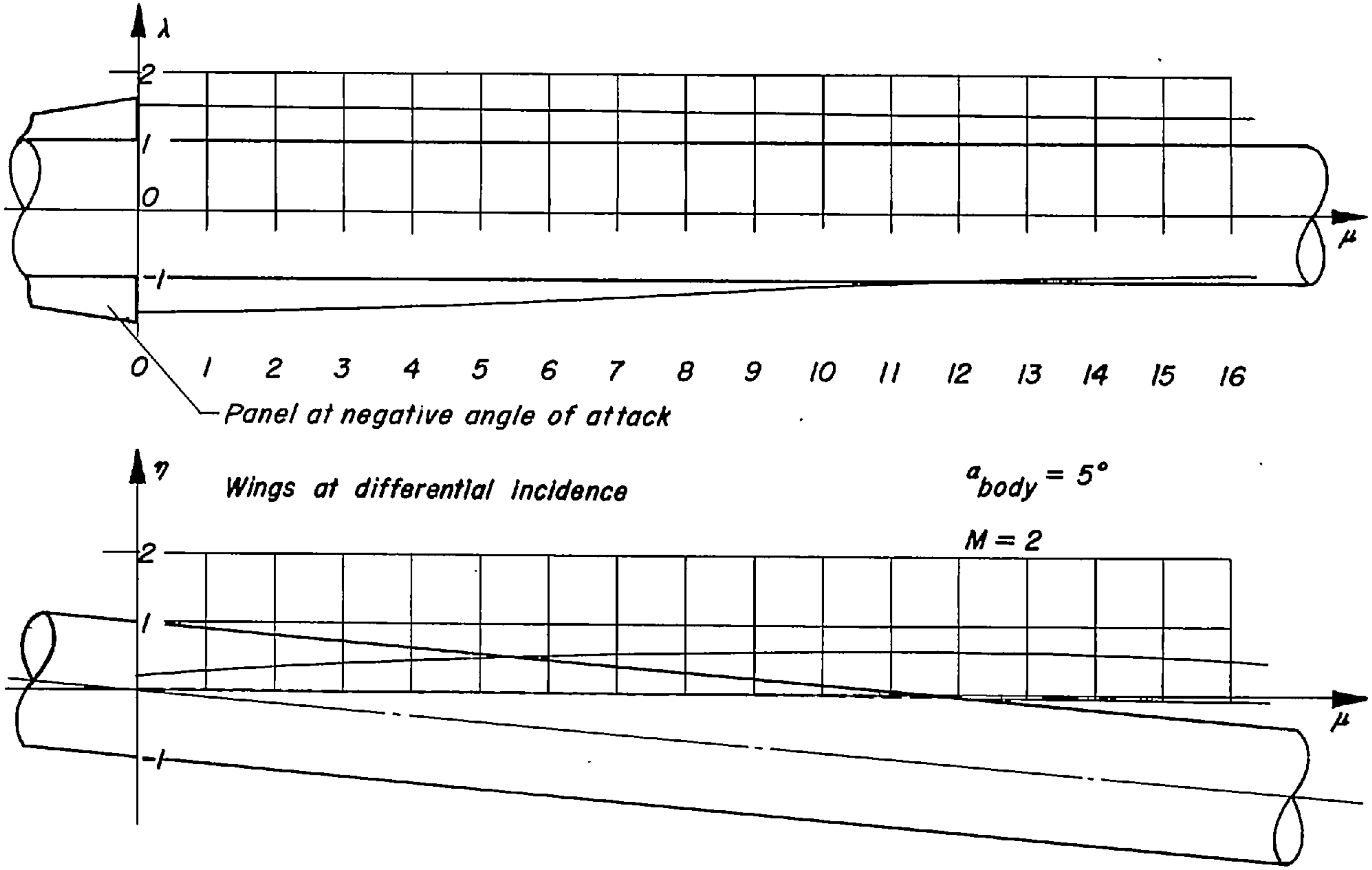

Figure 19.- Calculated vortex path behind plane wing and body combination of example 3.

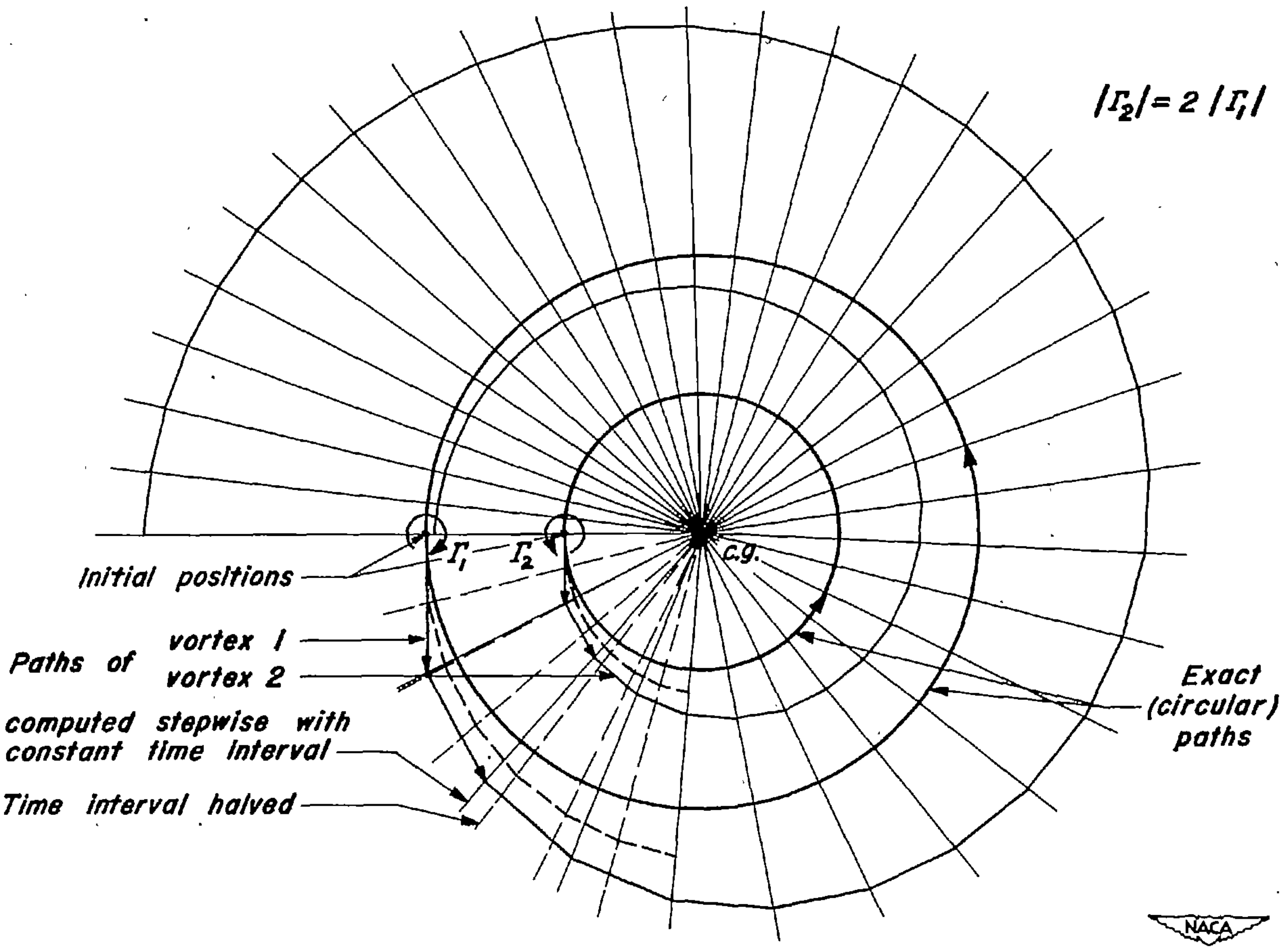

Figure 20.- Approximated (spiral) and exact (circular) paths of two vortices of unequal strength.

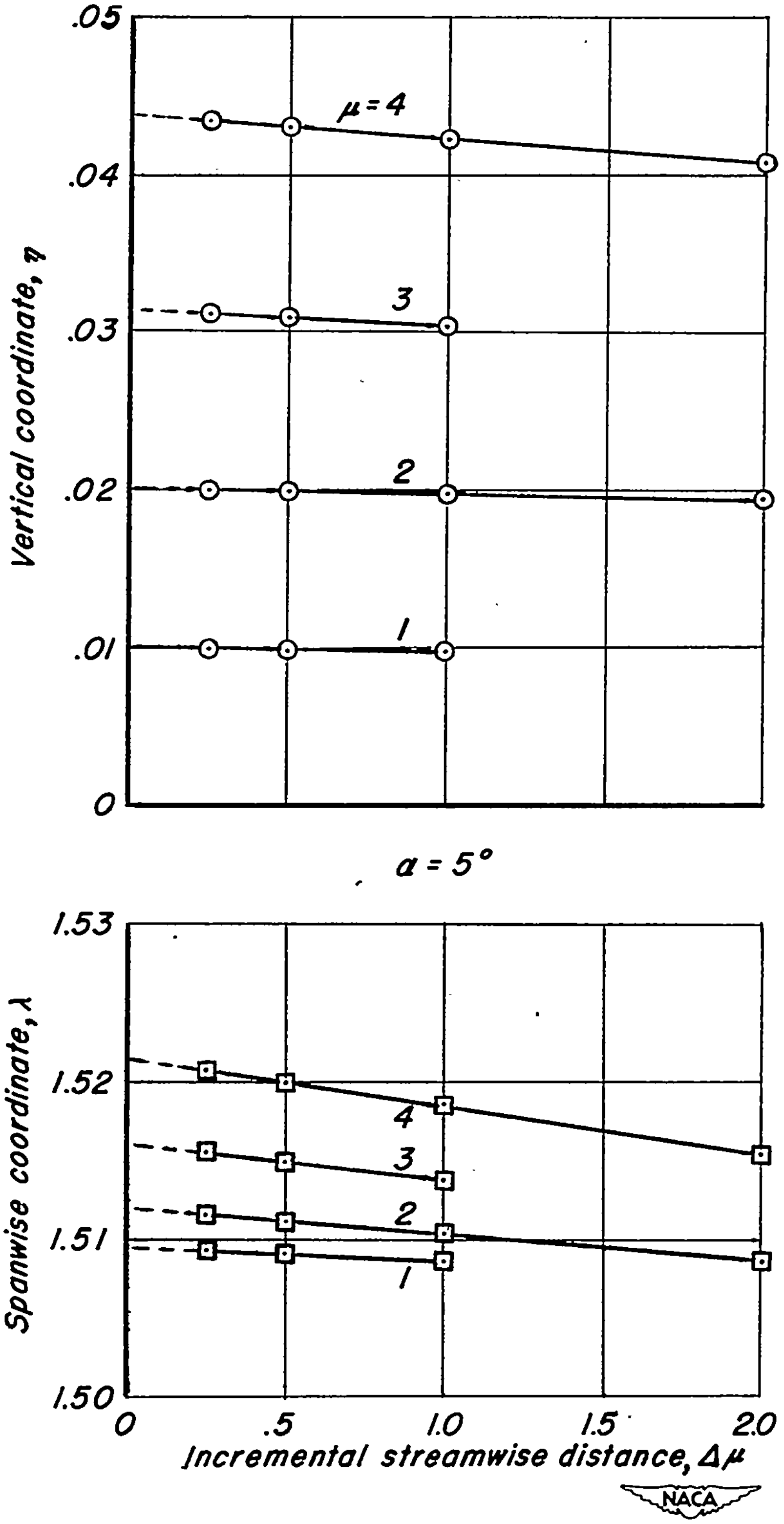

Figure 21.- Vortex position error versus $\Delta\mu$ at stations $\mu = 1, 2, 3,$ and 4 for single wing vortex.

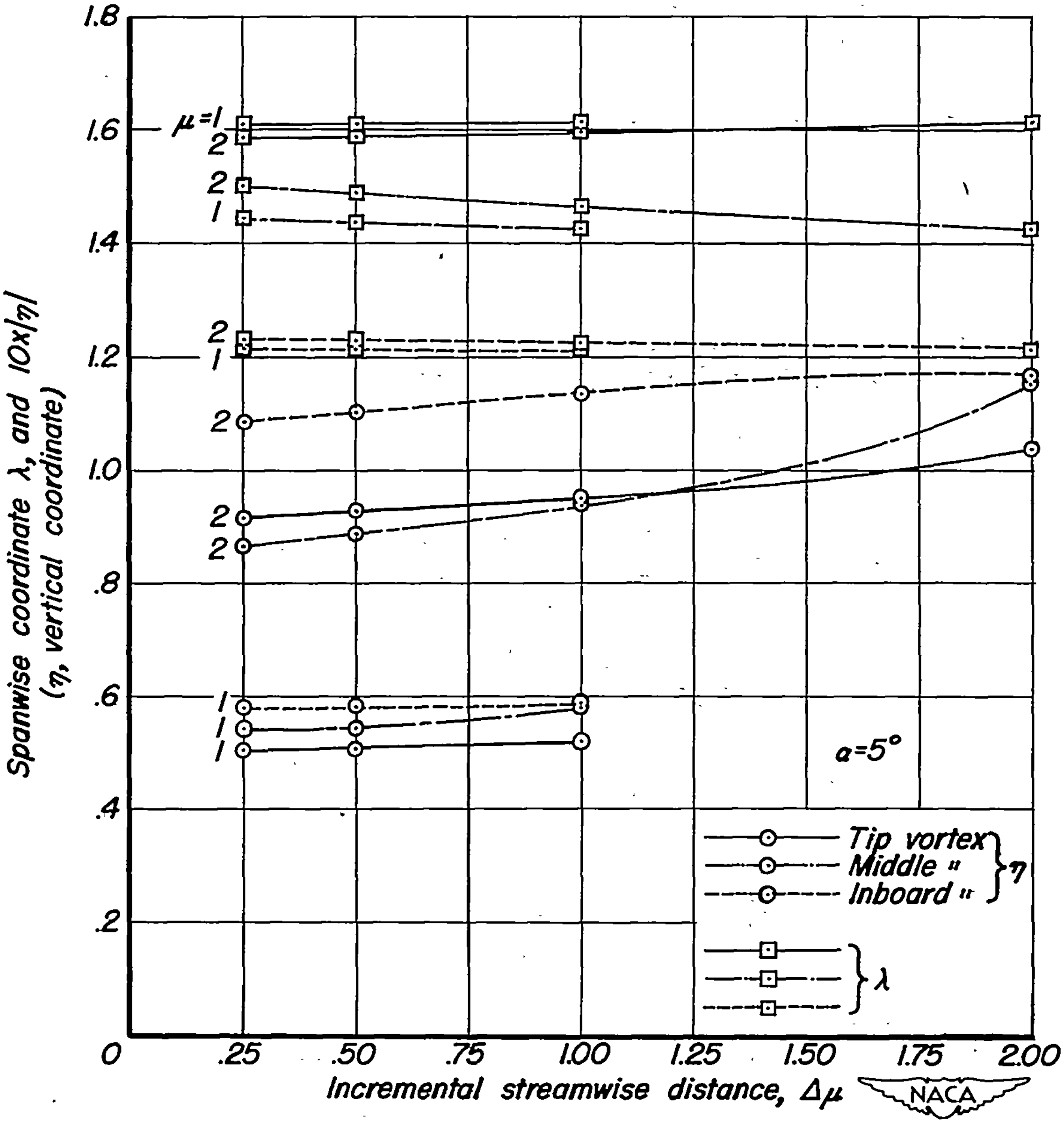

(a) Stations μ = 1 and 2.

Figure 22.- Vortex position error versus Δμ at stations μ = 1, 2, 3, and 4 for three wing vortex representations.

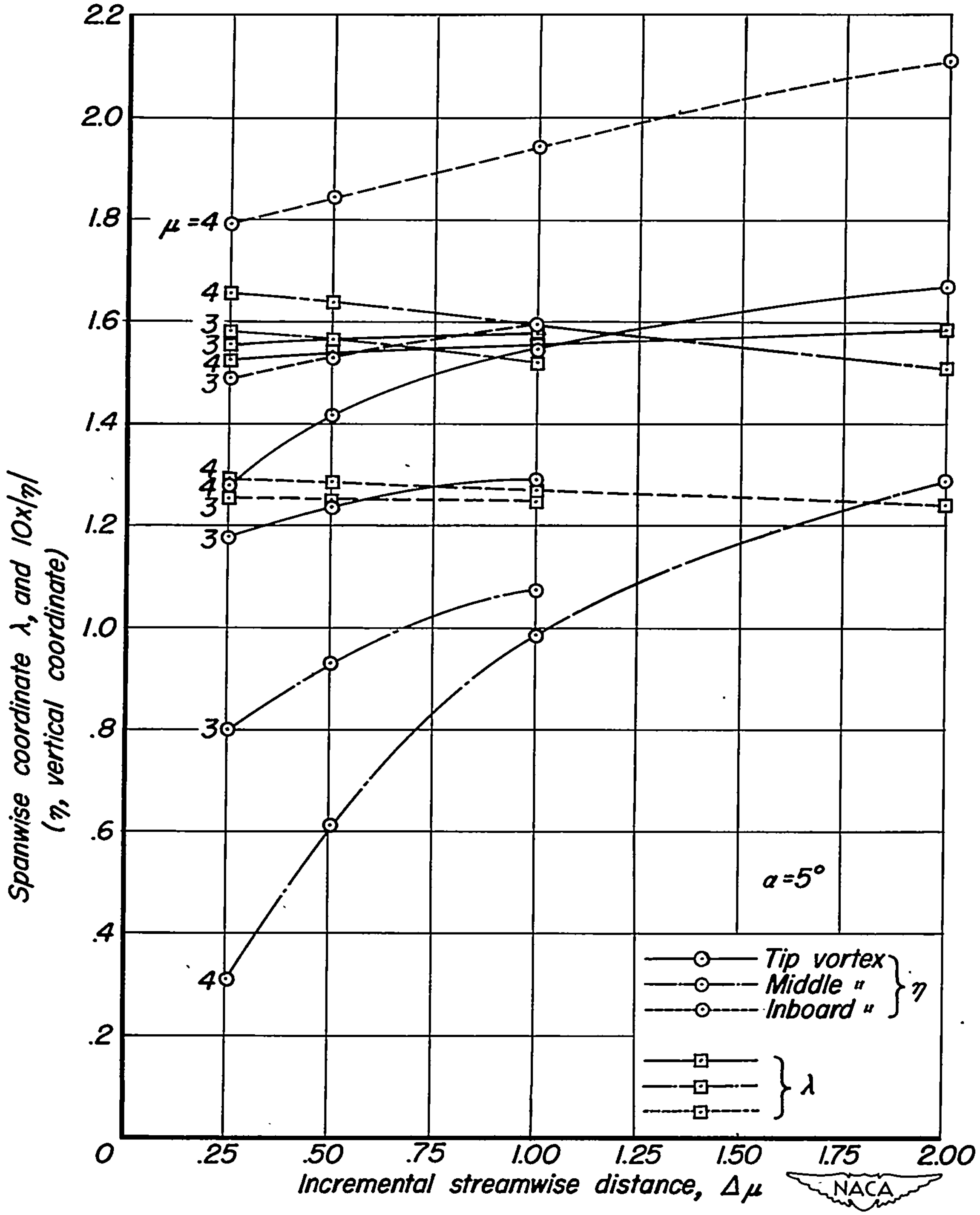

(b) Stations μ = 3 and 4.

Figure 22.- Continued.

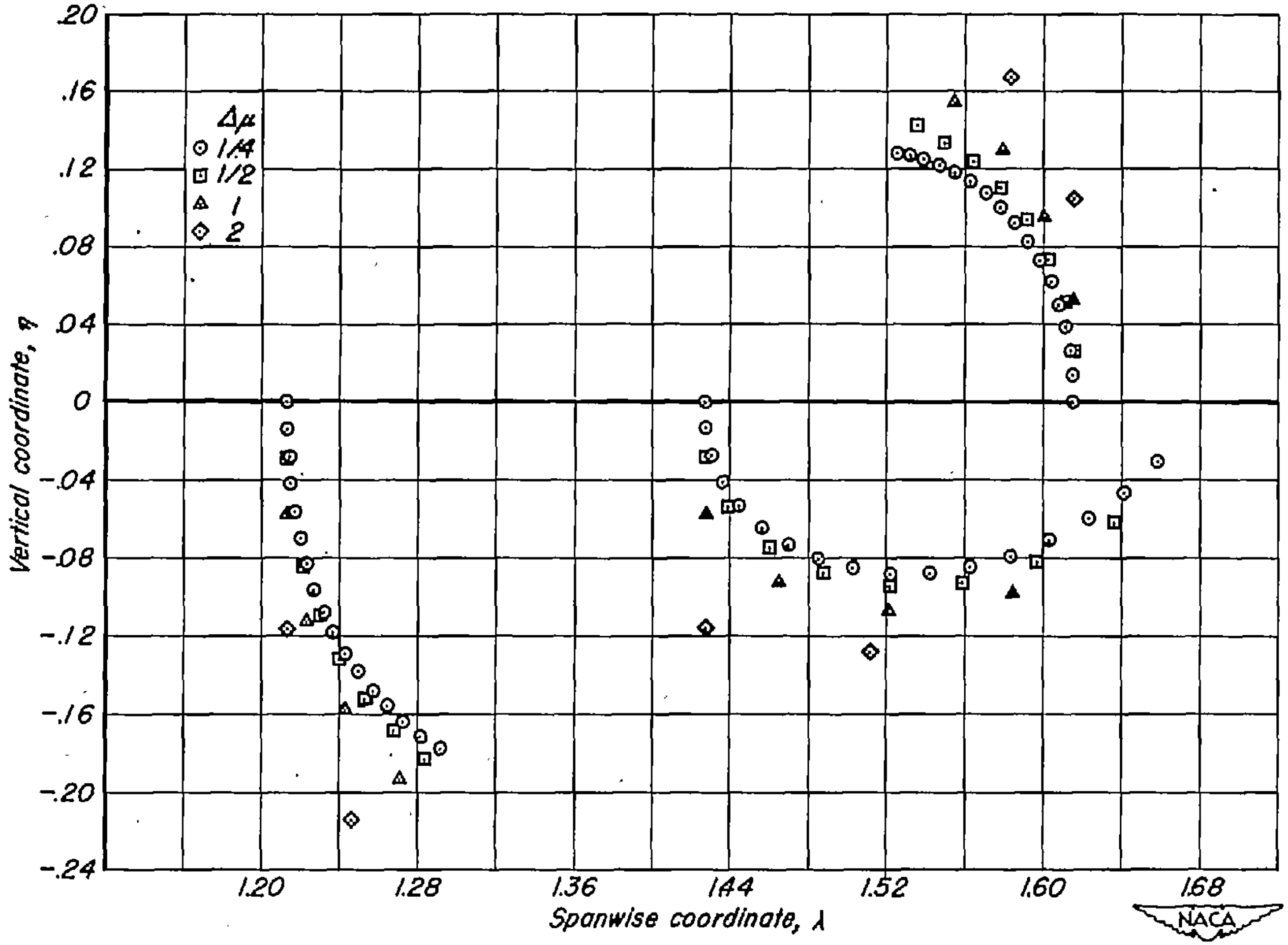

(c) Vortex paths from μ = 0 to μ = 4, with Δμ = 1/4, 1/2, 1, and 2, viewed in crossflow plane.

Figure 22.- Concluded.

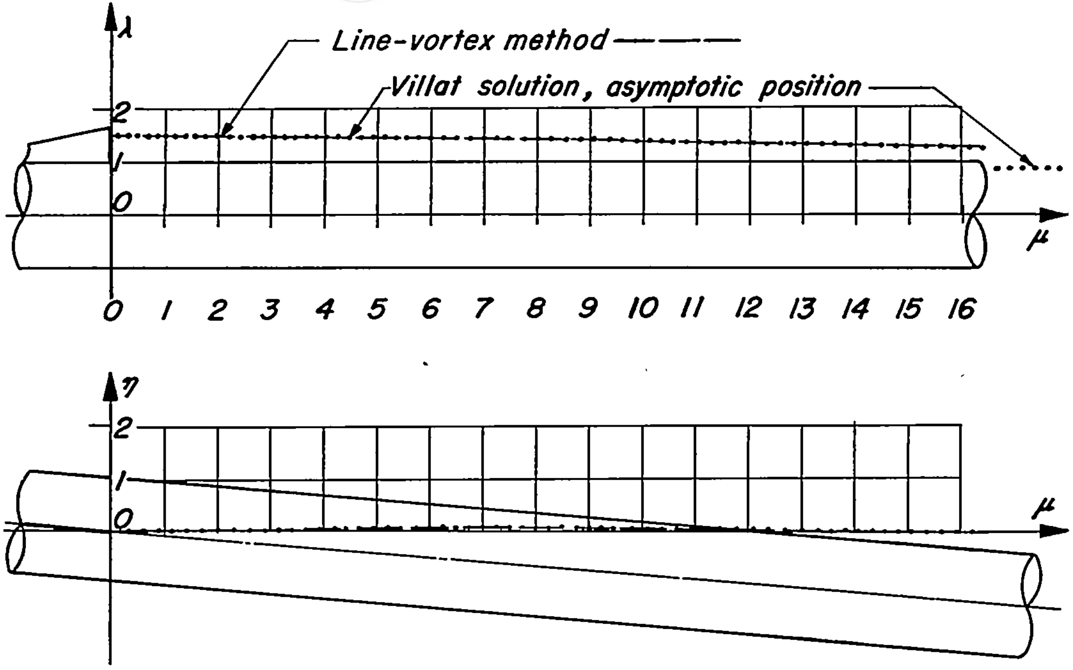

(a) Aspect ratio = 2/3, α = 5°, M = 2, r/s_m = 0.6

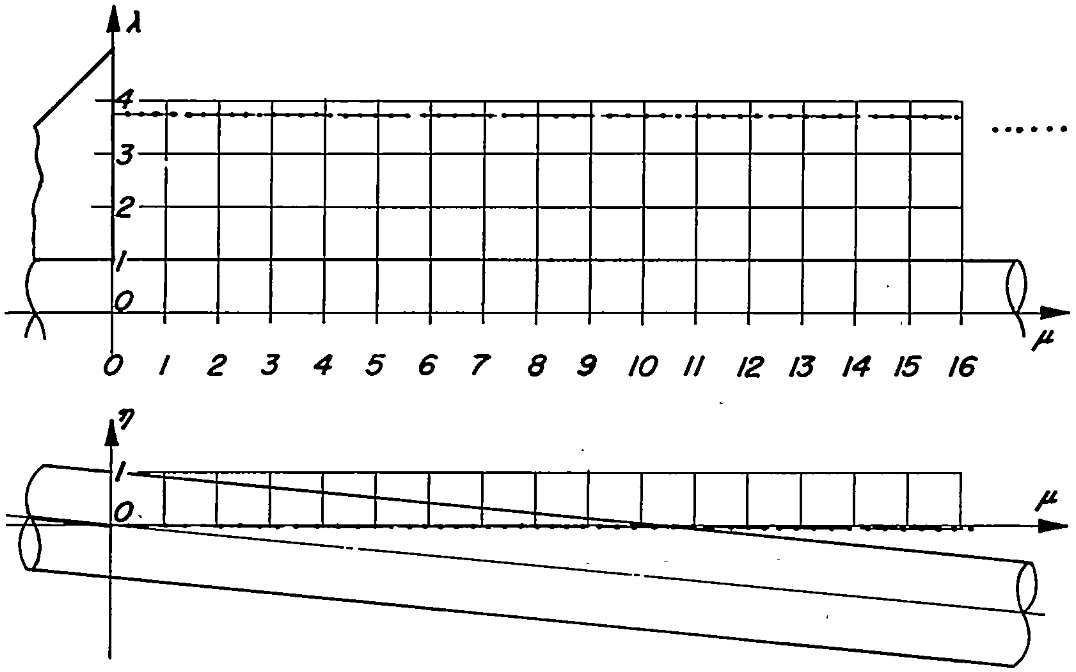

(b) Aspect ratio = 4, α = 5.5°, M = 2, r/s_m = 0.2

Figure 23.- Comparison of stepwise approximation with Villat (exact crossflow) solution for two wing-body combinations (ref. 18).

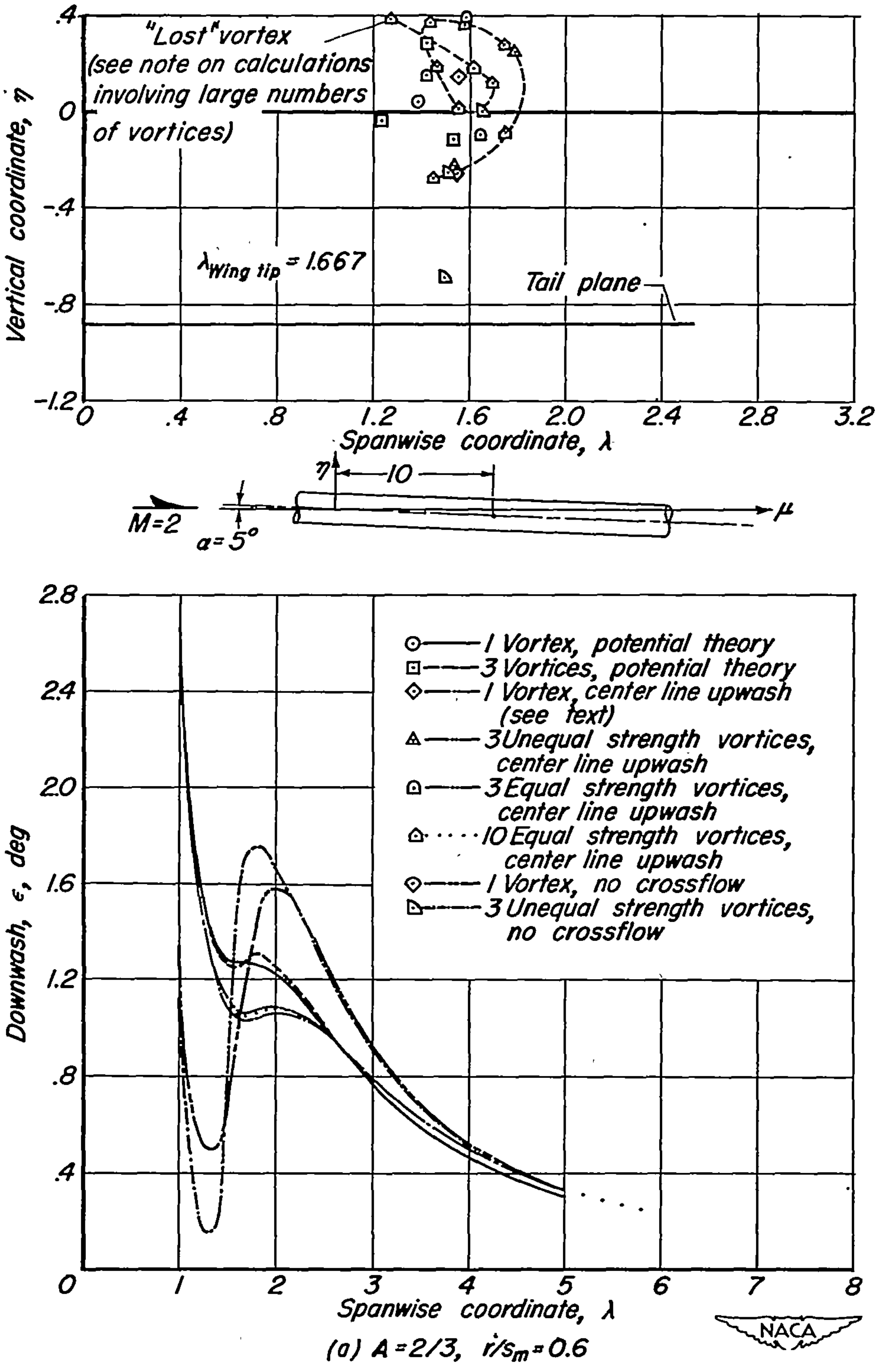

(a) Aspect ratio = 2/3, r/s_m = 0.6

Figure 24.- Effect of number of vortices on downwash at tail location for missile-type configuration.

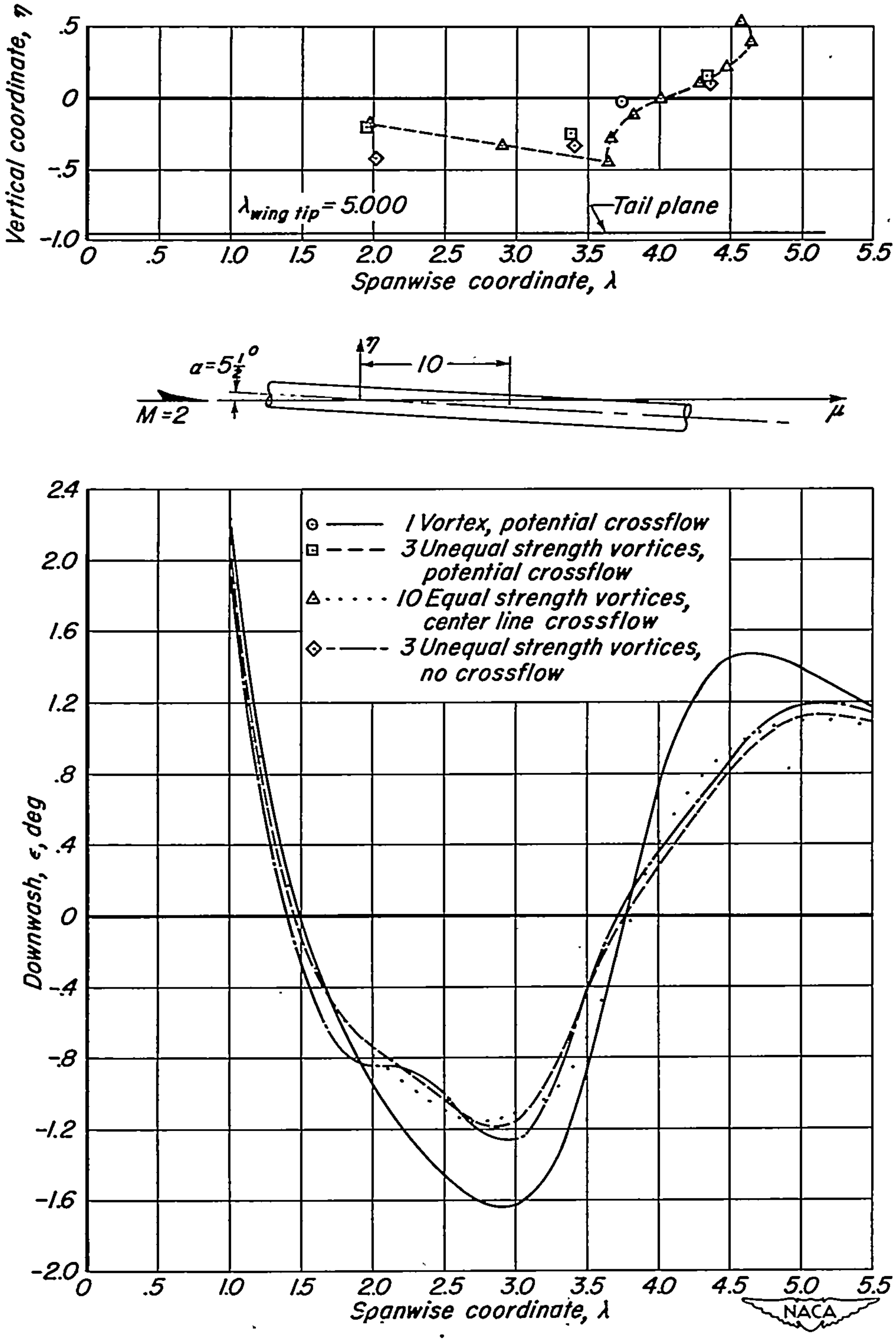

(b) Aspect ratio = 4, $r/s_m = 0.2$

Figure 24.- Concluded.

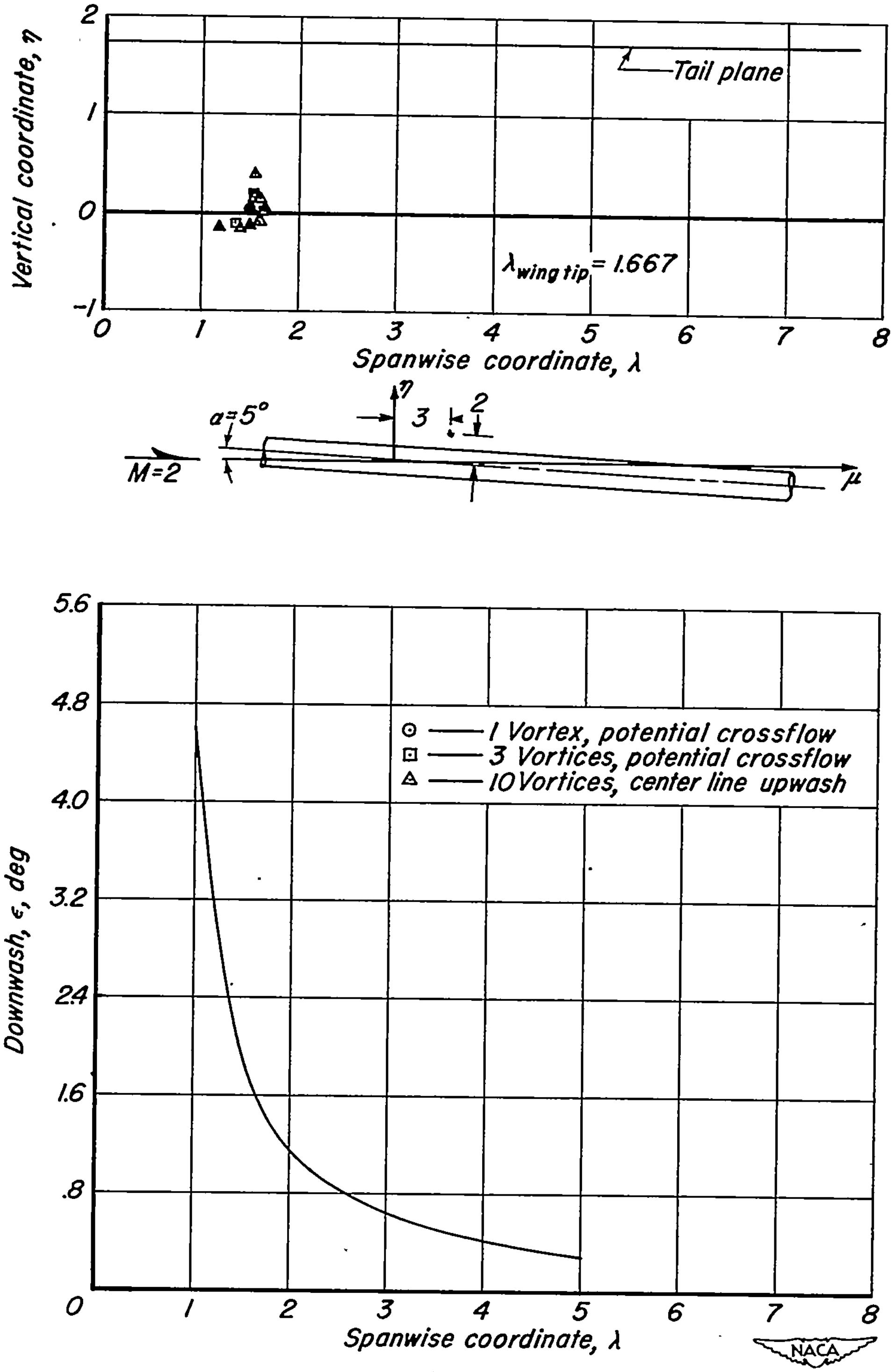

(a) Aspect ratio = 2/3, $r/s_m = 0.6$

Figure 25.- Effect of number of vortices on downwash at tail location for airplane-type configuration.

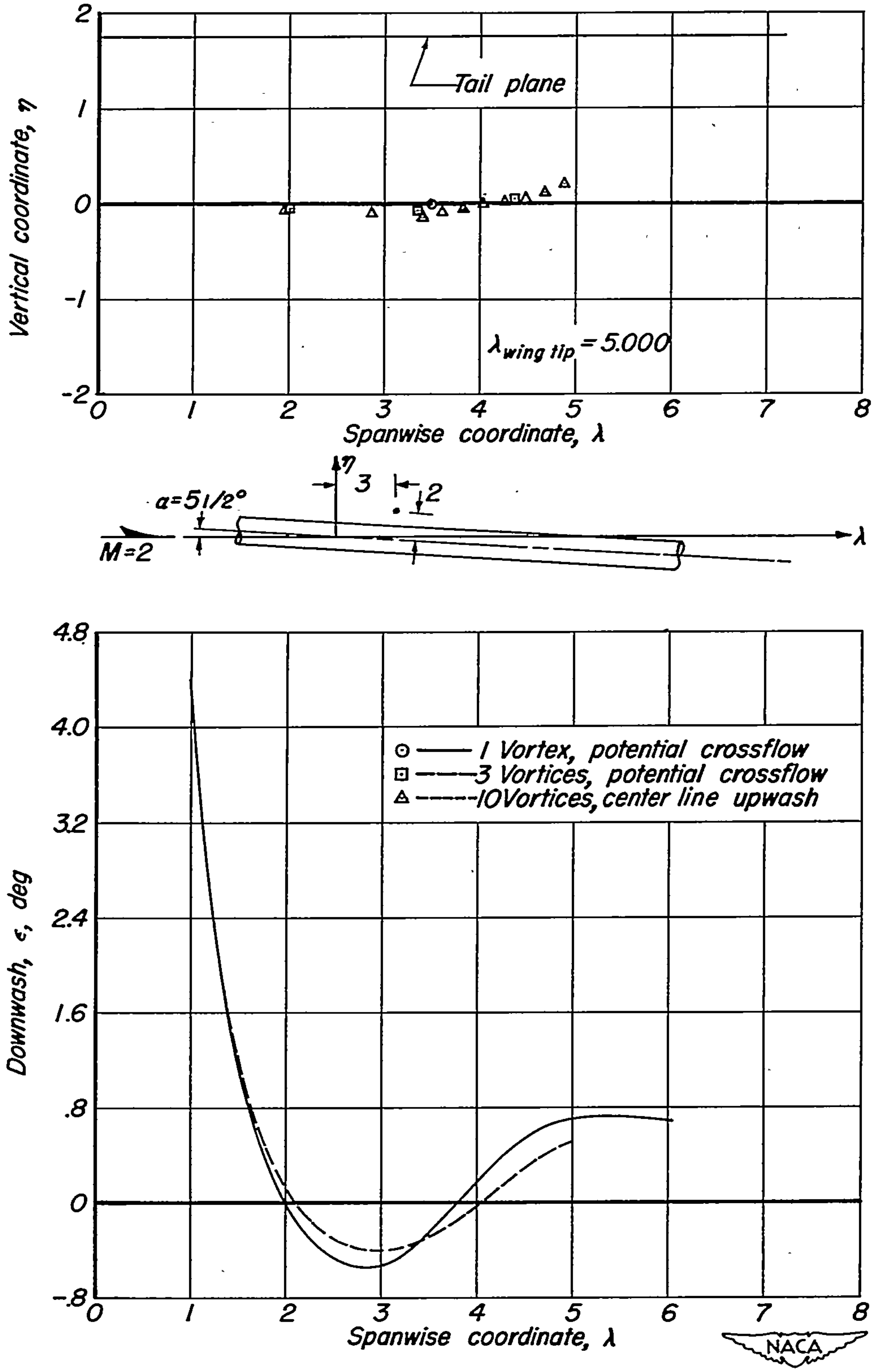

(b) Aspect ratio = 4, r/s_m = 0.2

Figure 25.- Concluded.

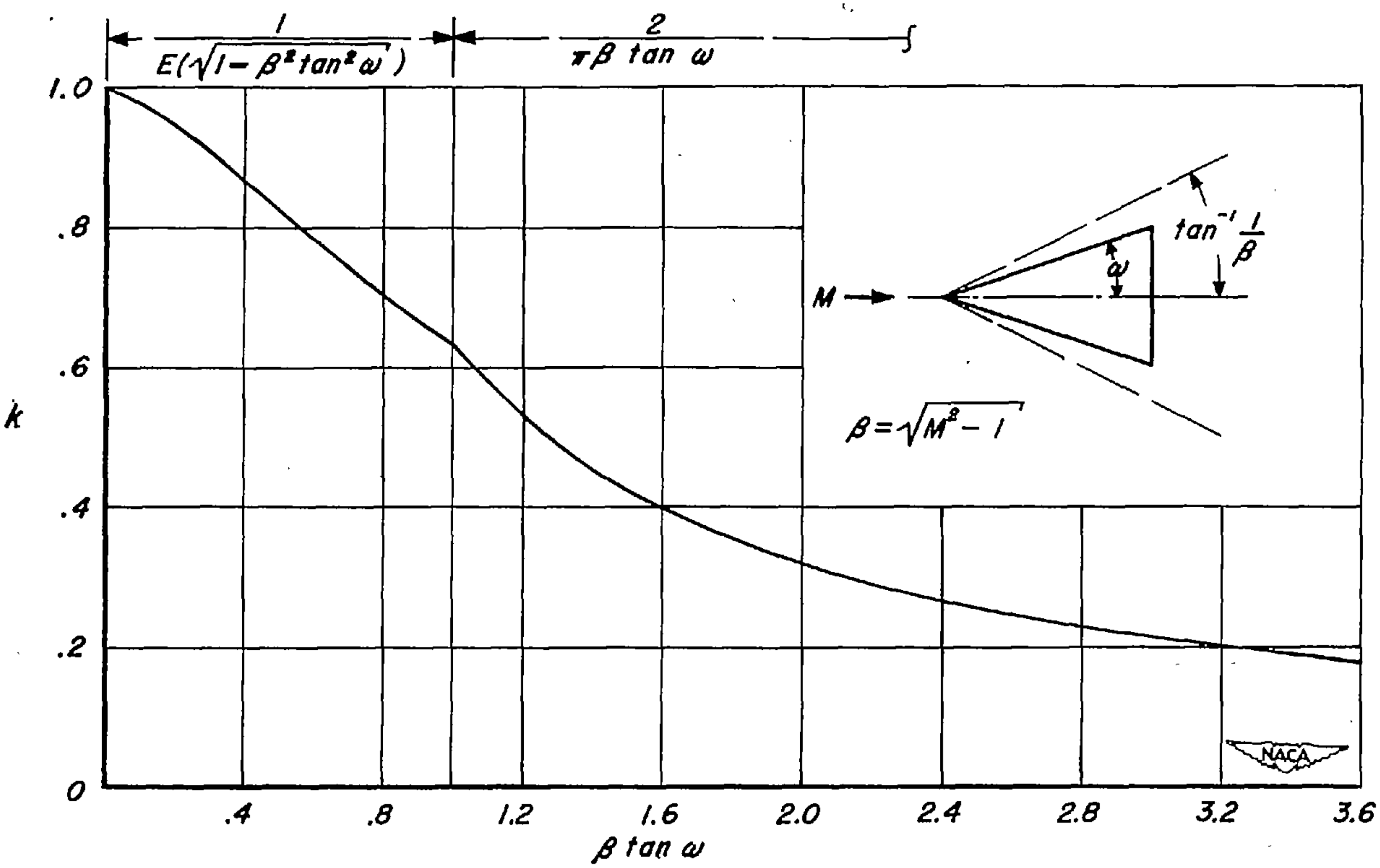

Figure 26.- Aspect-ratio correction factor k.

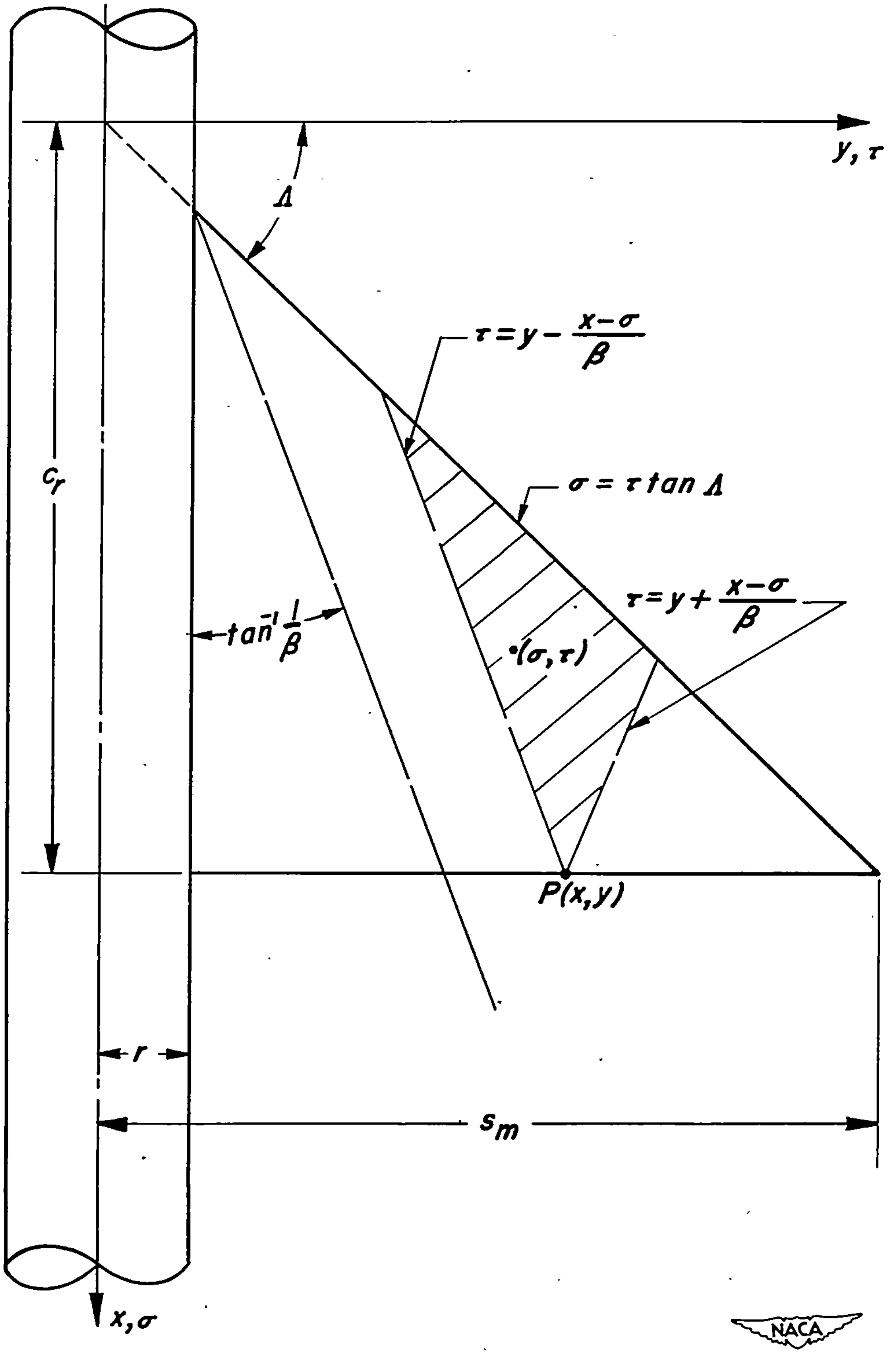

Figure 27.- Forecone of integration for equation (B8).

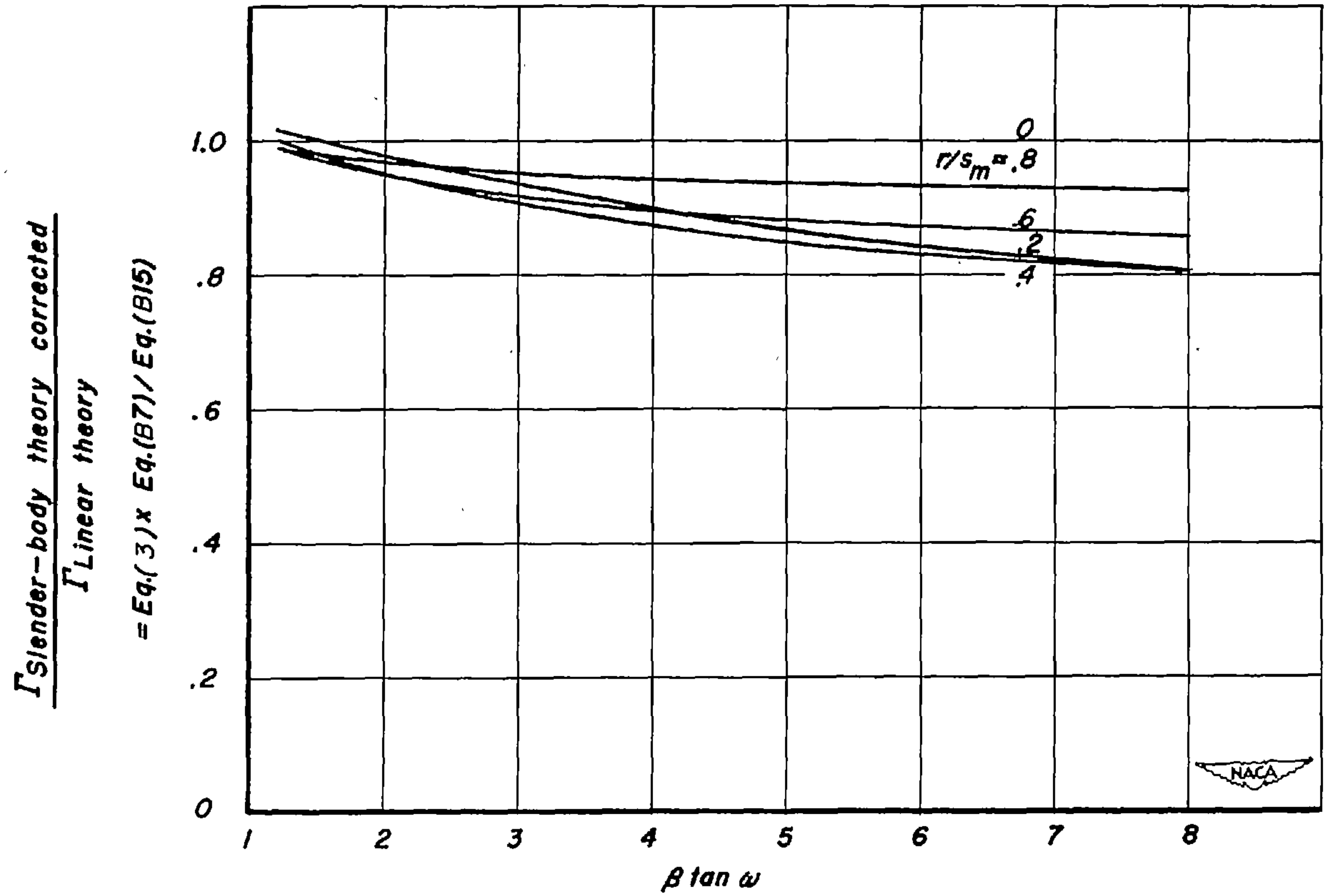

Figure 28.- Comparison of corrected slender-body and linear theories at Mach line on wing trailing edge.

NACA-Langley - 9-21-54 - 1000